



Jakob Kalt BSc.

Cu(I)- Oxide/Organic Semiconductor (PCBM) Heterojunction: Interface Engineering with Self-Assembled Monolayers

MASTERARBEIT

zur Erlangung des akademischen Grades

Diplom-Ingenieur

Masterstudium Advanced Materials Science

eingereicht an der

Technischen Universität Graz

Betreuer

Prof. Dr. Emil List-Kratochvil

Institut für Festkörperphysik

In Kooperation mit:



EIDESSTATTLICHE ERKLÄRUNG

Ich erkläre an Eides statt, dass ich die vorliegende Arbeit selbstständig verfasst, andere als die angegebenen Quellen/Hilfsmittel nicht benutzt, und die den benutzten Quellen wörtlich und inhaltlich entnommenen Stellen als solche kenntlich gemacht habe. Das in TUGRAZonline hochgeladene Textdokument ist mit der vorliegenden Masterarbeit identisch.

Graz, am

.....

(Unterschrift)

AFFIDAVIT

I declare that I have authored this thesis independently, that I have not used other than the declared sources/resources, and that I have explicitly indicated all material which has been quoted either literally or by content from the sources used. The text document uploaded to TUGRAZonline is identical to the present master's thesis.

.....

date

.....

(signature)

Kurzfassung

Ein Hauptziel des Forschungsbereiches der Photovoltaik ist es gleichermaßen die elektrischen Eigenschaften der Zelle zu optimieren als auch die Materialkosten zu minimieren. Kupferoxid ist dabei ein vielversprechender anorganischer Absorber. Das Material ist weltweit im Überfluss vorhanden und ermöglicht eine einfache großflächige Produktion, was sowohl den Anforderungen für Kosten per Watt als auch dem Materialnachschub genügt. Bis heute ist die größte Einschränkung dieses intrinsischen p-Typ Halbleiter die Identifizierung eines geeigneten n-Typ Halbleiters um eine Heterojunction Solarzelle herzustellen.

Der organische n-Typ Halbleiter PCBM wurde verwendet um die Heterojunction mit Kupferoxid herzustellen. Das Kupferoxid wurde elektrochemisch auf ein Au- bzw. ein ITO/Au/ITO- Substrat aufgetragen. Nach dem Spin-coating der organischen Schicht wurde abschließend eine transparente AZO-Top Elektrode mittels sputtering aufgetragen. Um die einzelnen Schichten zu studieren und zu charakterisieren wurden unterschiedliche Methoden verwendet, wie zum Beispiel SEM, AFM und IV-Messungen. Die Solarzellenstruktur Au/Cu₂O/PCBM/AZO-Struktur zeigte einen Short-Circuit Strom von $I_{sc} = -4,6 \frac{mA}{cm^2}$, eine Open-Circuit Spannung von $V_{oc} = 183 mV$, einen Füllfaktor von $FF = 27,3\%$ und eine Leistungsumwandlungseffizienz von $\eta = 0,229 \%$. Die raue Oberfläche des elektrochemisch aufgetragenen Kupferoxids und die inhomogene Auftragungstechnik des organischen Halbleiters hat einige leistungsbehindernde Effekte zufolge.

Im zweiten Teil dieser Arbeit wurde das Interface zwischen Cu₂O und PCBM mit Hilfe von selbstorganisierenden Monoschichten modifiziert. Diese SAMs sind in der Literatur weit verbreitet und eignen sich, um die Eigenschaften der Oberfläche zu modifizieren. Die für dieses Experiment ausgewählten Moleküle sind Benzoesäure-Derivate. Zuerst wurden der Einfluss der SAMs auf die Oberflächenenergie mittels dem KPFM nachgewiesen. Danach wurden die Eigenschaften in der IV-Messung bestimmt. In dieser Messung konnten keine leistungssteigernden Effekte nachgewiesen werden, aber eine partielle Kontrolle über die PV-Eigenschaften abhängig von der resultierenden Richtung der SAM-Dipolmomente konnte gemessen werden.

Abstract

A lot of research has been invested in the field of photovoltaics to optimize solar cell properties and minimize the production and material costs. Cuprous oxide has been attracted a lot of attention in recent studies as an inorganic absorber. This abundant material offers an affordable large scale production which accomplishes the requirement of cost-per-watt and material supply. The biggest limitation for this intrinsic p-doped material has been the identification of an appropriate n-doped semiconducting layer to form the heterojunction solar cell.

In this thesis, the organic n-type semiconductor PCBM has been used to build a heterojunction with cuprous oxide. The cuprous oxide has been electrochemically deposited on an Au- and an ITO/Au/ITO-substrate. After spin coating the PCBM a transparent AZO-top electrode has been sputtered. Each layer has been characterized using various techniques such as SEM, AFM and IV-measurements. The solar cell structure Au/Cu₂O/PCBM/AZO presented a short-circuit current of $I_{sc} = -4,6 \frac{mA}{cm^2}$, an open-circuit voltage $V_{oc} = 183 mV$, a fill-factor of $FF = 27,3\%$ and a power conversion efficiency of $\eta = 0,229\%$. The rough surface of the electrodeposited cuprous oxide and the inhomogeneous deposition technique of PCBM results in several performance hindering effects like a high shunt-resistance.

In the second part of this thesis the Cu₂O/PCBM interface has been modified with self-assembled monolayers. SAMs as a tool to influence the interfacial properties has been widely studied and reported. The molecules used in this thesis have been benzoic acid derivates. In a first approach the influence of the SAMs on the surface energy has been verified by using the KPFM. In the IV-measurement of the modified structure no performance enhancing effects could be seen but a partial control of the PV-properties depending on the resulting direction of the SAM-dipole moment could be studied.

Vorwort

Zuerst möchte ich mich bei meinem Professor Dr. Emil List-Kratochvil für die Unterstützung während meiner Zeit als Diplomand also auch für die Möglichkeit an diesem Projekt arbeiten zu können bedanken.

Weiteres möchte ich mich bei meinem Betreuer am Austrian Institute of Technology Dr. Theodoros Dimopoulos und dem ganzen Team für die tolle Zeit in Wien und die Unterstützung bei meiner Arbeit bedanken.

Auch bei Birgit Six und dem Team vom NTC möchte ich mich für die großartige Zusammenarbeit und Hilfestellung in Weiz bedanken.

Table of contents

1	Introduction.....	1
1.1	Targets.....	1
1.2	Tasks.....	2
2	Theoretical background	3
2.1	P-n junction ^{3,4}	3
2.2	Solar cells	5
2.2.1	Thin film solar cells.....	6
2.2.2	Light absorption ^{4,9}	7
2.2.3	IV-characteristic of the solar cell	8
2.3	Organic semiconductors	10
2.3.1	PCBM.....	12
2.4	Cu ₂ O absorber	13
2.5	SAM [Self Assembled Molecules].....	14
2.5.1	Electronic properties.....	14
2.5.2	Benzoic acid derivate	15
3	Characterization methods.....	17
3.1	AFM [Atomic Force Microscopy].....	17
3.2	KPFM [Kelvin Probe Force Microscopy]	17
3.2.1	Working principle ⁴⁵	17
3.3	Fourier transform infrared spectrometer (FTIR)	19
3.4	XRD	19
3.5	Electrical device characterization.....	19
3.6	SEM [Scanning Electron Microscopy].....	19
4	Solar cell fabrication procedure and design.....	20
4.1	Design of the heterojunction solar cell.....	20
4.2	Substrate preparation.....	21
4.3	Electrochemical deposition of cuprous oxide.....	22
4.3.1	Theoretical background of electrochemical deposition.....	22

4.3.2	Experimental influences of ECD of Cu ₂ O-absorber.....	23
4.3.3	Cu ₂ O structure on Au bottom electrode	25
4.3.4	Cu ₂ O structure on IMI bottom electrode	33
4.3.5	Summary of the Cu ₂ O structure on different bottom electrodes	36
4.4	Spin coating of organic layers	37
4.5	Sputtering of top-electrode	37
5	Inorganic-organic hybrid solar cell.....	38
5.1	Characterization of solar cell structure.....	38
5.1.1	Cu ₂ O/PCBM structural characterization	38
5.2	IV-measurement to characterize the photovoltaic properties of the hybrid solar cell	41
5.3	Conclusion of Cu ₂ O/PCBM heterojunction	52
6	Interface modification using SAMs.....	53
6.1	Interfacial structure.....	53
6.1.1	Interfacial modification using SAMs	55
6.2	SAMs characterization	56
6.2.1	Contact angle measurement.....	56
6.2.2	AFM and KPFM measurements	57
6.3	Cu ₂ O/PCBM interface characterization with the KPFM.....	66
6.4	Modification of Cu ₂ O/PCBM interface with selected SAMs.....	69
7	Conclusion	76
	Bibliography	78
	List of Figures	85
	List of tables	88

1 Introduction

Since the discovery of the photoelectric effect and the development of the solar cell people could produce energy directly from solar energy. Solar energy is sustainable and will play a crucial role in the future energy supply.¹ In the last few centuries the efficiency and power conversion of solar cells increased drastically which can be seen in the following graph from the NREL.

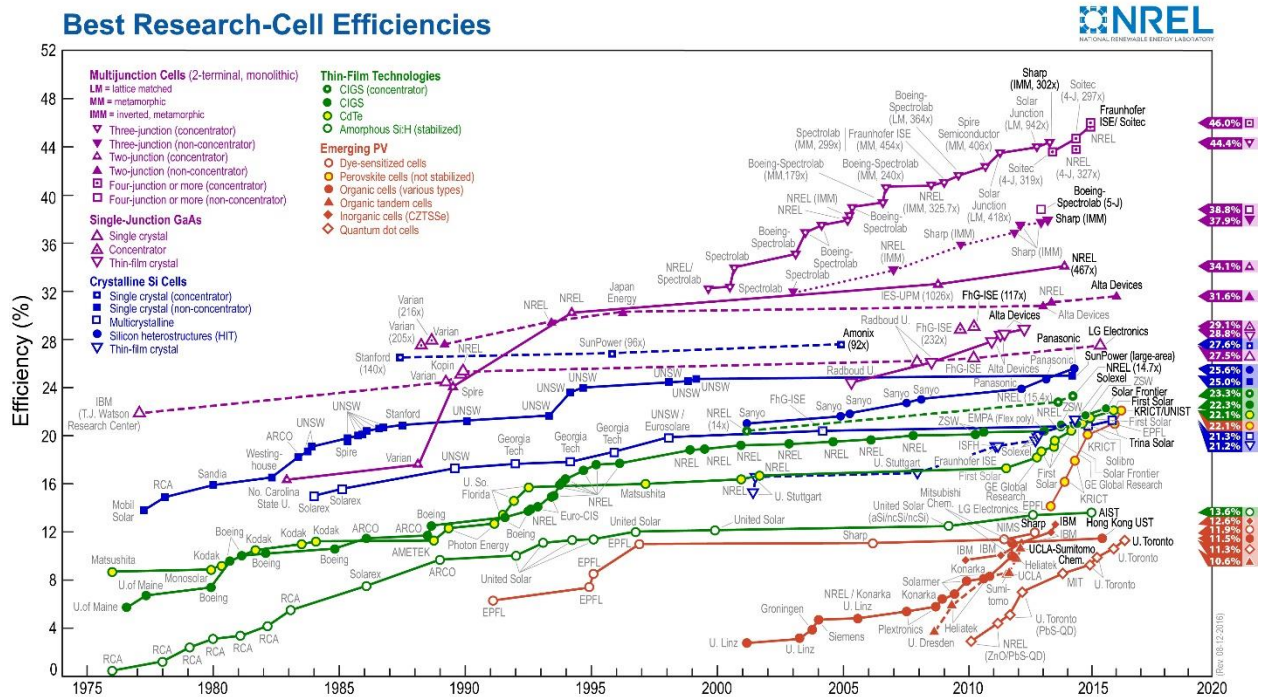


Figure 1 Overview of the highest confirmed conversion efficiencies for research solar cells by the National Renewable Energy Laboratory (NREL)²

1.1 Targets

The target of this work is to manufacture and investigate a new hybrid inorganic-organic thin-film solar cell based on the Cu_2O (absorber)/PCBM heterojunction.

The work will be divided in two parts. The main focus of the first part will be the investigation of the interface of the pn-junction formed by the inorganic p-type semiconductor Cu_2O and the organic semiconductor PCBM. Since this structure has never been reviewed before a detailed optimization and characterization of the individual layers must be performed.

The focus of the second part will be on the interface engineering of these two materials. The interface will be modified additional Self Assembled Monolayers (SAM) in an attempt to tune the energy band alignment of the heterojunction.

1.2 Tasks

The first task will be the preparation and manufacturing of the solar cell. Each layer and the preparation will be described in the following chapters of this thesis.

The bottom electrode will be sputtered on a glass substrate. The inorganic absorber will be manufactured by electrochemical deposition. The organic n-type semiconductor will be deposited by spin coating. As a top electrode, a transparent conductive oxide will be sputtered on top of the structure.

To determine the various properties of the semiconductors, the interface and the working solar cell appropriate instruments will be used.

The surface of the individual layer will be characterized by the SEM, AFM and XRD. The resulting solar cell will be tested by analysing the IV-characteristics with and without illumination.

The interface engineering will be studied in detail with the KPFM which gives a direct insight to the change in the surface energy.

2 Theoretical background

2.1 P-n junction^{3,4}

To understand the background physics behind solar cells it is essential to review the p-n junction.

The p-n junction is formed by aligning two semiconductors together, one p-type and one n-type semiconductor. The majority carriers in the n-type semiconductor are electrons with electron density N_D . The additional donor states shift the fermi level from the intrinsic position $E_{F,i}$ up to a position near to the conduction band E_C which can be seen in Figure 2 (b). Respectively for the p-type semiconductor seen in Figure 2 (a), the majority carriers are holes with a hole density of N_A . Holes correspond with a missing electron in the valence band. These additional hole-states shift the intrinsic fermi energy $E_{F,i}$ down to a position near to the valance band E_v .

When the two semiconductors are brought in contact a diffusion current starts flowing, due to the exchange of excess majority carriers (holes and electrons for p-type and n-type respectively). The leftover ion cores create an electric field and due to this a drift current opposes the diffusion current. A depletion region forms depleted of free charge carriers as seen in Figure 2 (d). With no external bias applied a thermal equilibrium forms. This implies that the fermi-level E_F is constant throughout the whole junction which causes the bands to bend. The magnitude of the bending is defined by the build-in voltage V_{bi} (c). It equals the potential difference between the two fermi levels of the p-type semiconductor $E_{F,p}$ and the n-type semiconductor $E_{F,n}$.

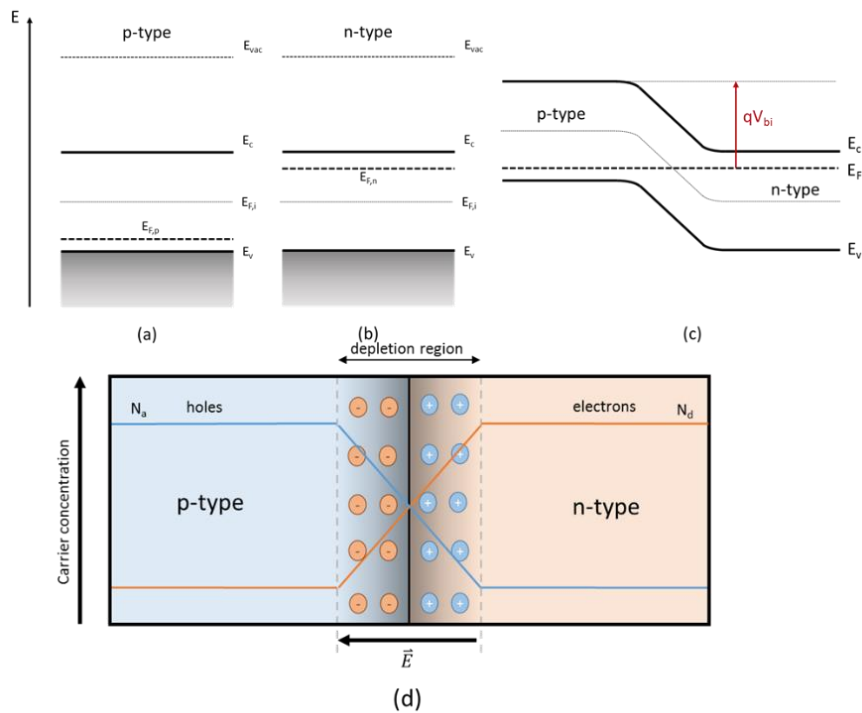


Figure 2 Schematic diagrams of a p-n junction: (a) p-type (b) n-type (c) junction in contact and equilibrium (d) carrier concentration diagram

The behavior of a p-n diode in an electric circuit can be studied by applying an external bias voltage V_a . A forward bias corresponds to a positive voltage applied at the p-side and a negative voltage at the n-side. Due to this electrons and holes are driven towards the junction and the depletion region becomes narrower. As a result, minority carriers are injected on each side respectively and a current start flowing. In the reverse bias case, the applied voltage is interchanged and the holes as well as the electrons are driven away from the junction. This results in an increasing electric field which sweeps away the minority electrons from the p-side and the minority holes from the n-side. The depletion region in this case becomes wider and no current can flow.

Both cases are shown in the band diagrams of Figure 3. It is important to note that as a consequence of the external bias the bands are not in thermal equilibrium any more. A positive voltage decreases the built-in potential (a) and a negative voltage increases it (b).

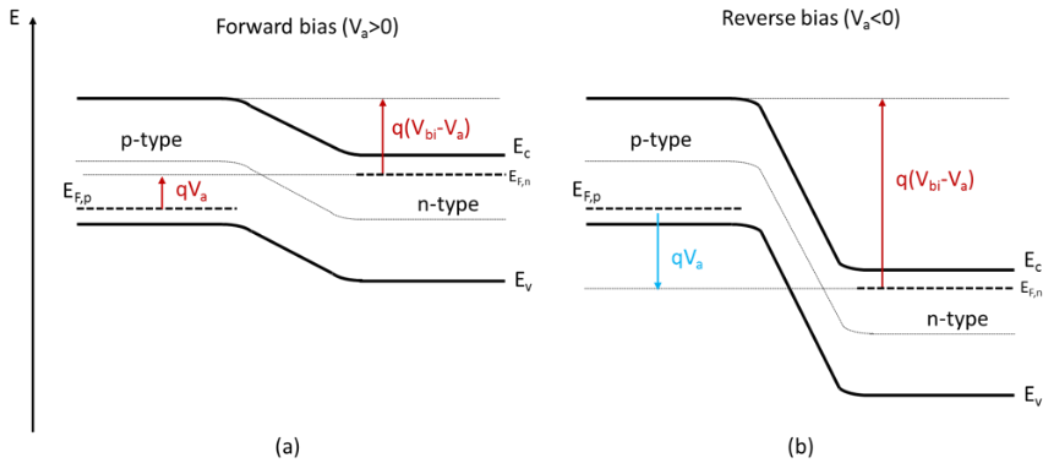


Figure 3 Energy band diagram of a p-n junction with external applied bias: (a) forward bias (b) reverse bias

Derived from the Shockley equation⁵ one can write down the ideal diode equation:

$$I = I_0 \left[\exp\left(\frac{qV}{nk_b T}\right) - 1 \right] \quad \text{eq. 1}$$

with I_0 the dark saturation current, V the applied voltage, q the charge, n the ideality factor, k_b the Boltzmann constant and T the temperature.

2.2 Solar cells

A solar cell is an electronic device which is used to directly generate electrons from incoming light with a high conversion efficiency. In a simple approximation, it can be seen as a diode illuminated with light and operated in forward bias.

Normally solar cells are illuminated by sunlight with the intention to convert solar energy to electrical energy. Therefore, one has to keep the radiation spectrum of the sun in mind. For laboratory purpose the most important standard is nowadays the AM 1.5 with a power density of 1000 W/m². An up to date version of this standard has been plotted in Figure 4. All used data and information are from the “Solar spectral” website.⁶

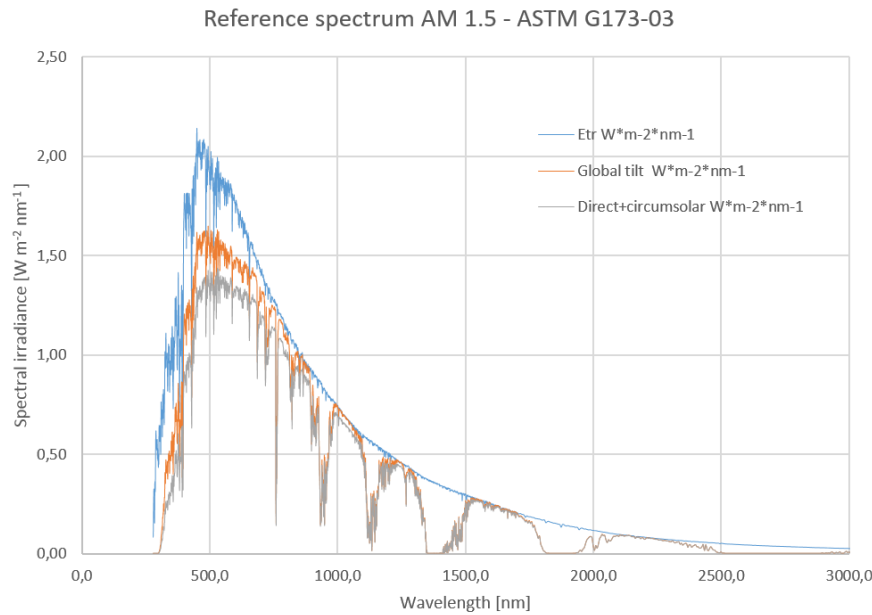


Figure 4 reference sun solar spectrum

2.2.1 Thin film solar cells

As mentioned in the introduction, solar cells are the most promising emerging technology in the renewable energy sector. Up until today the cost of large scale photovoltaic modules hinders its further rise. That is why researchers try to decrease the production cost and increase the power conversion efficiency. The manufacturing of thin film cells can be seen as a good trade-off since the cells are thinner and save a lot of raw material.⁷

To optimize the thickness, the absorption of the incident light becomes even more important. A highly absorbing material is to be used with a band gap in the region 1-1,5 eV for an optimal absorption of the incident solar light. This energy is an equivalent to a wavelength region of 350 – 1000nm. Compared with Figure 4 it is easy to identify this region as a maximum in the solar spectrum.

The word thin film is yet to be defined exactly but thin film solar cells are in a range of approximately 100 nanometres to several micrometres.⁸

Nowadays the best working thin film solar cells with reasonable trade-off between cost and efficiency are copper indium gallium selenide (CIGS), cadmium telluride (CdTe) as well as tandem-solar cells using polycrystalline silicon. From Figure 1 one can identify the maximum efficiencies for CdTe and CIGS both over 20%. Another upcoming technology has been the development of perovskite solar cells which have increased their device efficiencies in the last 10 years from under 10 % to 22,1% in 2016.

2.2.2 Light absorption ^{4,9}

A key factor in solar cells is the interaction of the semiconductor and the incoming light. This process involves a number of interacting particles in the electrons, holes, phonons and photons which are required to conserve the momentum and energy. A photon necessary to excite an electron from the valence band to the conduction band requires an energy higher than the band gap energy E_g . The absorption depends on the band structure of the semiconductor where in general two types of bandgaps are distinguished: the direct bandgap and the indirect bandgap semiconductor.

In a direct bandgap semiconductor, the minimum of the conduction band emerges at a position near to the maximum-position of the valence band. Therefore, they share the same wavevector k and thus a similar momentum and an electron-hole pair can be produced without additional momentum.

In the indirect bandgap semiconductor, the minimum of the conduction band has a different wavevector than the maximum of the valence band. Therefore, the momentum conservation is not fulfilled and the electron must change its momentum significantly to produce an electron-hole pair. Since the momentum of photons is very small, the involvement of an additional particle, the phonon (lattice vibration), is required to equal the difference in momentum. The additional energy required and the involvement of the phonon in the transition makes the indirect bandgap semiconductor less efficient and slower.

Therefore, most of the time direct bandgap semiconductors are used in thin film photovoltaics where high absorption is necessary.

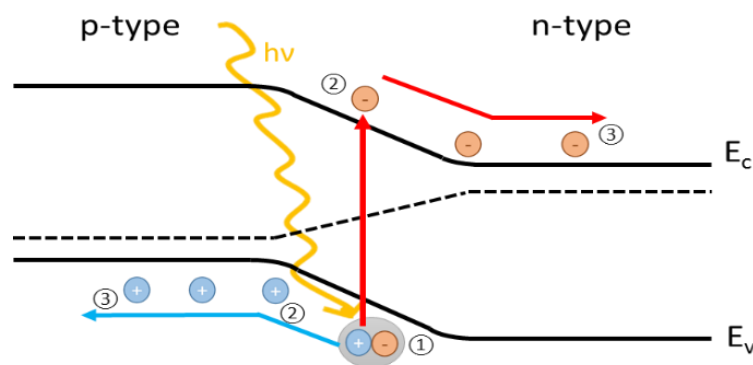


Figure 5 light absorption scheme

Once absorbed, a photon with a sufficient energy (larger than the band gap energy) can generate an electron – hole pair (inner photoelectric effect, Figure 5 (1)). In the depletion region of the p-n junction the strong electric field separates the charges and hence prevents recombination as seen in (2) of Figure 5.

These minority carriers (holes in n-type and electrons in p-type) are collected by the electric field and accelerated towards the opposite direction (holes towards the p-type and electrons towards the n-type).

When crossing the depletion region these minority carriers become majority carriers (holes in p-type and electrons in n-type, see Figure 5 (3)). The resulting photocurrent I_{ph} from these photo generated carriers adds to the diode current without illumination (eq. 1)

$$I = I_0 \left[\exp\left(\frac{qV}{nk_bT}\right) - 1 \right] - I_{ph} \quad \text{eq. 2}$$

2.2.3 IV-characteristic of the solar cell

Important device and characterization parameters can be found when measuring the I-V curve with and without illumination. For a better illustration a schematic I-V curve is plotted in Figure 6.

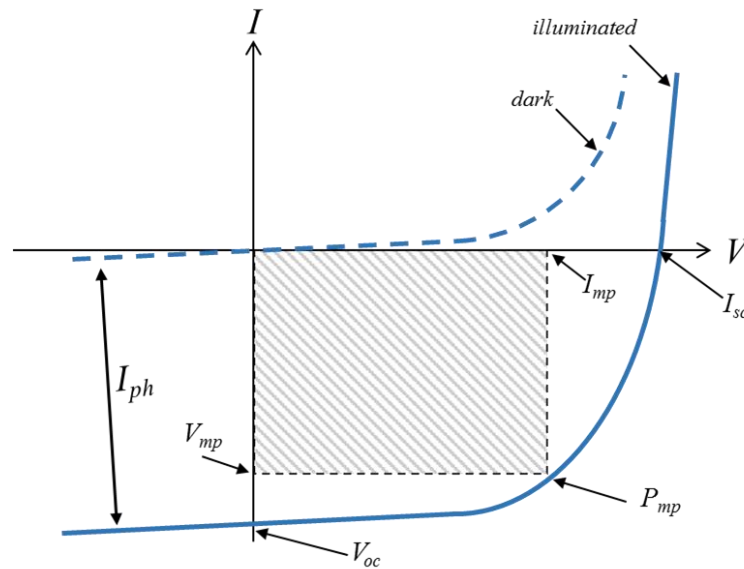


Figure 6 I-V curve of solar cell

The IV-curve is used to characterize the solar cell output parameters.

The open-circuit voltage V_{oc} is the voltage across the illuminated cell at zero current. The short-circuit current I_{sc} is the current through the cell at zero voltage. The power equals the product of current times the voltage and reaches a maximum at the maximum power point P_{mp} .

From these parameters the third important parameter can be calculated, the Fill Factor. The Fill-Factor (FF) of the solar cell is defined as the ratio of the maximum power to the product of the open-circuit voltage and the short-circuit current.

$$FF = \frac{P_{mp}}{I_{sc} V_{oc}} = \frac{I_{mp} V_{mp}}{I_{sc} V_{oc}} \quad \text{eq. 3}$$

From these characteristics the energy-conversion efficiency η can be calculated:

$$\eta = \frac{FF V_{oc} J_{sc}}{P_{ill}} \quad \text{eq. 4}$$

With P_{ill} representing the total input power by the incident light illuminating the cell.

The above presented characteristics describe an ideal solar cell. When considering a real solar cell, it is important to describe deviations from the ideal case. From eq. 4 it is possible to see that only the products in the numerator can be influenced from losses since the incident light illumination is constant.

The influencing losses can be summarized as parasitic effects with the shunt resistance and the series resistance of the solar cell as the most important. Therefore, an equivalent circuit model for the solar cell indicating these effect has been drawn in Figure 7.

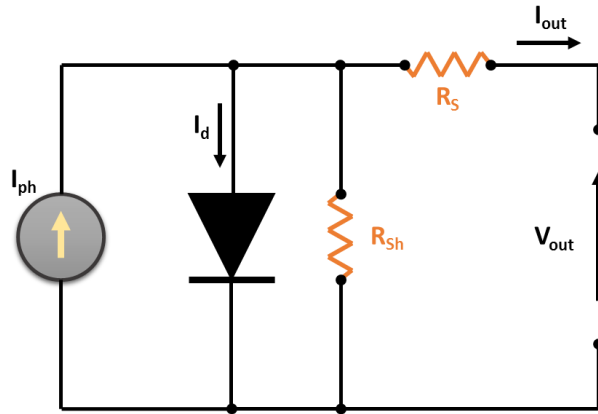


Figure 7 equivalent circuit of solar cell

Most of the time these two resistances are influencing the Fill-Factor of the solar cell. The resistance is area dependent, which is why usually the area normalized resistance $R_n = \frac{V_{oc}}{J_{sc}}$ in Ωcm^2 is used. Typically, the characteristic resistance R_{ch} of the solar cell is the output resistance at the maximum power point. It can be calculated by the inverse slope at the maximum power point, which is $\frac{V_{mp}}{I_{mp}}$.

The shunt resistance R_{sh} is normally caused by manufacturing defects such as the thickness and chemical composition inhomogeneity's. Shunts can be seen as alternative current path for the light generated carriers which is why R_{sh} is in parallel to the diode resistance. From simple electronics two assumptions can be derived. The first is since R_{sh} is in parallel a very high shunt resistance is desired, (ideally $R_{sh} = \infty$) where the diode resistance is yet too high to flow on the alterative path. Secondly,

the parallel resistance has a larger impact in low voltage regions, which is why an estimate value for R_{sh} can be derived by fitting a slope near the short circuit current.

The series resistance R_s is caused by contact resistance between the semiconductor and the metallic contacts as well as current resistance and charge collection of the electrodes. It is desired to be as low as possible. The series resistance can be determined by a slope in the nearby area of the open circuit voltage. At open-circuit voltage the overall current flows through the solar cell. At this point the resulting series resistance should be very low, in an ideal case it should be zero ($R_s = 0$).

The main impact of both resistances is influencing the Fill-Factor but at a high value R_s and a low value of R_{sh} it can also lead to a reduction of the V_{oc} and the I_{sc} respectively.^{9,10}

2.3 Organic semiconductors

Organic semiconductors in general are carbon-based materials, which combine the chemical and mechanical properties of organic compounds with the electric properties of semiconductors.

Basis of organic semiconductor are a conjugated π electron system. Conjugation are alternating single and double-bonds in the molecules leading to a delocalisation of the charge carriers. The interaction of these π -orbitals over the distance of several repeating units results in an energy-band-like structure.

The formation of double-bonds in carbon molecules plays a crucial role in this process and can be explained by sp^2 -hybridization of ethene (Figure 8). The molecular structure of ethene is C_2H_4 . From each C-atom the 2s orbital mixes with two 2p-orbitals to reach a favourable energetic state. These three hybridized sp^2 -orbitals arrange in a 120° bond angle to form a plane. One sp^2 -orbital of both C-atoms overlaps and they form a sigma-bond (σ). The leftover un-hybridized $2p_z$ -orbital arranges perpendicular to the plane formed by the sp^2 -orbitals. The electrons in these $2p_z$ -orbitals form the additional π -bonds. (Figure 8 (a))

When combining the two C-atoms the hybridized atomic sp^2 -orbitals will split into a binding (σ) and anti-binding (σ^*) orbital. Also the $2p_z$ -orbitals will form a binding (π) and anti-binding (π^*) orbital. Since the interaction of the $2p_z$ -orbitals is further away from the nucleus the splitting will be weaker for the π -case and is displayed in Figure 8 (b). The highest occupied molecular orbital (HOMO) is represented by the π -orbital and the lowest unoccupied molecular orbital (LUMO) by the π^* -orbital. The energy difference between these is the band gap and leads to the semiconductor properties.¹¹

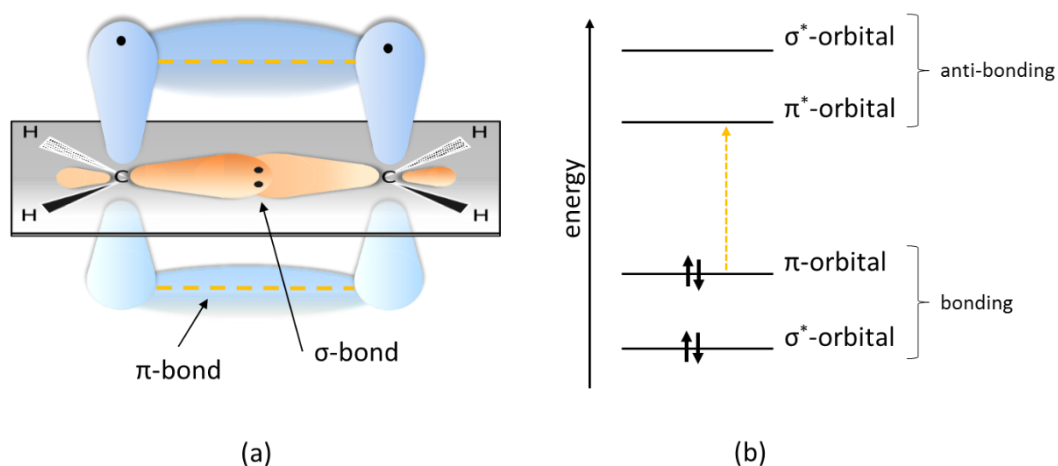


Figure 8 hybridization of ethene (a) orbital scheme (b) energy level diagram

When the conjugated structure is continued over a longer chain, the electronic charge becomes delocalized and forms a band-like structure. Therefore, the LUMO can be seen as an equivalent to the conduction band and the HOMO as an equivalent to the valence band.

To classify conductive organic materials, the conductivity σ represents an important parameter. It is defined as the product of the charge density n , the elemental charge e and the mobility of the charge carriers μ . (eq. 5)

$$\sigma = ne\mu \quad \text{eq. 5}$$

To increase the conductivity, it is possible to increase the amount of charge carriers and their mobility. But when doping organic material to increase its charge carriers it automatically decreases the mobility due to scattering on defects.

The low mobility μ of charge carriers is generally a problem in organic semiconductors. The dominating transport mechanism is called phonon-assisted hopping. Due to the disorder and defects of polymer structure the charge carriers are localized which in turn has a large effect on the mobility. [12, Figure 9] Typical mobility values for organic single crystals are in the range of $\mu = 1 \text{ cm}^2/\text{Vs}$ ¹³ and $\mu = 10^{-7} - 10^{-3} \text{ cm}^2/\text{Vs}$ for polymer organic semiconductors at room temperature¹².

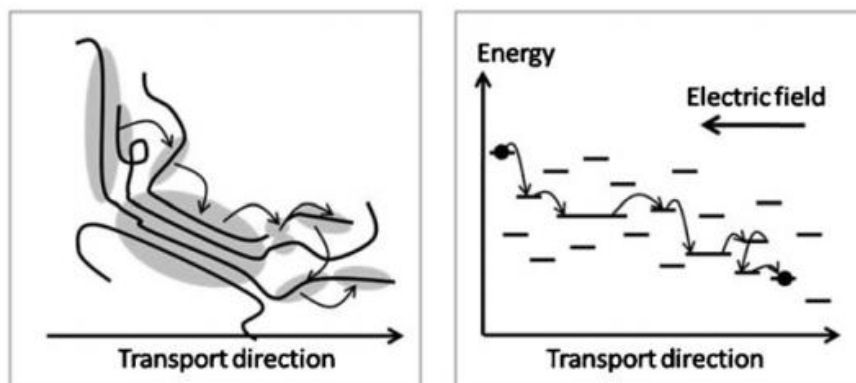


Figure 9 hopping mechanism (left) spatial and (right) energy landscape of hopping transport under influence of an external electric field [figure taken from¹²]

2.3.1 PCBM

The full name of PCBM is [6,6]-Phenyl C₇₁ butyric acid methyl ester. It is a fullerene derivate which has been used very often in bulk heterojunction organic solar cells because of its high hole mobility. It is a n-type semiconductor with an approximate mobility of $0,1 \text{ cm}^2/\text{Vs}$.¹⁴

The key element of its electronic properties is the so called “Buckyball”, a Buckminsterfullerene. The one used in this work has been a C₇₀-fullerene consisting of 70 carbon atoms. Because of this, PCBM is also notated in the thesis as either [70]PCBM or PC₇₁BM. A schematic picture taken has been added in Figure 10 to illustrate the conjugated structure of the organic semiconductor.

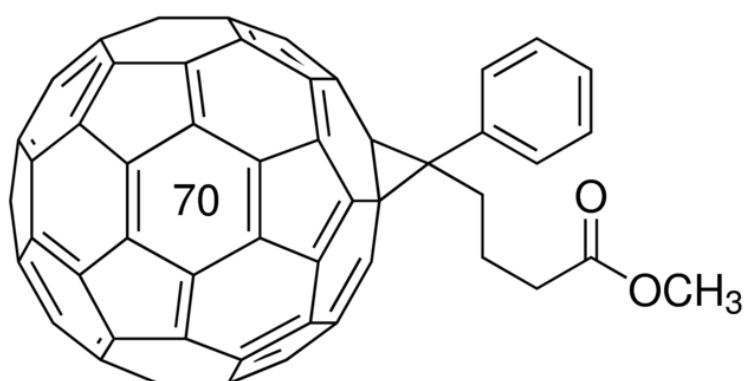


Figure 10 [70] PCBM chemical structure [figure taken from Sigma-Aldrich website¹⁴]

2.4 Cu₂O absorber

The research in photovoltaics is focused to future large scale solar cell production at a low-cost. Cuprous oxide is a prominent light absorber which is recognized as a promising material in all-oxide solar cells^{15,16}.

Cu₂O has been first recognized as a Cu₂O Schottky junction in the early 20th century but since the difficulty of n-type doping became prominent further advancement have been sporadic.^{17,18}

“In a recent study, Cu₂O appears as one of the most intriguing among 23 inorganic absorbers for abundant and affordable electricity supply, based on the dual constraints of material supply and lowest cost per watt”^{19,20} Cuprous oxide is abundant in high quantities on earth and non-toxic. Apart from these properties it is air-stable and can be prepared by non-vacuum techniques such as deposition electrochemical deposition from solution and thermal oxidation of copper sheets.

Cuprous oxide is an intrinsic p-type semiconductor since the high concentration of copper vacancies are negatively charged and it probably contains interstitial oxygen defects.²¹ Cu₂O has a cubic unit cell structure and a direct band gap with an energy of 1,8 – 2 eV dependent on the deposition conditions. Because of the direct band gap, the absorption coefficient (more than 10^3 cm^{-1})²² of cuprous oxide is relative high which is why this material is an ideal candidate as an absorber in thin film solar cell structures. The band gap is quite large to be an ideal match for the solar spectrum (compare with Figure 4) but the theoretical maximum power efficiency calculated by the Shockley-Queisser limit still reaches approximately 20% under standardized AM1.5 illumination.^{5,18,19,23}

As mentioned above Cu₂O is a p-type with a majority carrier mobility in the range of $100 \frac{\text{cm}^2}{\text{Vs}}$.^{18,24} For further p-type doping, Cl and N are suitable dopants known for Cu₂O whereas the n-type doping has been very difficult due to the mechanism of dopant self-compensation.^{18,25} In recent times there have been successfully engineered Cu₂O-homojunctions reported^{26,27} but since the efficiencies are very low the research focus lies mainly on heterojunctions with Cu₂O as the absorber. The most promising n-type layers to form the heterojunctions have been up to date Ga₂O₃²⁸ and ZnO.

Especially ZnO has been studied thoroughly as an n-type window layer for Cu₂O. An efficiency of 1,4% for electrochemical deposition of first n-type ZnO and then p-type Cu₂O²⁹, an efficiency of 2,8 for ALD of ZnO on top of electrodeposited Cu₂O³⁰ and 4,1% for thermally oxidized Cu₂O by PLD with ZnO as n-type to form the heterojunction³¹.

2.5 SAM [Self Assembled Molecules]

SAMs [Self Assembled Molecules] are organic assemblies which form spontaneously by chemical adsorption on the substrate surface. When deposited upon a surface the molecule spontaneously forms a densely packed two-dimensional layer. This layer alters the surface and interfacial properties and adds various possibilities for applications.^{32,33}

The basic structure of SAMs can be seen in Figure 11. The head group connects the molecule to the substrate surface due to adsorption. The tail group separates the head and the functional part of the SAM. The end-group defines the properties of the new layer. By changing the functional-group the surface can be modified like for example changing it from hydrophobic to hydrophilic.³³

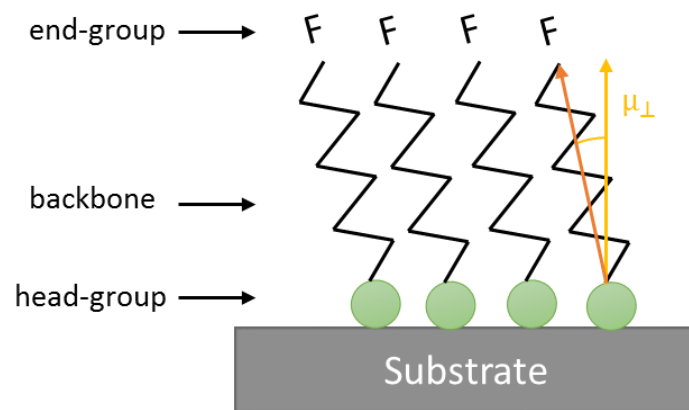


Figure 11 schematic structure of SAMs

2.5.1 Electronic properties

The electrical properties of SAMs are of particular interest for interfacial studies. With the resulting work function shift induced by the adsorbed SAMs it is possible to modify and improve an interface. This has been investigated theoretically³⁴ as well as experimentally.^{35,36}

The electric dipole is fundamentally defined as:³⁷

$$\mu = qd$$

eq. 6

With d as the displacement vector and q as the charge. The dipole moment points from the negative charge to the positive one.

The work function modification can be interpreted by the absorption of the SAM- layer. The permanent dipole of the molecule influences the properties and magnitude of the surface potential. It is necessary to note that only the dipole component perpendicular to the surface normal affects the work function. Therefore the gas-phase dipole moment of molecules changes with the absorption.³⁸

The change in work function $\Delta\Phi$ can be derived from the Helmholtz equation.³⁹

$$\Delta\Phi = \frac{q N \mu_{\perp}}{\epsilon_0 \epsilon_r} \quad \text{eq. 7}$$

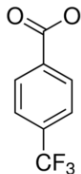
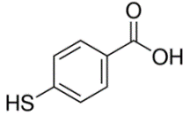
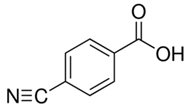
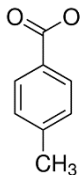
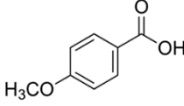
With the electric charge q , the surface dipole moment μ_{\perp} perpendicular to the surface, the vacuum permittivity ϵ_0 , the relative dielectric constant ϵ_r and N the surface dipole density.

2.5.2 Benzoic acid derivate

A number of benzoic acid derivatives have been selected and are listed in Table 1. All derivatives were ordered from Sigma-Aldrich. To influence the direction of the interfacial dipole three derivatives with a net positive dipole moment have been selected (tfba, meba and cba) as well as two derivatives with a net negative dipole moment (tba and mba).

It is worth noting that the dipole notated in the table is the gas-phase dipole moment. This moment will change due to the absorption, interaction with the surface and the tilt angle as discussed in the previous chapter. The formed interfacial dipole will diverge to the one gas-phase moment.

Table 1 summary of benzoic acid derivatives

Name [a]	Abbreviation [b]	Structural formula [c]	Gas-phase dipole moment [d]
4-(trifluoromethyl) benzoic acid	tfba		+2.1 D [1], +2.7 D [3]
4-mercaptobenzoic acid	meba		+1.5 D [1]
4-cyanobenzoic acid	cba		+3,7 D [2], +2.3 D [3]
p-Toluic acid	tba		-2.9 D [1], -4.0 D [3]
4-methoxybenzoic acid	mba		-2.9 D [1], -3.7 D [2], -4.4 D [3]

[a] IUPAC name of the derivative. [b] Abbreviation used for further experiments in this thesis [c] All structural formula images taken from the Sigma-Aldrich website. [d] The source for each reported gas-phase dipole moment has been noted with: [1] Yip et al.[2008]⁴⁰, [2] Rühle et al.[2005]⁴¹ and [3] Haick et al.[2004]⁴²

3 Characterization methods

3.1 AFM [Atomic Force Microscopy]

The atomic force microscope is a high-resolution microscope with a resolution of less than 1 Å. It was first introduced by Binnig in 1986⁴³ and is nowadays an important surface characterization tool.

It basically consists of three main parts: the cantilever with the tip, a laser and a photodiode. The AFM operates by measuring the force acting between the surface and the tip. The force causes lateral and vertical deflections of the cantilever. These deflections can be monitored by the photodiode which registers small changes in the reflected laser beam.

To image the surface topography two modes are used in the AFM: (a) contact mode and (b) the non-contact mode. Both modes have their advantages and disadvantages like the damage due to high forces in case (a) or the influence of a thin water film in mode (b). This is why an intermittent mode has been introduced, the tapping mode. Its imaging is similar to the contact mode but the cantilever is oscillated in resonance frequency. The tip taps on the surface during its oscillation and by maintaining a constant amplitude of oscillation the topography contrast can be measured.⁴⁴

The AFM used in this thesis has been the Dimension V model from Veeco with a Nanoscope V controller. The device has been used in controlled air environment, an ISO 14644 certified clean room.

3.2 KPFM [Kelvin Probe Force Microscopy]

3.2.1 Working principle⁴⁵

The KPFM measures the contact potential difference (V_{CPD}) between a conducting tip and the sample surface:

$$V_{CPD} = \frac{\Phi_{tip} - \Phi_{sample}}{-e} \quad \text{eq. 8}$$

with Φ the work function of tip and sample and e the electronic charge.

The measuring principle of can be explained by energy diagrams of the tip and sample system (Figure 12). In the first picture (a), the tip and the sample are in equilibrium and a finite distance d apart from each other. Both share the same vacuum level E_{VL} but since they are not in contact their Fermi levels differ. When brought in electrical contact (b) the Fermi levels of the materials will align through an electron current flow. As a consequence, the vacuum levels will shift and the surface of the sample and tip will be charged respectively. A potential difference V_{CPD} will form and act as an electric force on the

contact area. This can be compared to a simple capacitor model. This force can be nullified by applying an external bias V_{DC} has to be applied (c). When V_{DC} equals the magnitude of the potential difference V_{CPD} with the opposite direction, the surface charge in the contact area gets eliminated. This amount of applied bias is exactly the work function difference between tip and sample.^{45,46}

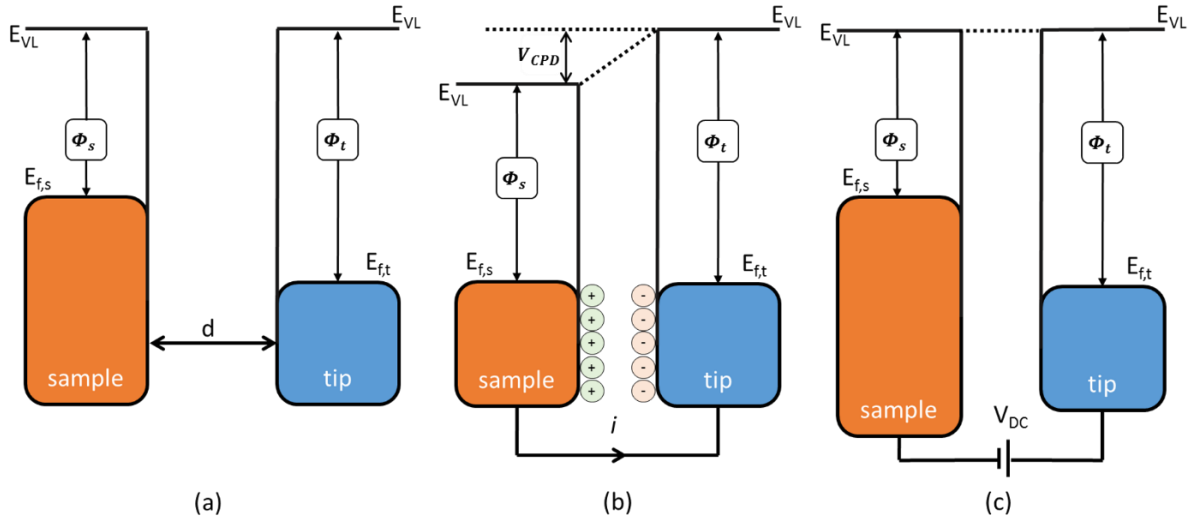


Figure 12 Electronic energy levels of the tip-sample system for three different cases: a) equilibrium & no contact b) contact & no external bias c) contact & external applied bias

The electrostatic force F_{es} acting between the tip and the sample can be expressed by:

$$F_{es}(z) = -\frac{1}{2}\Delta V^2 \frac{dC(z)}{dz} \quad \text{eq. 9}$$

where $\frac{dC(z)}{dz}$ is the gradient of the capacitance between the two surfaces with a dependence on the z direction normal to the surface and ΔV the voltage difference .

The CPD is measured by applying an AC- voltage ($V_{ac} = V_{AC}\sin(\omega t)$) and a DC-voltage V_{DC} to the tip. V_{ac} causes the cantilever to oscillate and the V_{DC} is used to nullify the electric force interfering with the oscillation caused by the CPD.

The voltage difference ΔV between the tip and the sample surface can be expressed by:

$$\Delta V = [V_{tip} \pm V_{CPD}] = (V_{DC} \pm V_{CPD}) + V_{AC}\sin(\omega t) \quad \text{eq. 10}$$

The sign of \pm is dependent whether the bias V_{DC} is applied to the tip (-) or the sample (+).⁴⁵

3.3 Fourier transform infrared spectrometer (FTIR)

The FTIR used in this thesis has been a Bruker Vertex 70 which has been equipped with an additional source for visible and un-polarized light. To record a spectrum in the range of 330 – 550 nm a GaP detector has been used. For a higher wavelength range of 550- 1200 nm a Si detector has been used. The FTIR has been used for measuring transmittance and reflectance.

The transmittance has been measured in reference to air with normal incident light.

The reflectance has been measured with an additional equipment (A513QA) for the FTIR at 13° deflections of incident and un-polarized light. The reference for the measurement signal has an aluminum coated calibrated mirror for the first wavelength range of 330- 550 nm and a Au-coated substrate for the second wavelength range of 550 – 1200 nm. The reflectance has been measured from the Cu₂O side.⁴⁷

3.4 XRD

X-ray diffraction measurements to measure the crystallographic structure of the substrate have been performed using a Bruker AXS D8 Discover Horizontal X-ray diffractometer.

The radiation has been Cu-K α and the device have been equipped with a Göbel mirror and a two-dimensional general area detector diffractometer system.⁴⁸

3.5 Electrical device characterization

The lamp for the illumination has been a LOT QuantumDesign fabricated halogen lamp operated at standardized AM 1,5 1000 W/m². The IV-curves have been measured and recorded by an Agilent “4156C Precision Semiconductor Parameter Analyzer “.

3.6 SEM [Scanning Electron Microscopy]

Scanning electron microscopy is a widely used tool to analyze the surface topography of a sample. A focused electron beam is used to raster across the specimen surface. The impinging electrons interact with the surface and produces a variety of different types of signals like the secondary electrons (SE), backscattered electrons (BSE) and characteristic x-rays. The SEM mostly focuses on the secondary and backscattered electrons since these signals vary according to the difference in surface topography. In this experiment only the SE have been detected and used, since the emission of secondary electrons is confined to a relative small volume near to the impact zone of the electron beam. This results in relative high resolution images.⁴⁹ The SEM used in this thesis has been a GEMINI Zeiss Supra 40.

4 Solar cell fabrication procedure and design

4.1 Design of the heterojunction solar cell

The inorganic absorber used in this thesis is Cu_2O , which has been produced by electrochemical deposition. The organic n-type semiconductor PCBM has been selected to form the heterojunction with cuprous oxide.

Two different architectures (Figure 13) have been selected: one with a Au (100 nm) bottom electrode and one with an ITO(50nm)/Au(5nm)/ITO(50nm) bottom electrode. Both electrodes have been sputtered on a glass substrate. These conductive electrodes have been used for the electrodeposition of a thin cuprous oxide layer ($\sim 2\text{-}3\ \mu\text{m}$). On top of the Cu_2O the organic semiconductor (OSC) has been spin coated. As a top electrode the transparent conductive oxide (TCO) AZO has been selected.

SAMs has been used to modify the electronic structure of the hybrid p-n junction. They have been spin coated as an additional interfacial layer in-between the Cu_2O and the PCBM.

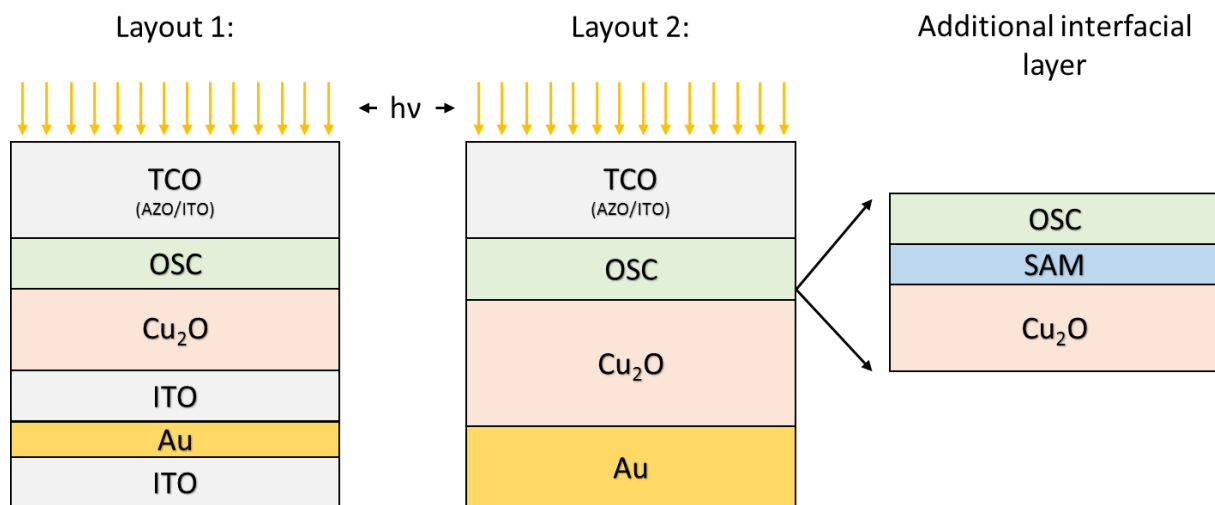


Figure 13 design layout of the hybrid solar cell

4.2 Substrate preparation

The glass substrates have been cleaned in a three step procedure in an ultrasonic bath. First deionized water (18,2 Ω) has been mixed with 2 ml of HELLMANEXTM a cleaning agent from Sigma-Aldrich. In a second and third step acetone and isopropanol has been used to clean the glass substrates from residual organic waste.

The bottom electrodes were deposited in a DC – magnetron sputtering system (Leybold Univex 450C) in pure argon atmosphere. Au has been selected as an electrode because of its properties necessary for the characterization of the solar cell in further experiments. The high conductivity of Au leads to a higher nucleation rate in the electrochemical deposition. This results in a finer grain structure and lower roughness of Cu₂O. The roughness is a decisive factor for the accuracy of the kelvin probe measurements. To get better adhesion, a thin layer of tantalum (~5 nm) is introduced as a sticking layer. The thickness of the Au is approximately 100 nm. The Au-layer is non transparent and the measured sheet resistance is approximately $1 \frac{\Omega}{sq}$.

As a second electrode indium tin oxide (ITO) has been used. To improve the conductivity of ITO, a thin layer of Au (~5 nm) has been sputtered in the middle of two 50 nm ITO-layer (105 nm in total). In further descriptions this electrode will be denoted as IMI. The IMI layer is transparent (see Figure 14) and the measured sheet resistance is approximately $15 - 20 \frac{\Omega}{sq}$

The sputtering parameter are listed in Table 2 .

Table 2 sputtering parameter bottom electrode

Material	Power	Deposition rate	Pre sputtering	Pressure	Inert Gas
ITO	40 W	0,235 nm/s	200 s	0,002 mbar	Ar
Au	20 W	0,626 nm/s	10 s	0,002 mbar	Ar
Ta	20 W	0,060 nm/s	10 s	0,002 mbar	Ar

The illumination from the top has been selected because of the high absorption coefficient of cuprous oxide. Therefore, an illumination from the glass-side is not efficient since no photons would reach the active interface region which can be seen in Figure 14. The transmission has been measured by the FTIR.

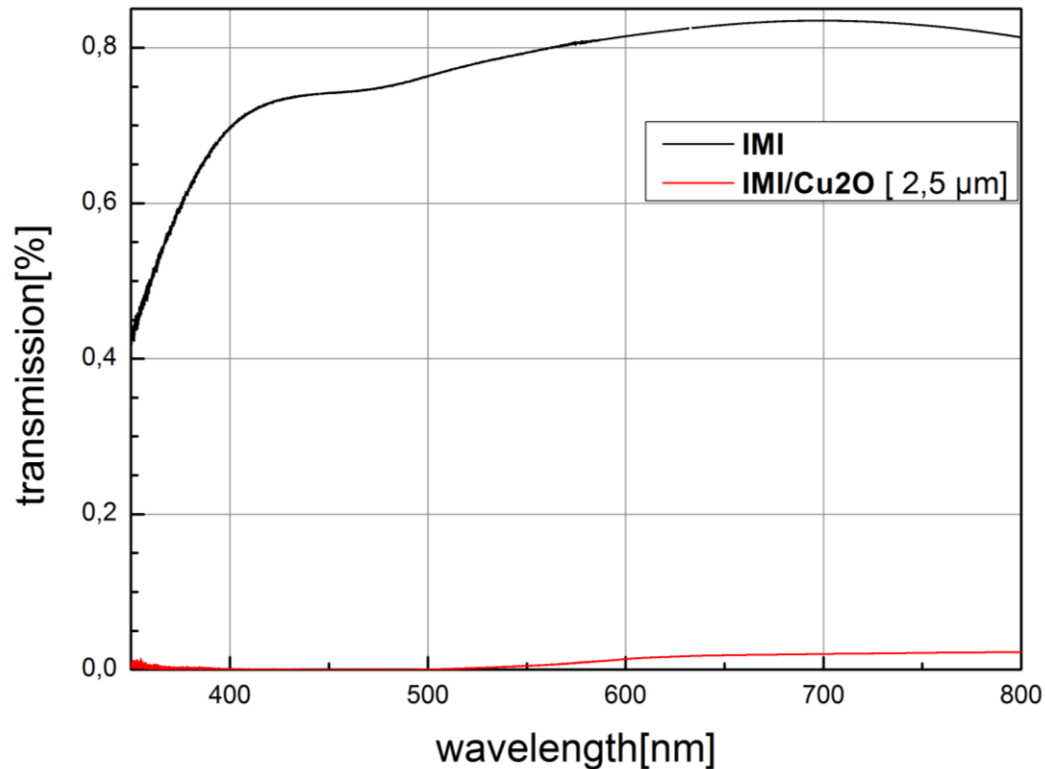


Figure 14 light absorption of Cu₂O on a IMI electrode and ITO-layer

4.3 Electrochemical deposition of cuprous oxide

As introduced in chapter 2.4 cuprous oxide has been used as the inorganic p-type absorber. The layer has been electrochemically deposited on the sputtered electrodes.

4.3.1 Theoretical background of electrochemical deposition

Electrochemical deposition (ECD) is a technique in which a material is grown on a conductive substrate due to the reduction of ions from an electrolyte. The used electrolyte is generally aqueous. The grown material can either be a metal, a metallic alloy or a semiconductor. The reduction of metal Ions M^{z+} in an aqueous solution is given by⁵⁰



To accomplish this process z electrons e are to be provided by an external circuit which is then called electrodeposition (or electroplating).

The material properties can be controlled by various parameters, e.g. the pH, the temperature and the applied potential. With an optimization of these parameters it is possible to grow well defined films of desired structure and composition. The biggest advantages of electrodeposition are “simplicity, low cost, scalability, and manufacturability”⁵¹.

An electrochemical cell has at least two electrodes but normally consist of three, namely the working electrode WE, the reference electrode RE and the counter electrode CE. The overall electrochemical reaction, the redox reaction, consist out of two independent half reactions. In case of ECD the half-reaction of interest is, as mentioned above, the reduction. The working electrode is the electrode where the reduction takes place. The electrically conductive electrode can be either a metal or for instance in solar cells a TCO (transparent conductive electrode). To get a current flowing oxidation has to take place on the counterpart, the counter electrode. The potential of the working electrode is monitored by the reference electrode. The reference electrode has a high input impedance so its potential will remain constant.^{50,51} A schematic illustration of the setup has been added in Figure 15.

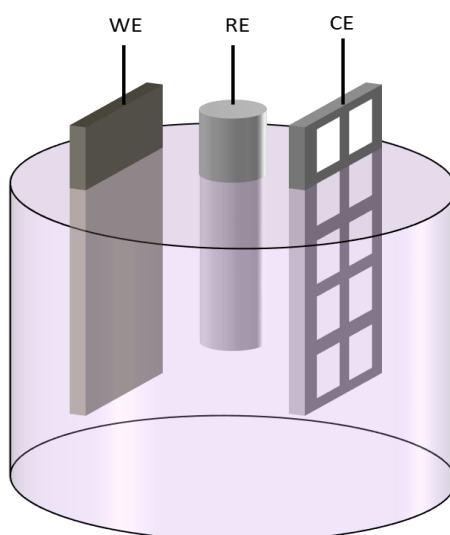
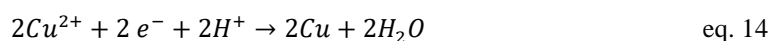
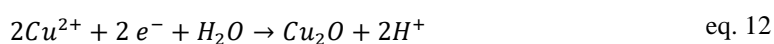


Figure 15 potentiostatic electrodeposition setup

4.3.2 Experimental influences of ECD of Cu₂O-absorber

During the cathodic reduction of Cu²⁺ ions, three reactions occur:⁵²⁻⁵⁴



It is important to note that the first and the third reaction (eq. 12 and eq. 14) are pH dependent.⁵⁴

A low pH value of the electrolyte solution (lower than pH 7) forms metallic copper according to the third reaction. The first and the second reaction (eq. 12 and eq. 13) can be controlled by the applied potential.

Two very important parameters in the electrochemical deposition of cuprous oxide are the pH-value and the temperature. A very well-known aqueous solution consists cupric sulfate and lactic acid. The lactic acid acts as a complexing agent and stabilizes the copper ions. As mentioned above (eq. 12 and eq. 14) it is necessary to increase the pH of the solution in the alkaline region with the addition of sodium hydroxide. Numerous groups reported the ideal pH-range to be between 9 – 12. With an increase of the pH it is also possible to influence the orientation of the Cu_2O -planes. In case of the often used pH of 12,5 cuprous oxide grows preferred in the (111) orientation.^{52,54,55}

With the temperature the diffusion of ions can be controlled. Since the diffusion current at RT is not sufficient, a bath temperature of $> 50^\circ\text{C}$ is used.^{52,54,56}

For the experiments, an electrolyte solution has been prepared using 0,2 M copper(II) sulfate pentahydrate ($\text{CuSO}_4 \cdot 5\text{H}_2\text{O}$), 3 M of lactic acid, de-ionized water ($18,2\Omega$) and approximately 2 M sodium hydroxide (NaOH) to adjust the pH-value to 12,5 in a 500 mL solution. All of the ingredients have been ordered from Sigma-Aldrich. This aqueous solution is widely used and characterized to electrodeposit Cu_2O .^{55-57,30,58}

The electrodeposition has been carried out potentiostatically on the Autolab PGSTAT 128N-Potentiostat at 50°C . The reference electrode used has been a Ag/AgCl.

To evaluate the deposition potential according to eq. 12 - eq. 14 a cyclic voltammogram has been performed. The scan rate was 10 mV/s starting from a slightly positive potential of 0,05 V to a negative potential of $-1,0$ V.

An example voltammogram for the Au-electrode (black line) and IMI-electrode (red line) is illustrated in Figure 16 in order to achieve an overview to the potential range selection. For this case the deposition range for the cuprous oxide deposition has been from -0,45 to -0,65 V vs Ag/AgCl for the IMI-electrode and -0,28 to -0,32 V vs Ag/AgCl for the Au electrode. At a potential higher than the selected range additionally to the cuprous oxide copper starts to deposit (eq. 13). The selected deposition range of Cu_2O is comparable to literature results.^{52,54,55}

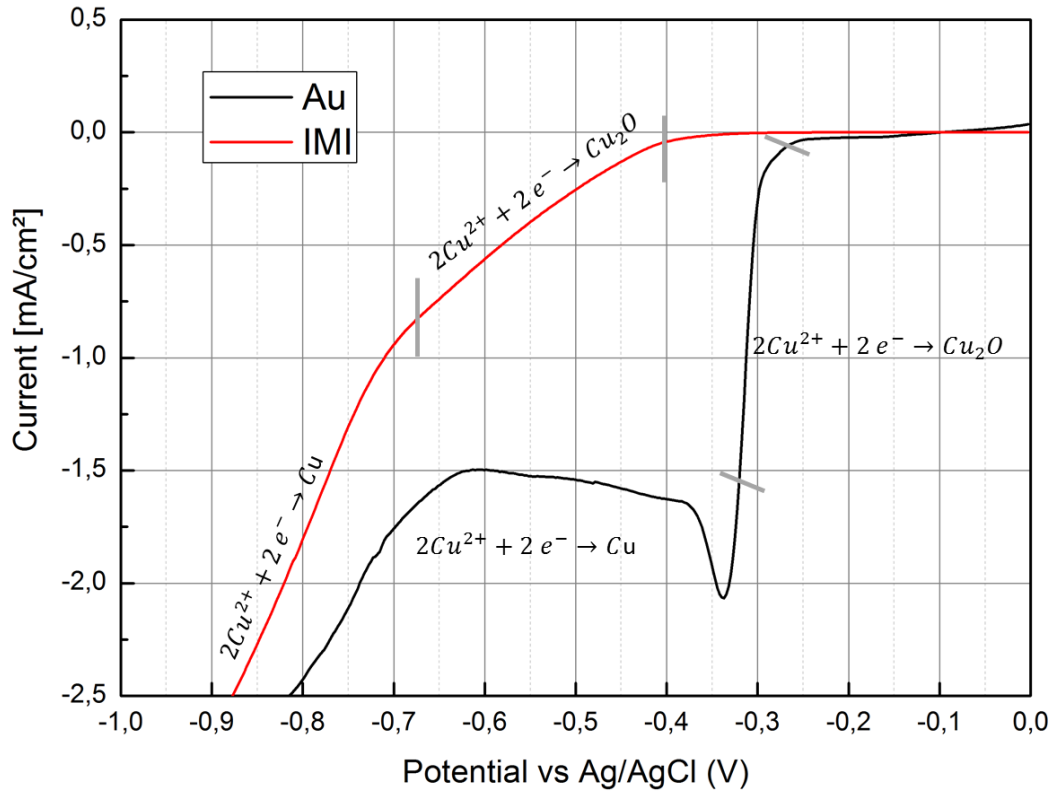


Figure 16 cyclic voltammogram of Cu_2O for ITO and Au

The thickness of the deposited film can be approximated by Faradays law by measuring the charge Q passed through the electrolyte:⁵⁹

$$Q = \frac{mFz}{M} = V \frac{Fz\rho}{M} = At \frac{Fz\rho}{M} \quad \text{eq. 15}$$

With m the mass of deposited material, F the faraday's constant, z the valence number, M the molar mass, V the volume, ρ the density, A the deposited area and t the thickness of the deposited film.

In the following chapters the influence of the different bottom electrodes in Au and IMI will be reviewed with respect to the electrodeposition process and the resulting properties. To characterize the layers, the AFM and the SEM has been used. (see chapter 3)

4.3.3 Cu_2O structure on Au bottom electrode

In a first set of experiment the sputtered Au electrode has been used as the bottom electrode. The deposition from the solution has been carried out at an appropriate fixed potential selected from the

cyclic voltammetry. The thickness was approximated to $t = 2,5 \mu\text{m}$ with eq. 15 by defining the necessary charge to pass through the electrode area.

In Figure 17 a deposition curve for three different deposition potentials has been plotted. The first larger picture shows an overview of the whole deposition process. As seen in the voltammogram too, an increasing potential increases the absolute value of the deposition current, decreasing the time necessary to reach the desired charge and therefore thickness. In the zoomed-in picture the same curves are plotted for the first 200 seconds. Since the metal electrode is very conductive, a high amount of nucleation can take place in a relative short period of period of time. The high increase of absolute value of the current in this case is related to the growth of the nuclei that increases the effective area of the surface. Around these nuclei, diffusion zones emerge which will increase until a maximum point and then start overlapping. The current then starts decreasing until it reaches a plateau. This plateau-region is diffusion controlled.⁶⁰⁻⁶²

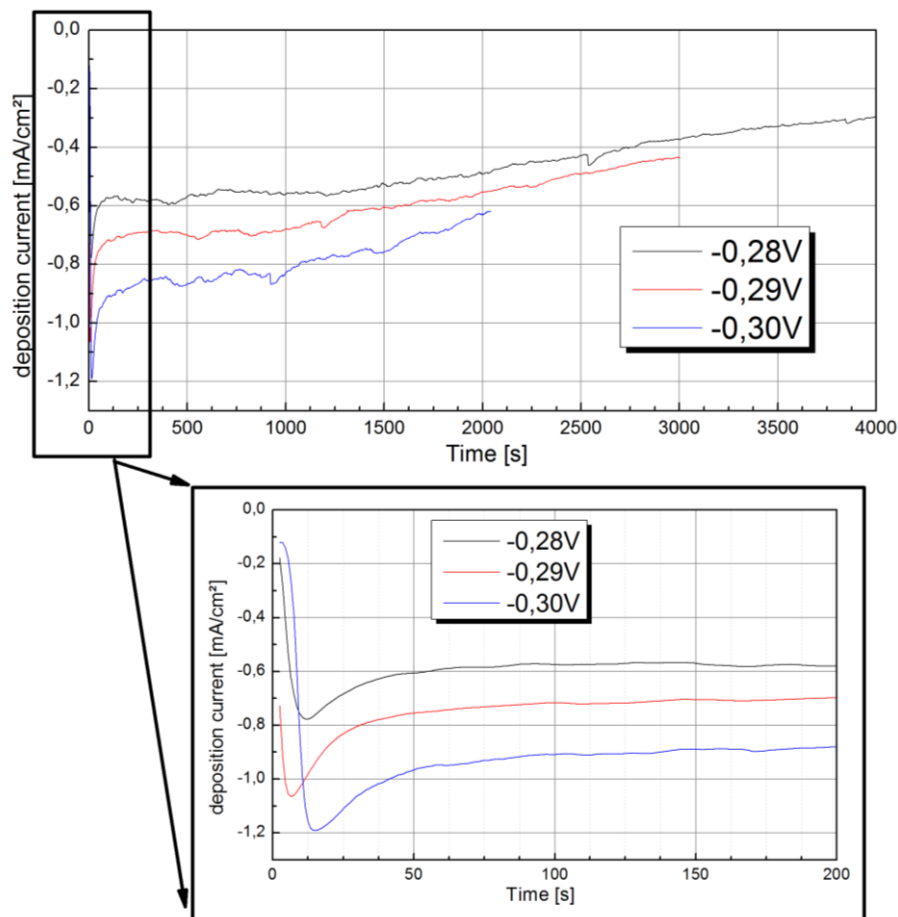


Figure 17 Current- time transients of Cu_2O deposited on Au bottom electrode at different deposition potentials

To illustrate the dependence of the deposition potential on the grain structure SEM as well as AFM surface pictures haven been taken.

At first, surface pictures of two samples with a deposition potential of $-0,28\text{ V}$ and $-0,29\text{ V}$ have been taken. In both pictures (Figure 18 and Figure 19) the surface topography of the cuprous oxide film can be seen at two magnifications. From these pictures little to no difference in the surface of the cuprous oxide surface can be seen. This behavior is expected since the conductivity of the Au-electrode is very high (resistivity $\sim 1 \frac{\Omega}{sq}$)

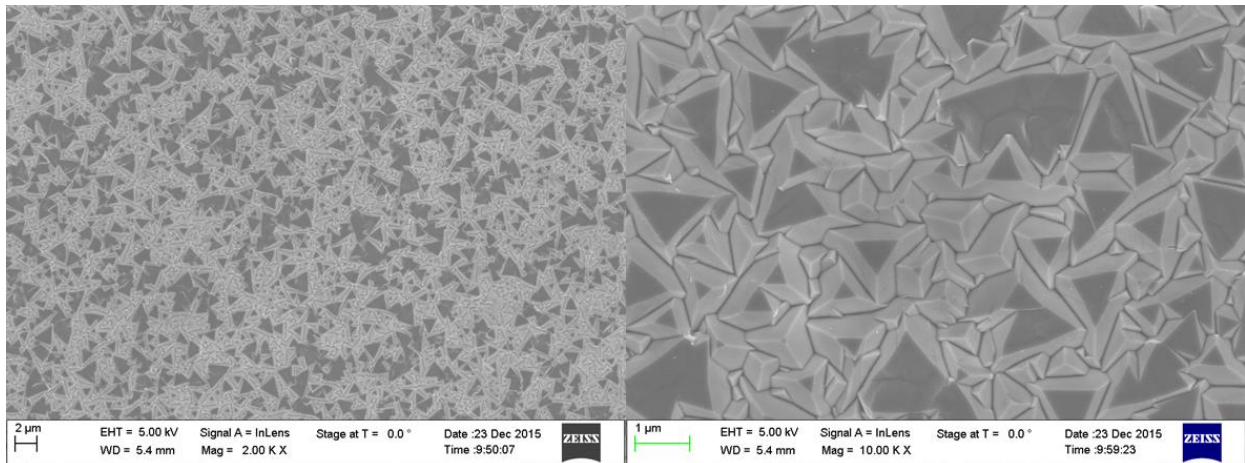


Figure 18 SEM picture of electrodeposited Cu_2O with a deposition potential of $-0,28\text{ V}$ on a Au bottom-electrode a) 2k magnification b) 30k magnification

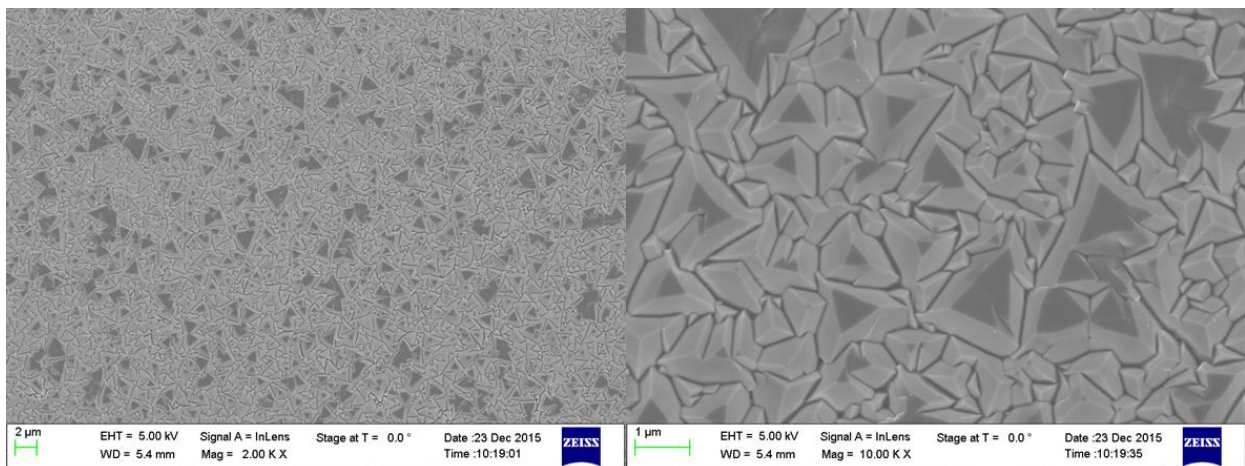


Figure 19 SEM picture of electrodeposited Cu_2O with a deposition potential of $-0,29\text{ V}$ on a Au bottom-electrode a) 2k magnification b) 30k magnification

To verify the thickness of the sample a cross-section images were taken by SEM. In the first picture of Figure 20 the thickness of the Au layer and the absorbing Cu_2O have been drawn. In the second picture the sample has been tilted.

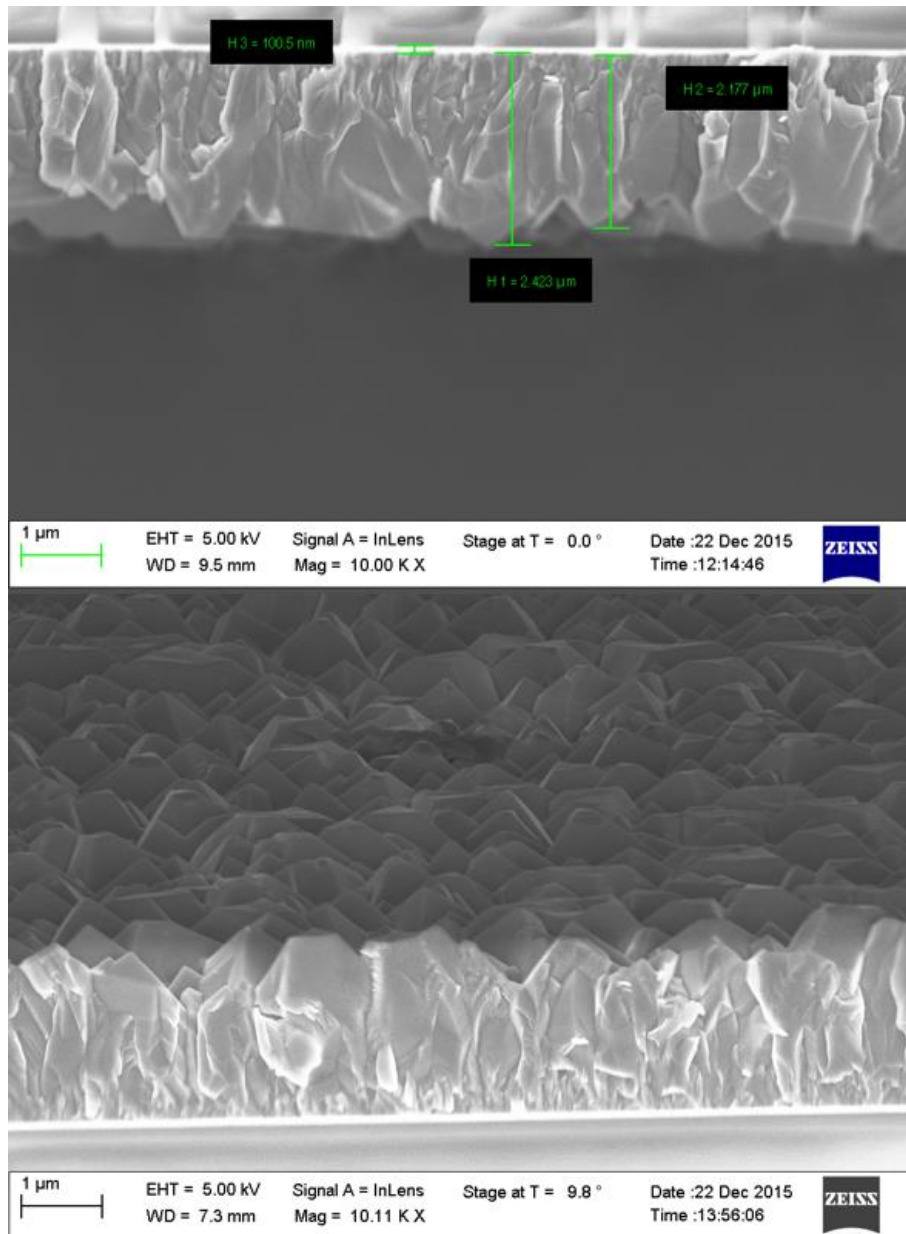


Figure 20 SEM cross-section of Cu_2O on an Au bottom-electrode

To quantify the surface roughness AFM experiments have been carried out.

An example surface height profile of a Cu_2O - substrate prepared at a deposition potential of $-0,29\text{ V}$ on an Au electrode has been added in Figure 21. In the left picture the scanning-area has been $50 \times 50\ \mu\text{m}$ whereas the right one has been performed on an area of $10 \times 10\ \mu\text{m}$ on the same sample.

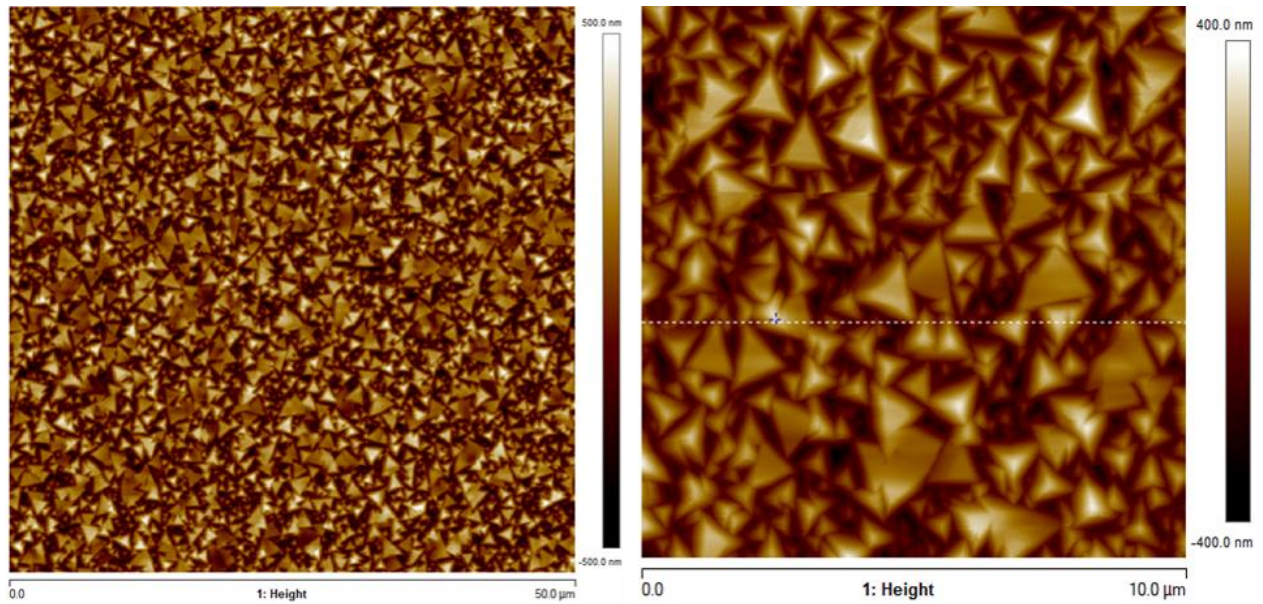


Figure 21 AFM picture of electrodeposited Cu_2O on a Au bottom-electrode

Additionally, a typical height profile has been taken from the right picture (white line) and has been added in Figure 22.

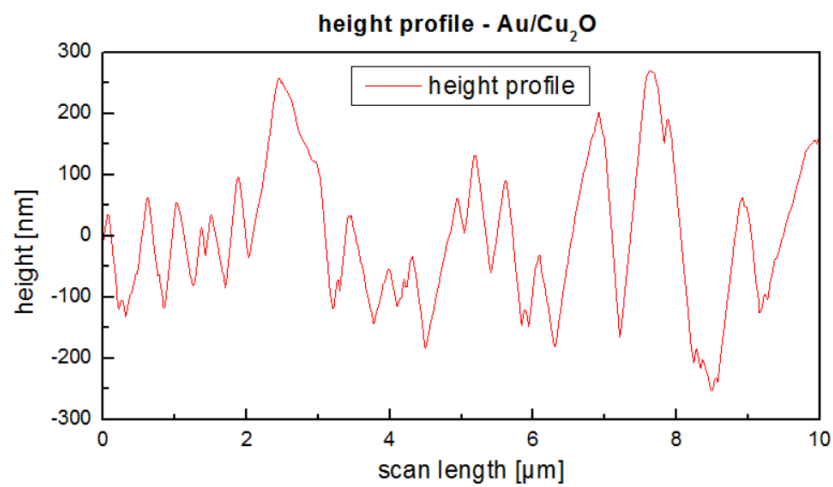


Figure 22 height profile of Cu_2O on Au electrode - taken from Figure 21 (white line)

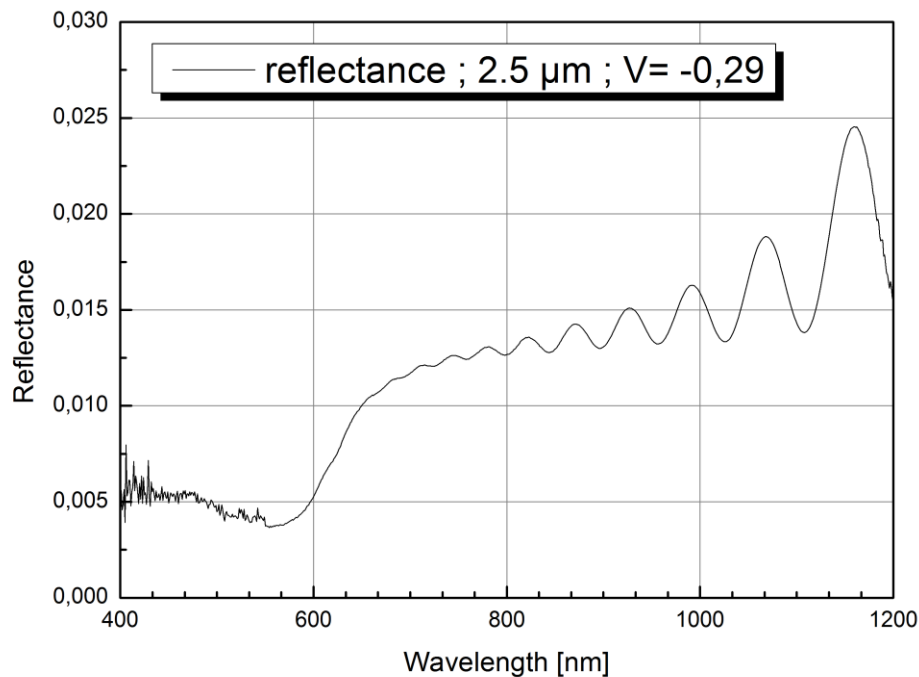
The surface roughness has been calculated from the AFM height pictures using the software NanoScope Analysis. Three different deposition potentials have been chosen to compare the average roughness. The calculated results are listed in Table 7.

Table 3 surface roughness comparison - Au electrode

<i>electrode</i>	deposition potential	surface roughness R_{RMS}
Au	- 0,28 V	$(157 \pm 6) \text{ nm}$
Au	- 0,29 V	$(151 \pm 5) \text{ nm}$
Au	- 0,30 V	$(164 \pm 3) \text{ nm}$

It has been expected that a lower surface potential leads to a rougher structure. Since the Au electrode is very conductive and the difference in the potentials is very low, all the roughness values are comparable. Nevertheless, it has to be considered that the electrochemical deposition is only partially controllable due to various influencing factors e.g. the charge transfer, temperature-value, concentration of ions. Depending on the influencing factors the surface roughness will change.

In addition to the AFM and SEM measurement a reflectivity measurement has been performed on the Au/Cu₂O surface prepared with a deposition potential of 0,29V and a thickness of 2,5 μm . The used FTIR has been described in chapter 3.3. The reflection curve has been plotted in Figure 23. The oscillations which starts at higher wavelength can be explained by interference. Since these wavelengths correspond to a lower energy than the band gap energy the light can penetrate through the sample where it will be reflected at the Au electrode. The reflected light then interferes with the incident light depending on the phase either constructive or destructive.

Figure 23 reflectivity measurement of Cu₂O - sample

From the reflectance it is possible to calculate the band gap of the measured material. This has been done by plotting the reflectance over the energy in electron volts. The intercept of the two slopes on the on-set edge of the reflection is defined to be the band-gap. The measured band-gap of 1,9 eV, which is in good accordance to the reported values.^{30,63,64}

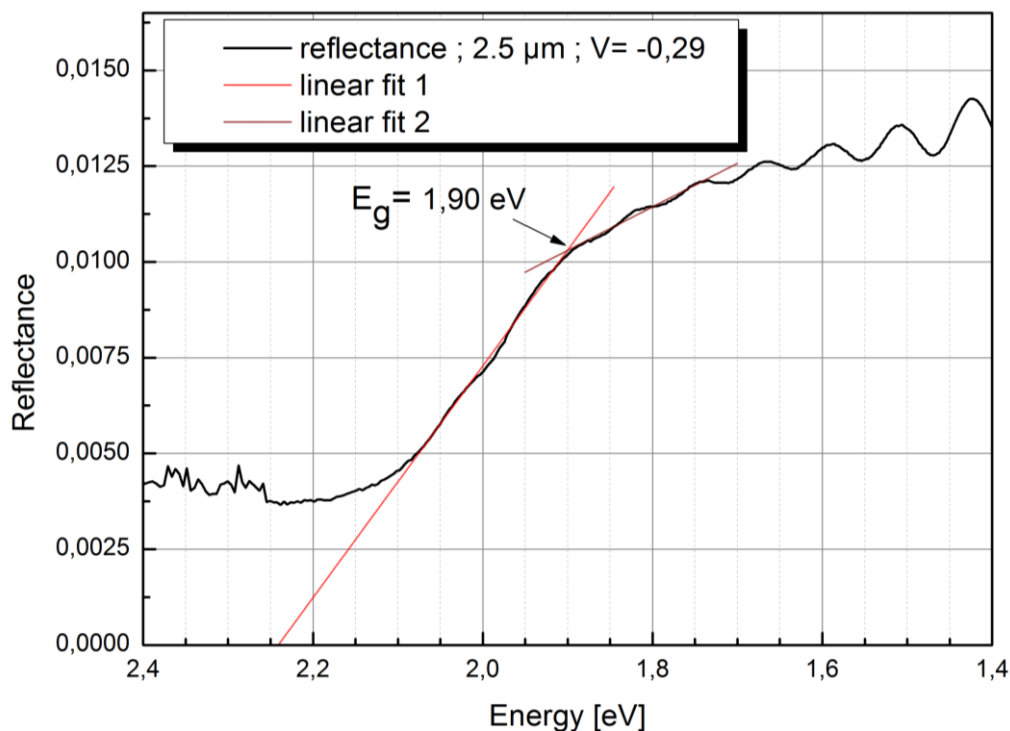


Figure 24 reflectance measurement - Cu₂O - band gap

The Au/Cu₂O structure has then been analysed using the XRD. The sample used has been electrochemically deposited on an Au electrode with a potential of -0,29 V and 2,5 μm thick. The element data used to analyse the XRD-pattern has been added in Table 4.

Table 4 Element data used to analyze the XRD

name	Common name	Reference code
Cu₂O	Copper(I) oxide	01-077-0199
Au	Au	03-065-2870

In Figure 25 the XRD pattern has been plotted and the resulting peaks have been identified. The identified plane reflections have been marked in the figure and the detailed results have been added in Table 5.

From the results it is clear to see the main peak at the cuprous oxide (111)-plane. These measurement results show very good accordance to the predicted and previously reported pH-dependence in electrodeposited cuprous oxide. (see chapter 4.3.2)

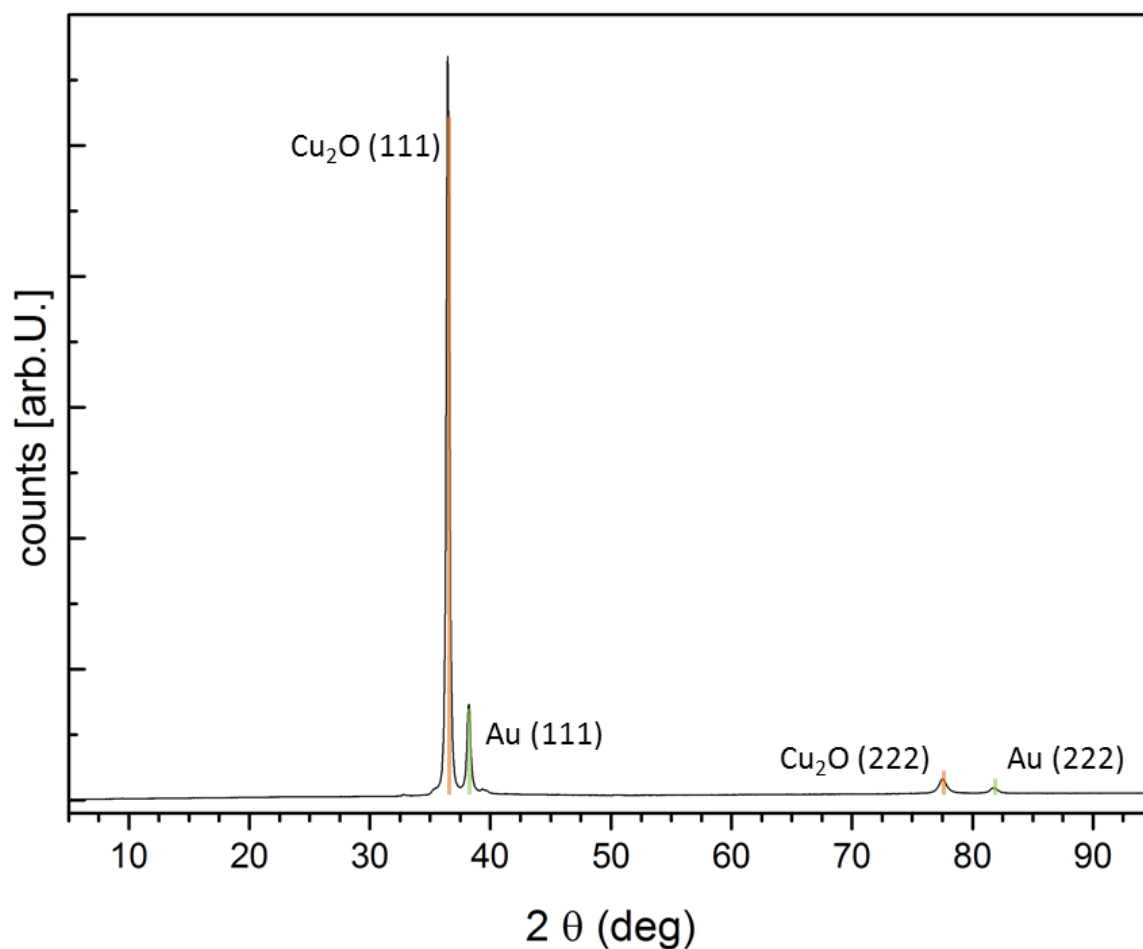


Figure 25 XRD-pattern of Au/Cu₂O structure

Table 5 Identification of the resulting XRD peaks

name	Peak No.	Plane [hkl]	D [Å]	2θ[deg]
Cu₂O	1	(111)	2,45836	36,521
Cu₂O	2	(222)	1,22918	77,611
Au	1	(111)	2,35478	38,188
Au	2	(222)	1,17739	81,726

4.3.4 Cu_2O structure on IMI bottom electrode

The second material used as a bottom electrode has been IMI (ITO/Au/ITO structure, chapter 4.2). The grain size of the Cu_2O on the IMI-electrode is larger than on the Au-electrode. This results from the higher resistance of IMI compared to the metal Au. Therefore, less nucleation sites are formed during the electrochemical deposition process which increases the grain size. This behaviour can be seen in Figure 26 in which compared to the layout with the Au electrode no sharp increase of the deposition current occurs in the first time period. This indicates a lower nucleation rate with a continuous grow of the nuclei resulting in a larger grain size.

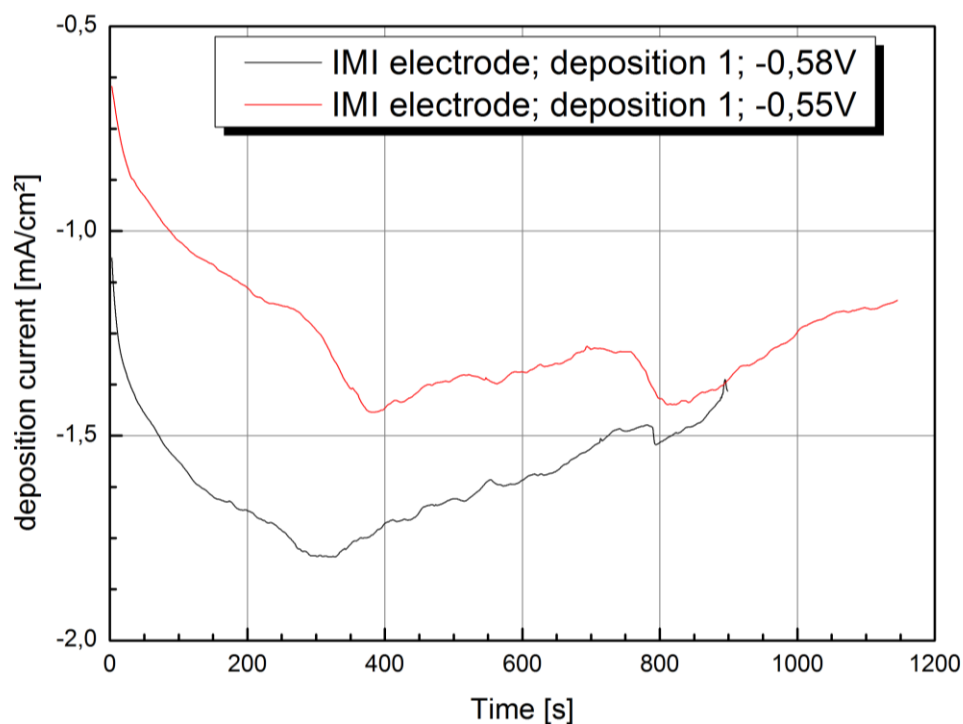


Figure 26 Current- time transients of Cu_2O deposited on IMI bottom electrode at different deposition potentials

The SEM pictures illustrate the difference in the grain size for the IMI- electrode compared to the Au - electrodes. (Figure 27) The sample used for the SEM picture has been prepared with a deposition potential of $-0,58\text{ V}$.

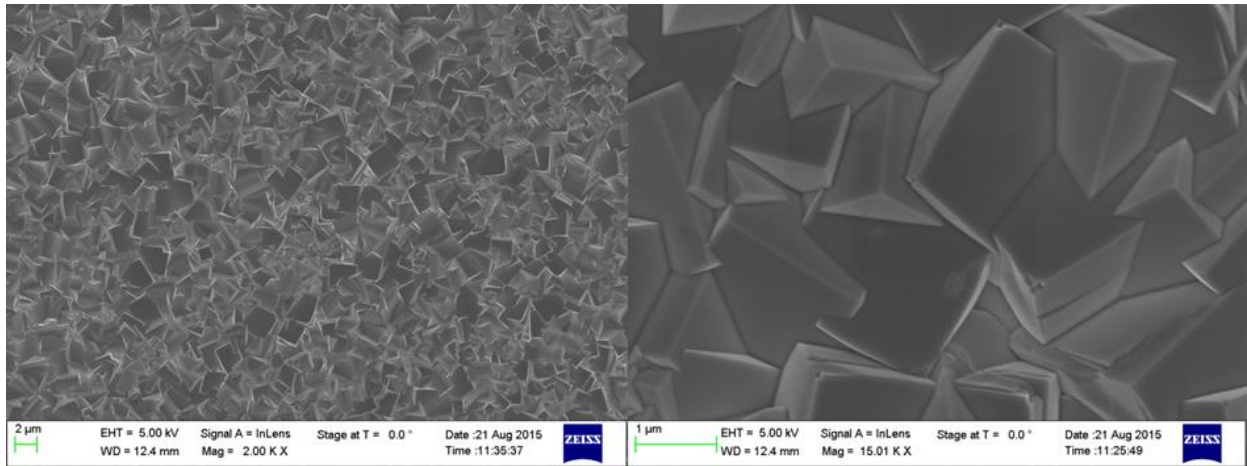


Figure 27 SEM picture of Cu₂O on a IMI bottom-electrode a) 2k magnification b) 15k magnification

The same sample used in the SEM has been used for further characterization in the AFM. The height profile of this sample can be seen in Figure 28. To compare it to the Au case the same scan areas have been chosen in 50×50 μm and 10×10 μm. For the smaller scan area, a height profile of one scan line has been taken and drawn in Figure 29.

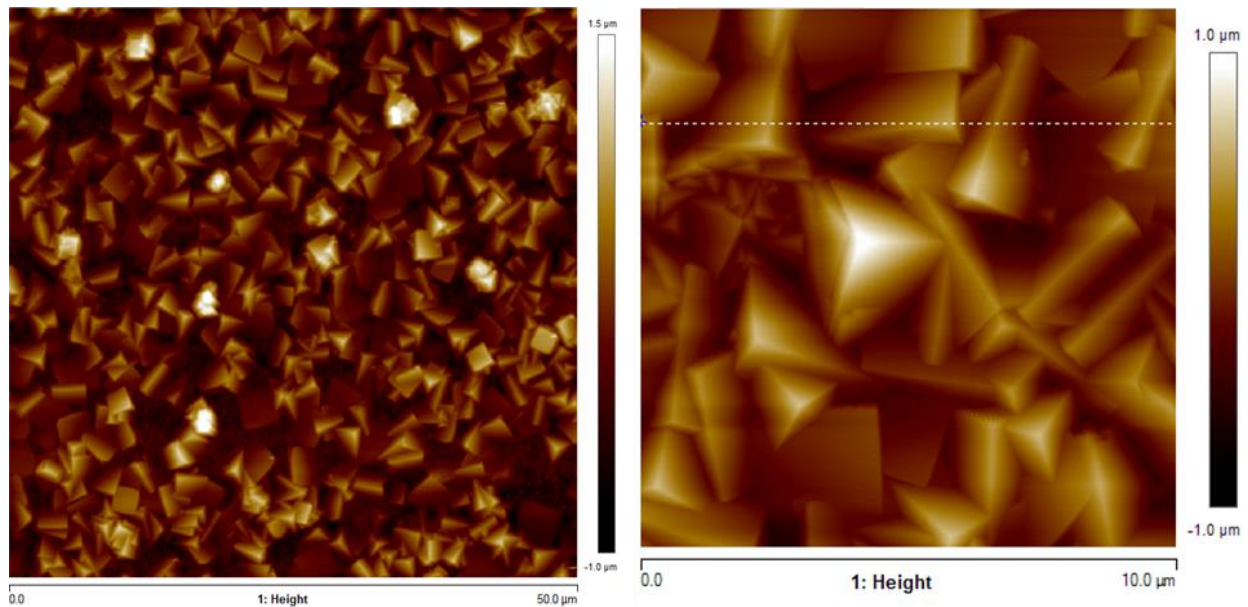


Figure 28 AFM picture of electrodeposited Cu₂O on a IMI bottom-electrode

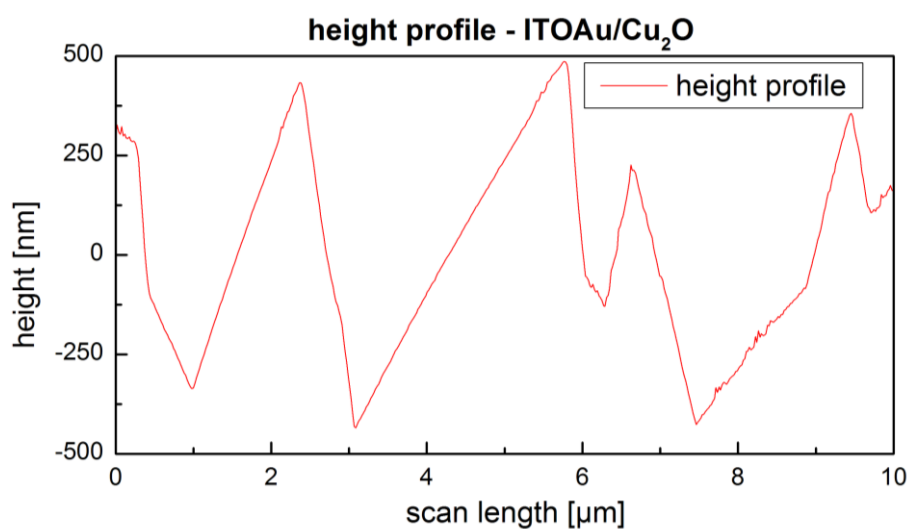


Figure 29 height profile of Cu₂O on IMI electrode - taken from AFM Figure 28 (white line)

The calculated roughness in the IMI case is also very dependent on the applied potential which is why the roughness for two different deposition potentials has been calculated. The results are listed in Table 6.

Table 6 surface roughness comparison - IMI electrode

<i>electrode</i>	deposition potential	surface roughness R_{RMS}
<i>ITO/Au/ITO</i>	- 0,55 V	$(335 \pm 6) \text{ nm}$
<i>ITO/Au/ITO</i>	- 0,58 V	$(338 \pm 12) \text{ nm}$

4.3.5 Summary of the Cu_2O structure on different bottom electrodes

A clear difference in the roughness and grain size can be seen when comparing cuprous oxide deposited on an Au electrode or IMI electrode. The average surface roughness of the IMI/ Cu_2O and Au/ Cu_2O structure has been calculated and added in Table 7.

Table 7 calculated average surface roughness

layout	Average surface roughness R_{Ms}
IMI/ Cu_2O	337 nm
Au/ Cu_2O	157 nm

For visual comparison an SEM picture has been added with the same magnification for both cases. The structure on the left side is associated to an Au electrode whereas the right side is based on a IMI electrode. (Figure 30)

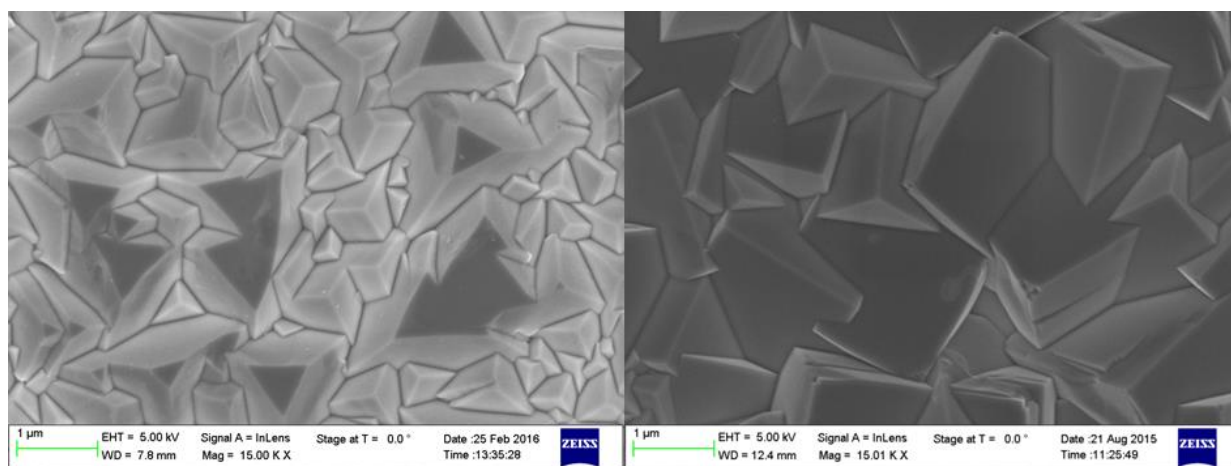


Figure 30 SEM comparison of the grain size dependency of the bottom electrode in electrochemical deposition

It is obvious to see the higher surface roughness of the samples with the IMI bottom electrode. In the Au case the cuprous oxide grows in smaller grains. Therefore, the Au-electrode has been selected to study in more detail and also to use as the bottom electrode for further experiments involving interface engineering that has been monitored by the KPFM. The reason was that it is difficult to deposit very thin layers by spin coating on very rough surfaces.

4.4 Spin coating of organic layers

The SAMs have been prepared with Ethanol in a 1 mg/ ml solution respectively.

The PC₇₁BM has been prepared in a 2 wt.% solution in chlorobenzene.

All Cu₂O-substrates have been annealed for 10 min at 90°C in inert atmosphere (either Ar or N-glovebox) before starting the spin coating process.

200 µl of the SAM solution has been spin coated in a static mode at 3000 rpm for 40s. Afterwards the film was annealed for 2min at 50°C to remove the rest of the ethanol.

For PCBM-deposition, 50µl of the solution were spin coated dynamically at 1000 rpm for 1 min and afterwards the substrates have been annealed for 10 min at 90°C.

Any changes to these procedures are specifically mentioned in the thesis.

4.5 Sputtering of top-electrode

To finish the solar cell structure, a transparent conductive electrode (TCO) has been sputtered on top. As seen in Figure 13 the cell has been illuminated from the top. The selected top electrode has been an 800nm layer of AZO (aluminium zinc oxide). The sputtering parameters are in Table 8

Table 8 top electrode sputtering parameter

	<i>POWER</i>	<i>DEPOSITION RATE</i>	<i>PRE SPUTTERING</i>	<i>PRESSURE</i>	<i>INERT GAS</i>
AZO	120 W	0,667 nm/s	100 s	0,001 mbar	Ar

5 Inorganic-organic hybrid solar cell

In this chapter a Cu₂O/PCBM hybrid solar cell will be manufactured and characterized.

The two architectures presented in Figure 13 have been used to characterize the structure and photovoltaic properties.

5.1 Characterization of solar cell structure

The electrodeposited cuprous oxide has been investigated in chapter 4.3. The electrodeposition has been carried out potentiostatically with an Ag/AgCl reference electrode. (chapter 2.4).

5.1.1 Cu₂O/PCBM structural characterization

This chapter deals with the structural change of the surface after spin coating the PC₇₁BM on the cuprous oxide layer. The change of the interfacial properties will be discussed in the following chapter 6 with the help of the KPFM.

The PC₇₁BM -layer has been prepared by spin coating a 2 wt.% solution by following the recipe in chapter 4.4. Due to the high roughness of the Cu₂O film, the thickness of the PCBM layer could not be verified but it is expected to be in a range of 50 – 80 nm from experiments on perovskite solar cells.^{65,66}

An AFM picture has been performed before and after the deposition of PCBM. The sample was prepared 2,5µm thick with a deposition potential of -0,28V.

In Figure 31 the height map of an 2,5 x 2,5 µm area is shown. The picture on the left relates to the pure Cu₂O -surface. The one on the right shows the exact same spot on the surface area after spin coating PCBM. The smearing of the surface is related to the spin coating of the PCBM layer. The smearing can be seen in more detail in the height profile in Figure 32.

The height profile shows an AFM-scan line which is marked in white dots in the previous AFM picture. It is expected that PCBM will fill the valleys due to the solution processing. This effect can be seen very clear at around 2 µm scan distance where the small peak vanishes after the deposition. It is not entirely clear if the whole indentation is filled by PCBM or perhaps etched by the solvent chlorobenzene.

On nearly horizontal surfaces it is also expected to smooth the peaks and attach to the surface with a different thickness than in the valley.

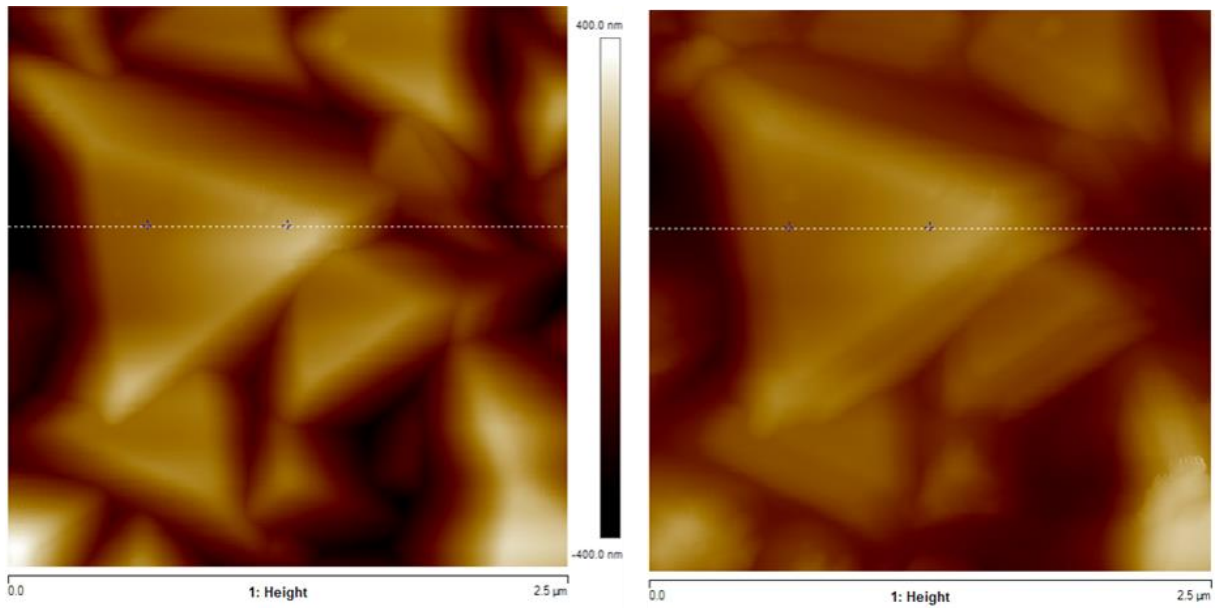


Figure 31 AFM height picture before (left image) and after (right image) the deposition of PCBM

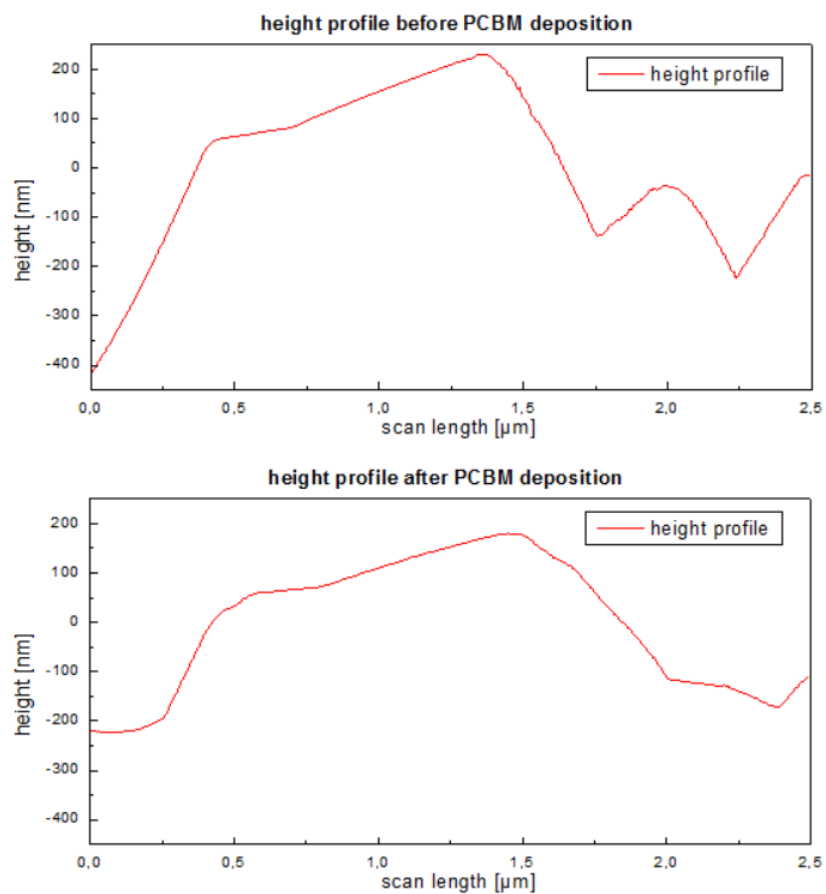


Figure 32 height profile before (top) and after (bottom) depositing PCBM - taken from AFM Figure 31(white line respectively)

The smoothing effect can also be seen when comparing the calculated roughness of a larger scanning area of $40 \times 50 \mu\text{m}$ with the AFM before and after deposition the PCBM. The result has been added in Table 9.

Table 9 surface roughness - comparison before and after depositing PCBM

surface	deposition potential	surface roughness R_q
<i>Au/Cu₂O</i>	- 0,28 V	$(157 \pm 6) \text{ nm}$
<i>Au/Cu₂O/PCB₇₁M</i>	- 0,28 V	$(124 \pm 9) \text{ nm}$

A SEM picture has been taken before and after the deposition of the PCBM. On the left side of Figure 33 the Cu₂O surface can be seen. The bottom electrode has been Au and cuprous oxide was prepared 2,5 μm thick with a deposition potential of -0,28V. The picture on the right shows the same surface after depositing the PCBM. It is worth noting that because the low atomic number of carbon a direct carbon contrast cannot be seen in the SEM.

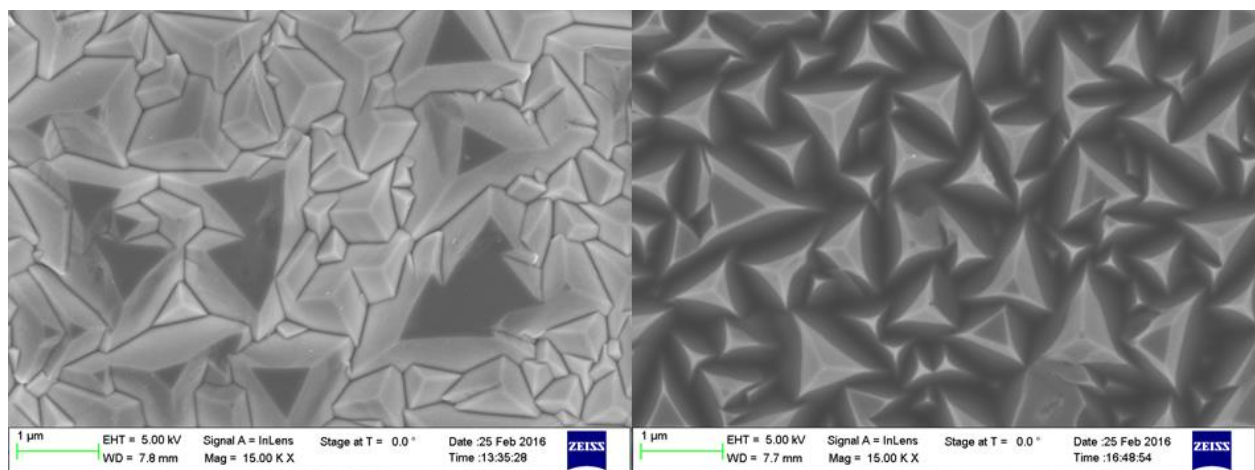


Figure 33 SEM surface picture before and after the spin coating of PCBM

From the measurement results it is clear that the spin coating of the PCBM is successful but the drawback of this method will be evident in the following chapters. Because of the high roughness of the cuprous surface no homogeneous and uniform film formation is expected from the spin coating procedure. This will result in a high shunt resistance of the solar cell.

In case of the ITO – electrode the carrier mobility should be higher because there are less small grains and therefore less grain boundaries to scatter the carriers. But since this structure is rougher than Au one, an even lower homogeneity of the PCBM – film when deposited by spin coating is expected. An alternative approach would be the evaporation of PCBM, which has not been performed in this thesis.

5.2 IV-measurement to characterize the photovoltaic properties of the hybrid solar cell

Up to date there have been no reports published covering the interfacial as well as the photovoltaic properties of a cuprous oxide-PCBM heterojunction solar cell. The only report covering a similar field of study has been from Oku et al.⁶⁷ He investigated the properties of a cuprous oxide and a fullerene derivate (C_{60}) heterojunction solar cell. The reported efficiency for this layout has been $\eta = 4,2 \times 10^{-3}$ for the electrodeposited cuprous oxide and thermally evaporated C_{60} .

The IV-characterization has been carried out in standard measurement conditions with AM 1.5 illumination of 1000 W/m^2 at room temperature. The experimental setup is described in chapter 3.5. The cells were defined by mechanical scribing the top electrode in distinct areas. The areas have been measured after the IV-measurement to calculate the current per square centimeter.

The same layout as in the chapter before has been used. If not mentioned otherwise Au has been used as the bottom electrode and a $2,5 \text{ }\mu\text{m}$ layer of Cu_2O have been electrodeposited on top of it. After the deposition procedure of the PCBM an 800 nm layer of AZO has been sputtered as the top electrode with the deposition parameters listed in Table 8.

As a reference solar cell a 50 nm layer of ZnO has been sputtered up top of the Cu_2O instead of spin coating the PCBM. The ZnO/ Cu_2O interface is well defined and studied in the literature. The photovoltaic parameters are highly dependent on the preparation method. The sputtering parameters for ZnO are listed in Table 10.

Table 10 zinc oxide sputtering parameter

	<i>Power</i>	<i>Deposition rate</i>	<i>Pre sputtering</i>	<i>Pressure</i>	<i>Inert Gas</i>
ZnO	40 W	0,196 nm/s	100 s	0,005 mbar	Ar

Additionally, a second reference has been prepared with sputtering AZO without depositing any n-type layer.

Both references haven been prepared on the IMI/ Cu_2O and the Au/ Cu_2O layout respectively and were then electrically characterized by IV-measurement. The results are added in Table 11 and the plots are illustrated in Figure 34.

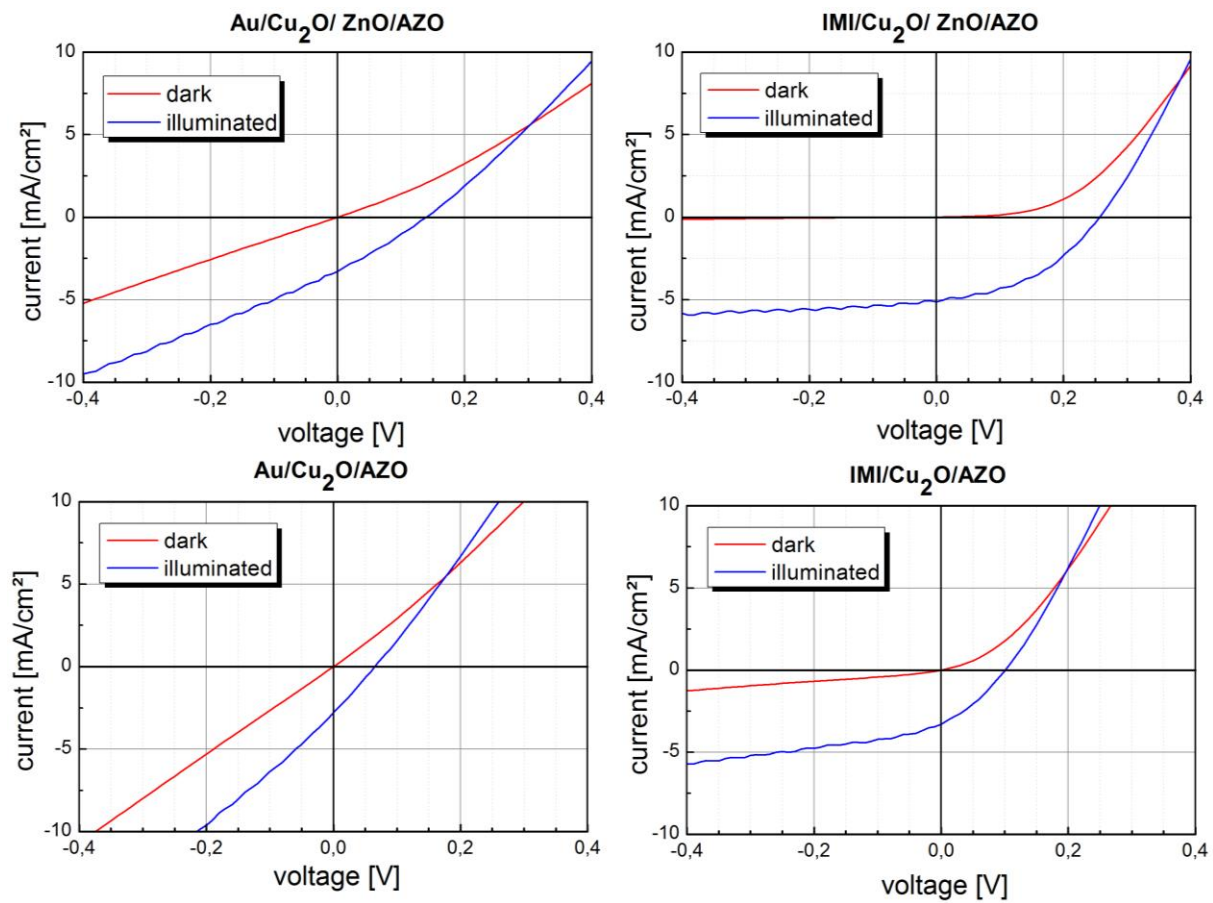


Figure 34 IV- characteristics of reference materials - AZO and ZnO/AZO

Table 11 IV-characteristics for reference solar cell - AZO and ZnO/AZO

<i>process</i>	<i>structure</i>	<i>FF</i> [%]	<i>η</i> [%]	<i>V_{oc}</i> [mV]	<i>J_{sc}</i> [mA/cm ²]
<i>ZnO/AZO sputtering</i>	Au/Cu ₂ O/ZnO/AZO	27,7%	0,127	139,5	-3,29
<i>ZnO/AZO sputtering</i>	IMI/Cu ₂ O/ZnO/AZO	42,4%	0,557	256,7	-5,12
<i>AZO sputtering</i>	Au/Cu ₂ O/AZO	26,3%	0,059	70,3	-3,17
<i>AZO sputtering</i>	IMI/Cu ₂ O/AZO	31,9%	0,106	101,0	-3,30

From the graph it is obvious to see that the best working cell has been produced with the previous discussed ZnO/Cu₂O heterojunction.

AZO or aluminum doped zinc oxide (Al-ZnO) is a highly n-doped ZnO therefore AZO can be treated by definition as a metal and forms a Cu₂O/metal Schottky solar cell. This structure has been studied in literature but is accepted to be not as efficient due to the lack of stability and improvement.²¹

In both different device layouts, the IMI bottom electrode case showed better efficiencies. This had been expected because the grain size is much larger compared to the Au electrode case. This leads to a better charge transport because less scattering on grain boundaries occurs. It can be presumed that the sputtered layer covers the surface with a homogeneous film thickness especially when compared to a deposition via spin coating. For bigger crystals a very homogenous interface is build which is shown the IV-characteristics of the IMI/ $\text{Cu}_2\text{O}/\text{ZnO}/\text{AZO}$ compared to the Au/ $\text{Cu}_2\text{O}/\text{ZnO}/\text{AZO}$. The same is true for the $\text{Cu}_2\text{O}/\text{AZO}$ interface, which can be seen in Figure 35 where a cross-section picture of the structure has been performed.

Additionally, it is worth noting that the current of the illuminated cells is always quite high which could be a result of the high photo-conductivity of the material cuprous oxide. This will be studied in the following measurements as well as the parasitic resistance effects.

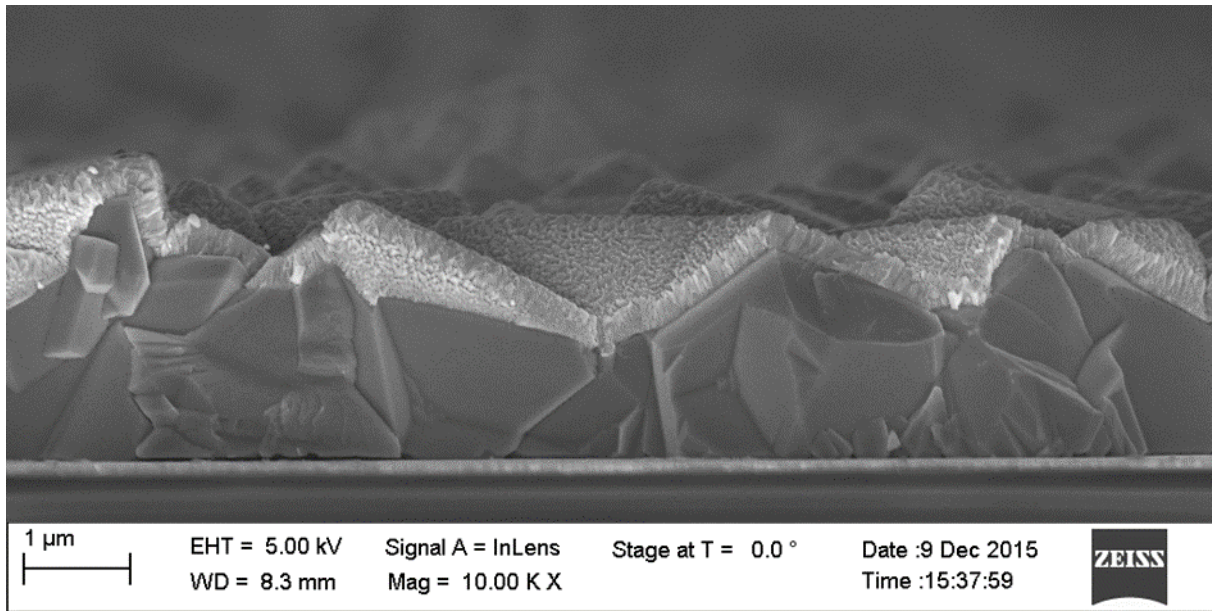


Figure 35 SEM cross-section of IMI/ $\text{Cu}_2\text{O}/\text{AZO}$ structure

After the characterization of the reference solar cell with the $\text{Cu}_2\text{O}/\text{ZnO}$ pn-junction the Au/ $\text{Cu}_2\text{O}/\text{PCBM}/\text{AZO}$ structure has been prepared.

In a first set of experiments the annealing time before depositing PCBM has been varied. The time interval has been chosen to be 10 minutes starting from no annealing to 20 minutes in an inert atmosphere. The aim of this study has been the investigation of performance enhancing effects and the removal of the water film covering the surface since the samples have been stored in a container in air environment. As mentioned in chapter 4.3 the annealing temperature has been chosen to be 90°C . The IV-curves of the corresponding annealing time are illustrated in Figure 36. The photovoltaic parameters have been calculated and are listed in Table 12.

After the deposition of the PCBM the samples have been annealed again for 10 minutes at 90°C. This annealing step has been introduced to enhance the binding and diffusion of the PCBM/Cu₂O interface as well as the removal of the PCBM solvent chlorobenzene.

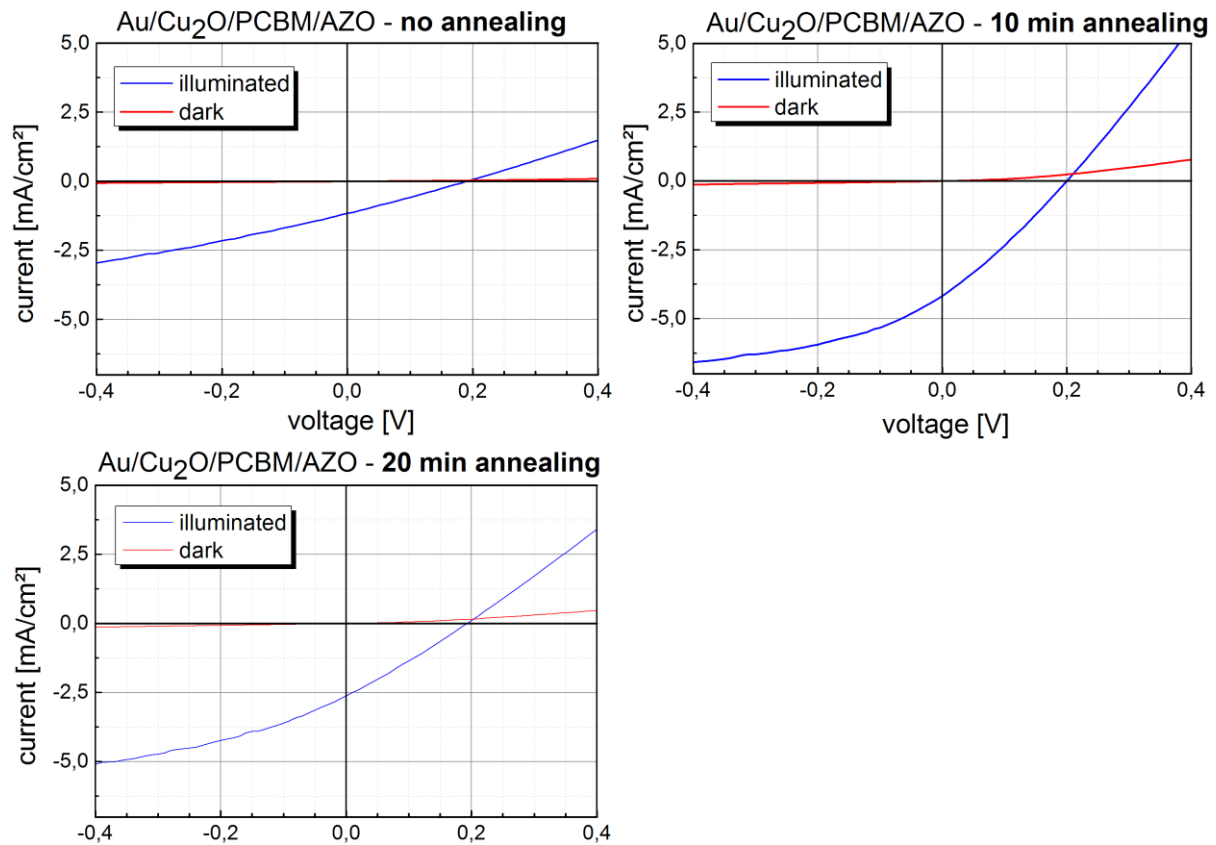


Figure 36 IV- characteristics of Au/Cu₂O/PCBM/AZO heterojunction solar cell - influence of annealing before depositing PCBM

Table 12 IV-characteristics Au/Cu₂O/PCBM/AZO - annealing

<i>process</i>	<i>structure</i>	<i>FF</i>	<i>η</i>	<i>V_{oc}</i>	<i>J_{sc}</i>
		[%]	[%]	[mV]	[mA/cm ²]
<i>no annealing</i>	Au/Cu ₂ O/PC ₇₁ BM/AZO	26,1%	0,058	190,4	-1,16
<i>10 min annealing</i>	Au/Cu ₂ O/PC ₇₁ BM/AZO	28,0%	0,234	200,1	-4,18
<i>20 min annealing</i>	Au/Cu ₂ O/PC ₇₁ BM/AZO	26,7%	0,135	192,7	-2,62

As seen in Table 12 an annealing time of 10 minutes or more has a positive effect on the solar cell characteristics. The obvious reason has been the removal of the water film on the surface. It could also be seen as an activation step after which the PCBM connects better to the surface.

In the experimental studies a change in output characteristics of the solar cell has been seen when illuminating them for a longer period of time. Therefore, the sample which has been annealed for 20 minutes has been selected to study the relation between the illumination time and the output characteristics. The calculated results are illustrated in Figure 37. The time between the measurements has been 10 minutes. It can be seen that with increasing time the open circuit voltage V_{oc} decreases. The overall efficiency increases because the short circuit current increases a higher rate compared to the decreasing voltage.

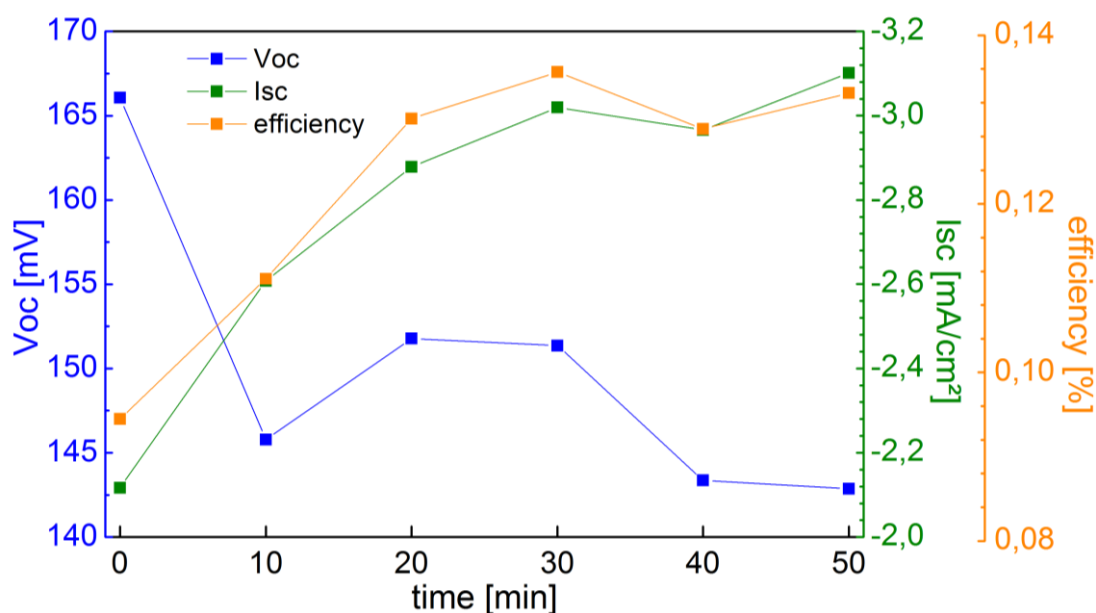


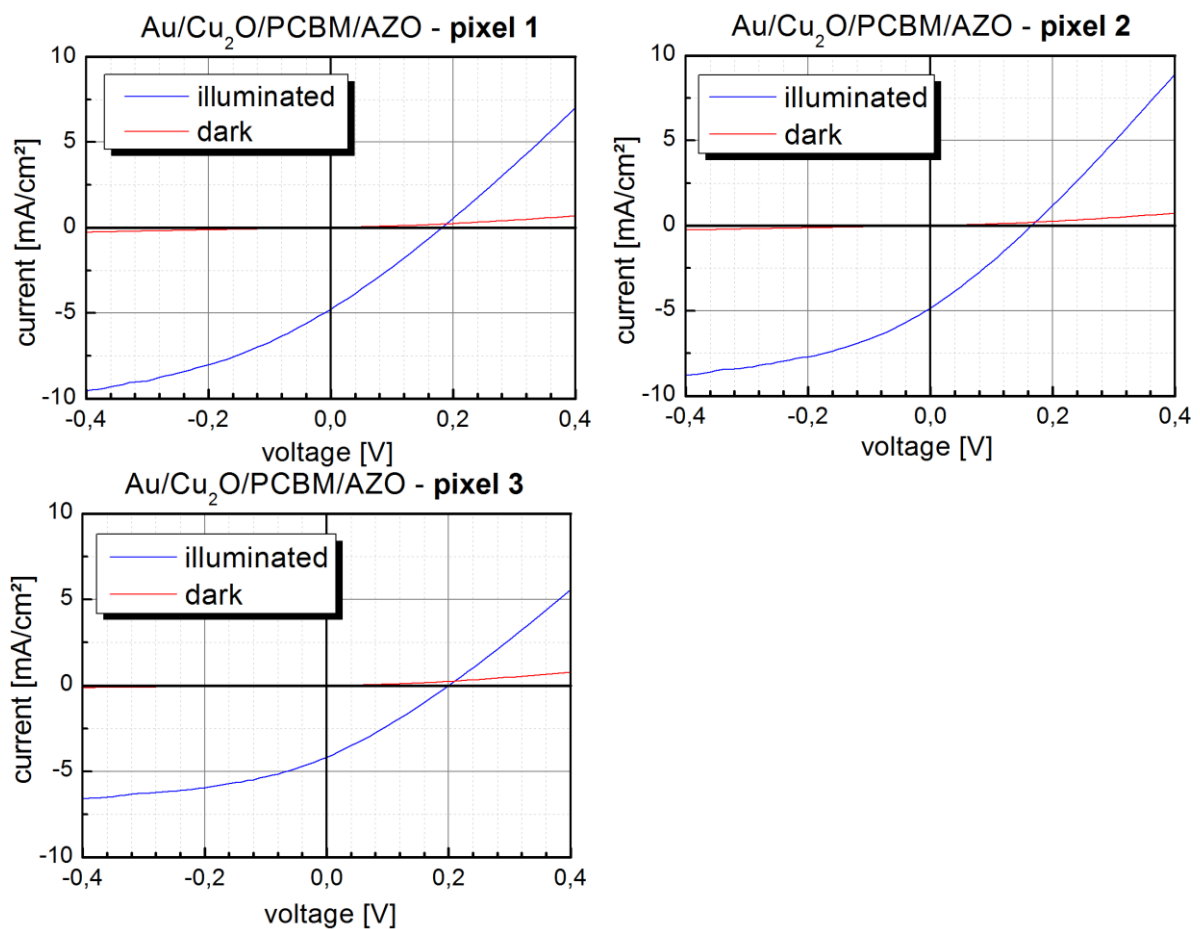
Figure 37 IV- characteristics of Au/Cu₂O/PCBM heterojunction solar cell – illumination time influence on the performance of the solar cell - 10 min illumination between measurements

For the Au/ Cu₂O/PC₇₁BM/AZO structure, the characteristic IV-curves of three pixels have been added in Figure 38 with the photovoltaic properties added in Table 13. The solar cell, which has been annealed for 10 minutes before and after the spin coating of PCBM, has been selected and measured on several pixels.

The V_{oc} of the Cu₂O/PCBM interface ranges in average at around 180 mV.

Table 13 IV-characteristics of Au/Cu₂O/PCBM/AZO - device

<i>name</i>	<i>structure</i>	<i>FF</i> [%]	η [%]	V_{oc} [mV]	J_{sc} [mA/cm ²]
Pixel 1	Au/ Cu ₂ O/ PC ₇₁ BM /AZO	26,7%	0,233	182,3	-4,78
Pixel 2	Au/ Cu ₂ O/ PC ₇₁ BM /AZO	27,3%	0,219	165,7	-4,84
Pixel 3	Au/ Cu ₂ O/ PC ₇₁ BM /AZO	28,0%	0,234	200,1	-4,18
<i>mean value device</i>	-	27,3%	0,229	182,7	-4,60

Figure 38 IV- characteristics of Au/Cu₂O/PCBM/AZO heterojunction solar cell - Performance of several pixels of an exemplary device

An important aspect in the consideration of Figure 38 are the defects. As discussed previously the deposition of PCBM is not homogeneous. Therefore, a high shunt resistance has been expected. This has a big influence on the FF as well as the V_{oc} . The second problem in the examined layout has been

the interfaces. Both interfaces are a possible source for defects and problems. In the semiconductor/organic semiconductor interface ($\text{Cu}_2\text{O}/\text{PCBM}$) the band alignment and the pn-junction plays an important role. No homogenous junction is expected due to the PCBM deposition technique in spin coating. Additionally, the sputtered top electrode AZO hinders the carrier transport because of its low conductivity compared to intrinsic metals and the interface forming with the PCBM.

To verify these assumptions, the series and the shunt resistance have been calculated for pixel 2 of the device shown in Figure 38. The slope around the V_{oc} and I_{sc} has been determined and is illustrated in Figure 39. To compare these resistance values, the same has been done for the reference solar cell with the IMI/ $\text{Cu}_2\text{O}/\text{ZnO}/\text{AZO}$ layout from Figure 34 and has been plotted on the right graph of Figure 39 .

The shunt resistance R_{sh} and the series resistance R_s can be calculated by taking the inverse of the slope. The characteristic resistance R_{ch} can be calculated by taking the inverse slope of the maximum power point. By dividing both resistance by the characteristic resistance the normalized shunt resistance r_{sh} and normalized series resistance r_s can be calculated and compared.

All these values have been calculated from Figure 39 and added in Table 14.

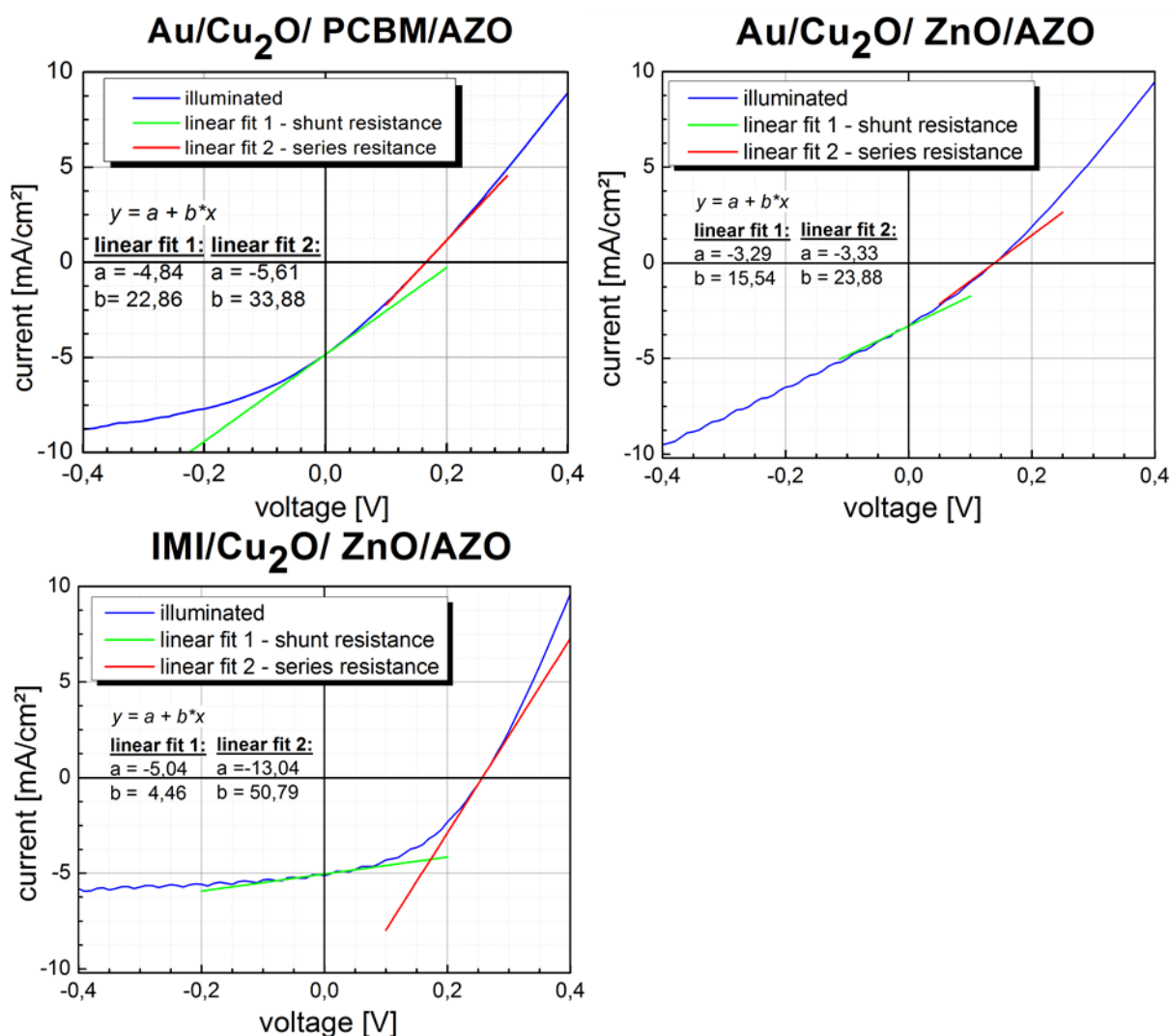


Figure 39 effect of parasitic resistance - shunt resistance and series resistance of Au/Cu₂O/PCBM structure, Au/Cu₂O/ZnO structure and IMI/Cu₂O/ZnO structure

Table 14 calculated values for the parasitic resistance of the Cu₂O/PCBM and the Cu₂O/ZnO interface structure

<i>Au/Cu₂O/PCBM/AZO</i>		<i>Au/Cu₂O/ZnO/AZO</i>		<i>IMI/Cu₂O/ZnO/AZO</i>	
R_{ch}	37,0 Ωcm^2	R_{ch}	50,3 Ωcm^2	R_{ch}	45,9 Ωcm^2
R_{sh}	43,7 Ωcm^2	R_{sh}	64,4 Ωcm^2	R_{sh}	224,4 Ωcm^2
R_s	29,5 Ωcm^2	R_s	41,9 Ωcm^2	R_s	19,7 Ωcm^2
r_s	0,80	r_s	0,83	r_s	0,43
r_{sh}	1,18	r_{sh}	1,28	r_{sh}	4,89

As discussed in chapter 2.2.3 the shunt resistance R_{sh} should go against infinity ($R_{sh} \rightarrow \infty$) whereas the series resistance R_s should go against zero ($R_s \rightarrow 0$). This trend can be best seen in the IMI/Cu₂O/ZnO reference cell which showed the best photovoltaic characteristics.

The same trend can be seen by looking upon the normalized values of the resistance.

The r_{sh} as well as the r_s value are far from the norm for the Au/Cu₂O/PCBM heterojunction cell which has been expected by reviewing the IV-characteristics. Therefore, no well-defined square for the Fill-Factor can be drawn resulting in a very low FF for the Au/Cu₂O/PCBM structure.

From the calculated resistance values the Au/Cu₂O/ZnO showed similar values compared to the Au/Cu₂O/PCBM. Nevertheless, the Au/Cu₂O/PCBM showed better IV-characteristics compared to the Au/Cu₂O/ZnO.

Comparing these results to the IMI/Cu₂O/ZnO interface one can see a better trend like predicted above even though the manufactured interface has not been optimized and is therefore far from ideal.

The current in all solar cells with the cuprous oxide absorber has been very high compared to the literature. The reason could be on one hand the very high parasitic resistance effects which are associated by a bypassing of the current. Another possibility would be the very high photocurrent of the cuprous oxide. This behavior can be seen in Figure 40 which illustrates a different range of pixel 2 from Figure 38. This time the plot focus has been on the forward bias area to show the explicit difference between the illuminated and the dark current. This difference originates from the very high photoconductivity of the cuprous oxide coupled the low shunt resistance due to the inhomogeneous junction and defects.

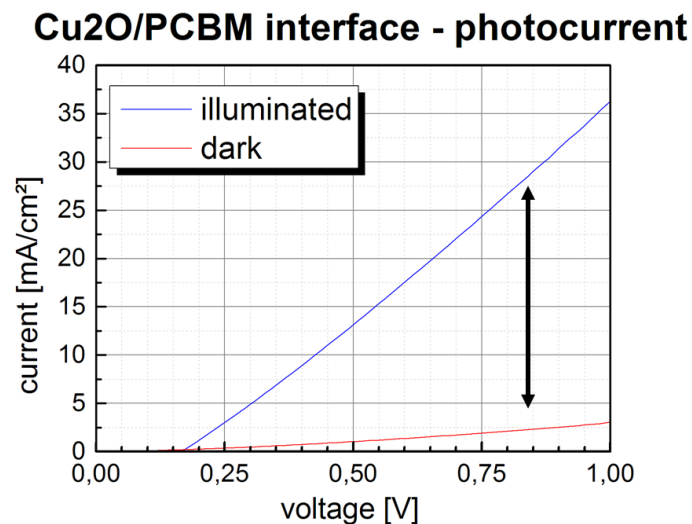


Figure 40 IV - characteristics Cu₂O/PCBM interface – photocurrent

In an last experiment the solar cell layout with the IMI – bottom electrode has been prepared. The thickness of the Cu₂O was 2,5 μm. Before and after the spin coating the PCBM layer an annealing time of 10 min in inert atmosphere was chosen. The top electrode has been again a 800 nm layer of AZO.

The IV-curve for this layout has been added in Figure 41 and the calculated photovoltaic properties can be found in Table 15.

Table 15 IV-characteristics of IMI/Cu₂O/PCBM - device

<i>name</i>	<i>structure</i>	<i>FF</i> [%]	<i>η</i> [%]	<i>V_{oc}</i> [mV]	<i>J_{sc}</i> [mA/cm ²]
<i>Pixel 1</i>	IMI/ Cu ₂ O/ PC ₇₁ BM /AZO	26,3%	0,127	174,2	-2,76
<i>Pixel 2</i>	IMI/ Cu ₂ O/ PC ₇₁ BM /AZO	26,9%	0,098	170,3	-2,13
<i>Pixel 3</i>	IMI/ Cu ₂ O/ PC ₇₁ BM /AZO	26,4%	0,099	173,1	-2,16
<i>mean value device</i>	-	26,5%	0,108	172,5	-2,35

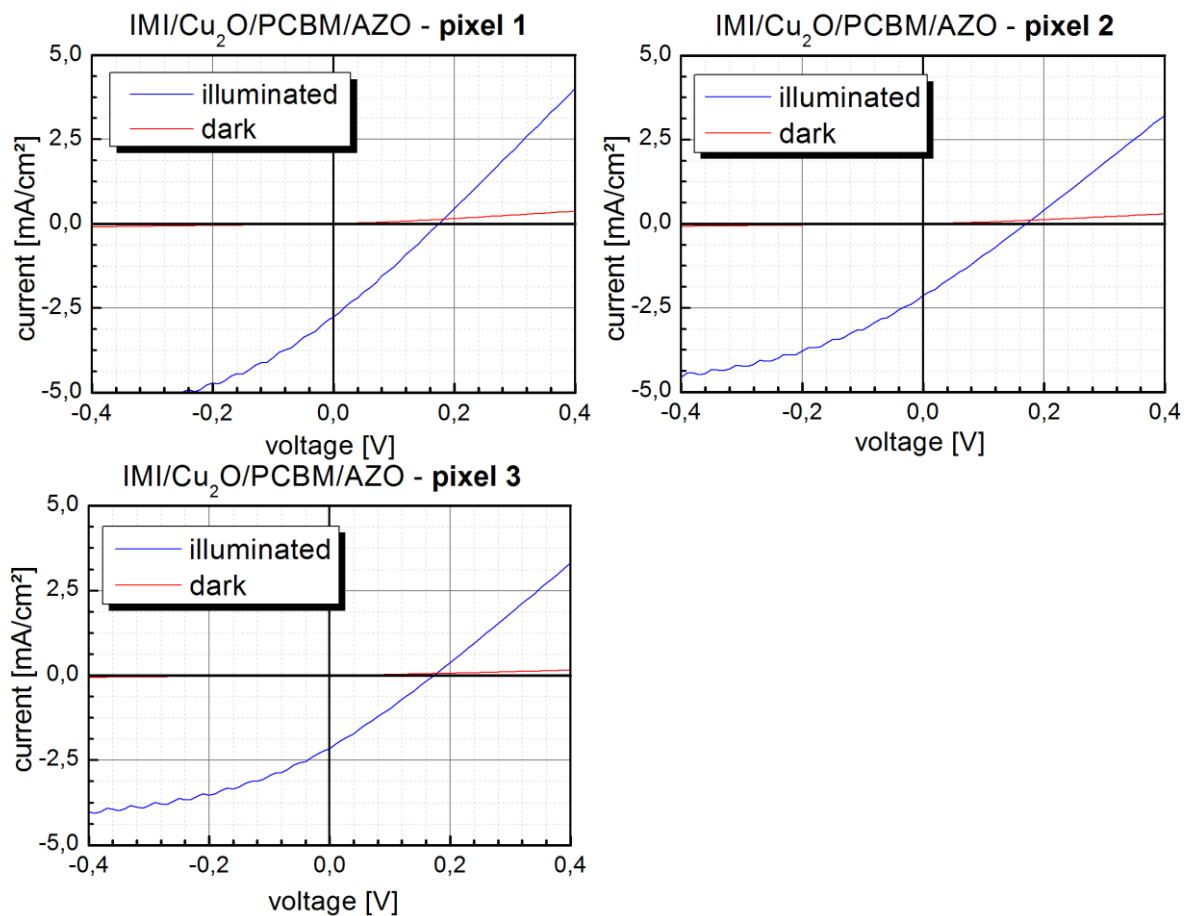


Figure 41 IV- characteristics of ITO/Cu₂O/PCBM heterojunction solar cell - Performance of several pixels of an exemplary device

For the IMI – bottom electrode it is uncertain if the solar cell has really been a result of the cuprous oxide/organic semiconductor interface. Comparing it to the results for the reference materials shows similarities in the output characteristics to the cell with the IMI/Cu₂O/AZO interface.

Generally speaking it is possible to state that the IMI/Cu₂O/ZnO has better PV-characteristics compared to the Au/Cu₂O/ZnO. With the PCBM, opposite PV-characteristics have been measured (Au/Cu₂O/PCBM > IMI/Cu₂O/PCBM).

An explanation would be the high surface roughness of the cuprous oxide when deposited upon the IMI – bottom electrode. Coupled with spin coating as the deposition technique for the PCBM, it is expected that the formation of a homogeneous junction will be lower compared to the Au – bottom electrode case. A change to a more homogeneous deposition technique for the organic layer would be advisable.

5.3 Conclusion of Cu₂O/PCBM heterojunction

In this chapter the cuprous oxide/PCBM heterojunction has been developed and characterized.

In the first part the structural changes of the surface have been monitored. AFM-height profiles and SEM pictures have been taken to analyse the changes. A surface smoothing due to the spin coating of the organic layer could be seen but since the surface of Cu₂O is very rough no homogenous film formation took place.

The PV-characteristics of the hybrid solar cell has been the focus of the second part of this chapter. For the Au/Cu₂O/PCBM/AZO solar cell structure a working cell has been produced with the average characteristics listed in Table 16.

Table 16 average output characteristics of Au/Cu₂O/PCBM/AZO-hybrid solar cell

FF [%]	η [%]	V _{oc} [mV]	J _{sc} [mA/cm ²]
27,3%	0,229	182,7	-4,60

From the values the low fill-factor is noticeable. The reason for this is the high shunt resistance of the solar cell because of the inhomogeneous junction formed. Additionally, the high series resistance shows some problems in the layout and carrier transport properties. The influence of the high photoconductivity of cuprous oxide has also been studied.

The Au bottom electrode has been selected because the interface engineering in the following chapter requires a lower roughness surface. The grain size and the roughness of the cuprous oxide grown on the IMI-bottom electrode has been bigger which is why the main attention has been focused on the layout with the Au bottom electrode.

6 Interface modification using SAMs

6.1 Interfacial structure

The understanding of the interfacial structure formed by the two materials is crucial when designing electronic devices. A lot of work has been done in the field of interfacial energy level alignment and the electronic structure designing especially involving organic materials. An excellent review has been published by Ishii et al.⁶⁸ who discusses the basic concept of energy level alignment and electronic structure of organic/organic and organic/metallic interfaces. A second review by Braun et al.⁶⁹ covers more recent developments of these interfaces.

The interface formed between the inorganic p-type semiconductor Cu_2O and the n-type organic semiconductor PCBM has been investigated in chapter 5. Comparing the results of this structure to high performing pn-junction solar cells (for example single crystal silicon) various performance reducing effects has been identified.

Since the interface between semiconductors is the active region, modification of this regime has the potential to improve and influence several important characteristics for example the electronic properties. The electronic properties can be best studied by looking at the energy levels of the semiconducting materials. Especially in inorganic/ organic heterojunction interfaces the energy level alignment plays a fundamental role for the key properties like the open-circuit voltage.⁷⁰⁻⁷²

As explained in the introduction, the difference in the Fermi-level of the two differently doped semiconductors gives rise upon contact to a built-in voltage. A very important aspect to consider is the interface between these two materials. Due to the heterogeneous structure a lot of localized surface states will be formed which influence the electronic properties. The band diagram is therefore only a starting point in characterizing the interface between two materials.

As a side note it has to be added that organic semiconductors do not form a conventional band structure. This has to be taken into account because of the different transport mechanism and properties. A short review to these properties have been given in chapter 2.3.

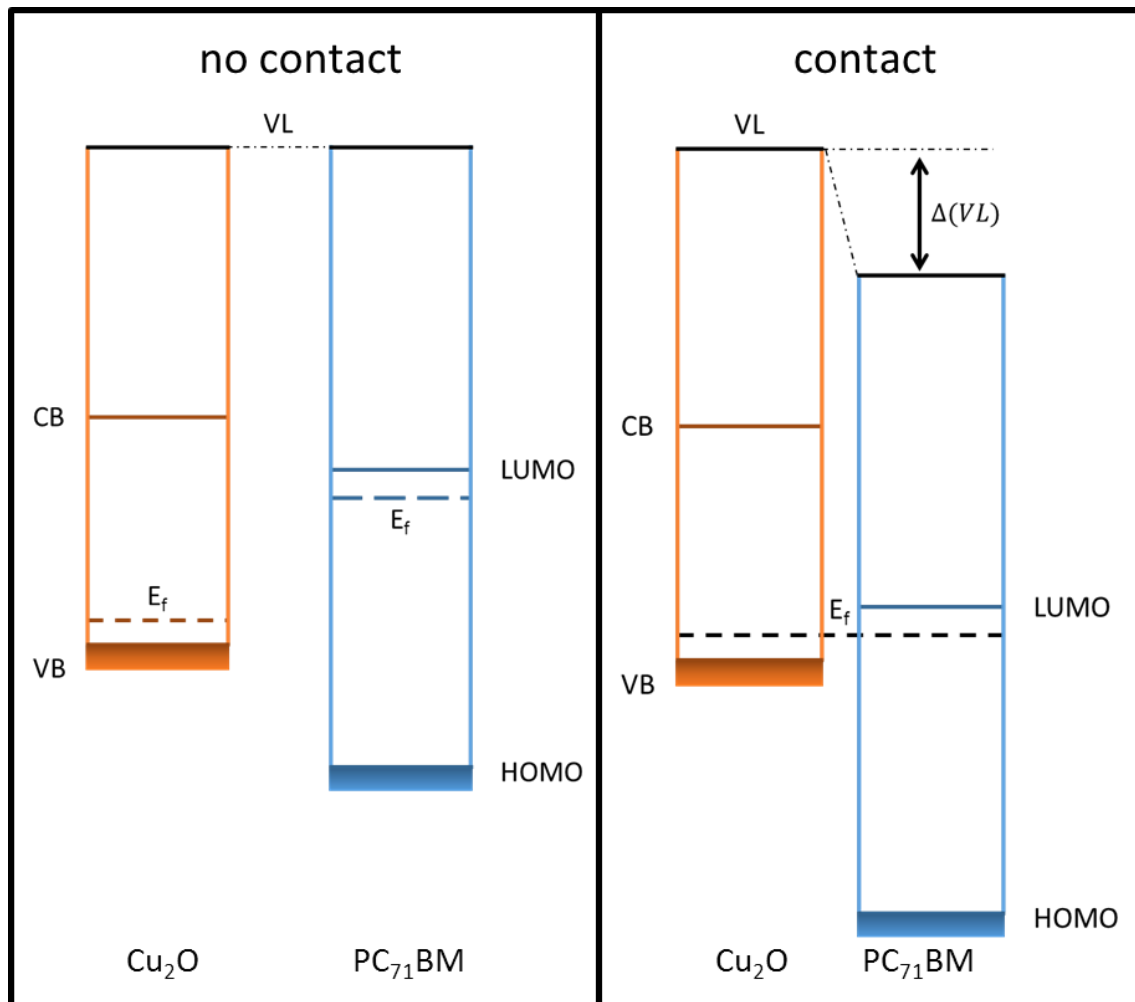
In the following Table 17 the energy levels have been reviewed from literature and from this data a band diagram has been drawn in Figure 42.

On the left side of the figure, the band diagram has been drawn for each material independently which can be identified by the sharing of the same vacuum level (VL). Upon contact the fermi level alignment shifts the vacuum level which can be seen on the right picture. The reason for this shift is the charge carrier exchange described in chapter 2.1.

Table 17 band diagram - literature data of cuprous oxide and PCBM

	Cu₂O		PC₇₁BM
CB	-3,2 eV [1]	LUMO	-3,9 eV [2], 4,0 eV [3], - 3,91 eV [4]
VB	-5,2 eV [1]	HOMO	-6,1 eV [2], 6,0 eV [3], -5,87 eV [4]
E _f	-5,0 eV [1]	E _f	-4,1 eV [2]
E _g	-2,0 eV [1], -2,17 eV [5]	E _g	-2,0 eV [2][3], 1,96 eV [4]

[1] Gershon et al. (2012)⁶⁴ [2] Yang et al. (2013)⁷³ [3] Liu et al. (2013)⁷⁴ [4] He et al. (2011)⁷⁵ [5] Kramm et al. (2012)⁶³

Figure 42 Band diagram Cu₂O/PCBM

6.1.1 Interfacial modification using SAMs

To tune and/or improve the properties of a heterojunction device, interfacial modification has become an important tool. One can significantly influence electronic properties like charge transfer, recombination and carrier transport.⁷⁶

A possible route to modify the interface is the deposition of self-assembled monolayers (SAMs). The effect of SAMs on the electronic structure has been reported and studied widely throughout different research fields.

Rusu et al.(2006) studied the effects Alkylthiolates on the surface dipole and work function of a Au surface.⁷⁷ More related to this thesis, a publication has been done by Lange et al.(2014) in which the workfunction of ZnO has been tuned over a range of 1,5 eV by using modified phosphonic acid self-assembled monolayers.³⁶

6.2 SAMs characterization

For this work several benzoic acid derivatives have been selected which have been already added in chapter 2.5.2 and Table 1.

Goh et al. (2007) investigated the surface modification of benzoic acids on a TiO₂-surface.³⁵

Benzoic acid SAMs and their influence on the work function have been also studied both theoretically³⁴ as well as experimentally⁴⁰ on zinc oxide surfaces. In both cases a tuning ability as well as an improvement of the efficiency has been verified by selection of sufficient SAMs in a hybrid organic-inorganic photovoltaic solar cell setup.

In a first set of experiments the respective benzoic acid derivative has been spin coated upon an electrodeposited Cu₂O surface. Therefore, a solution of 1 mg SAM per 1 mL ethanol has been prepared for each benzoic acid derivative.

To characterize the SAM-layer the following procedure for depositing the SAMs on the surface has been used:

1. Cleaning the sample-substrate with EtOH.
2. Spin-coating 200µL of self-assembled molecules solution on the Cu₂O surface with 3000 rpm for 40 seconds.
3. Drying step at low temperature (50°C) for 2 minutes.
4. Cleaning step with EtOH to remove not tightly bonded molecules.
5. Drying step at low temperature (50°C) for 2 minutes.

6.2.1 Contact angle measurement

In order to gain a first insight of the sticking of the benzoic acid derivatives, a contact angle measurement with H₂O has been carried out. Depending on the tail group of the derivative the SAM-layer the surface should show hydrophobic or hydrophilic properties. In context of the contact angle measurement this can be associated with hydrophobic-tail group when the wetting contact angle is larger than 90° and hydrophilic when smaller than 90°. ⁷⁸ The measurement results have been added in Table 18. The drop volume has been chosen to be 0,5µL.

Table 18 Contact angle of Cu₂O and Cu₂O with self-assembled molecules

Sample	Contact angle (H ₂ O) [°]
pure Cu ₂ O	102,5 ± 7,0
Cu ₂ O + <i>mba</i>	79.1 ± 6.3
Cu ₂ O + <i>tba</i>	96.5 ± 9.1
Cu ₂ O + <i>meba</i>	49.8 ± 6.4
Cu ₂ O + <i>tfba</i>	98.1 ± 2.7
Cu ₂ O + <i>cba</i>	87.9 ± 4.9

In comparison to the pure Cu₂O one can see a change of the wetting contact angle due to the functional head group of the SAM. Therefore, it can be concluded that the benzoic acid derivatives adhere on the cuprous oxide surface. Nevertheless, a homogeneous coverage cannot be expected due to the roughness of the Cu₂O- surface. (see chapter 4.3)

Literature result show similar contact angles after the deposition of the same SAMs used in this thesis, even though the SAMs has been deposited on ZnO.⁴⁰

6.2.2 AFM and KPFM measurements

For a better insight to the electronic structure of the samples, the KPFM has been used.

The KPFM is a tool used to measure the contact potential difference (CPD) between the tip and the sample surface. A brief review of the working principle can be found in chapter 3.2.

The KPFM used in this experiment is based on a controller implemented within the AFM. The AFM model has been the Dimension V model from Veeco with a Nanoscope V controller.

The KPFM mode used has been AM-KPFM where the AM stands for amplitude modulated. With a selected AC-bias applied, the tip starts vibrating in eigenfrequency. To keep this frequency constant an additional DC-Voltage is applied via a feedback-loop. The eigenfrequency of the Pt – coated tip has been around 75 kHz. The sample has been grounded by using a copper tape.

The mapping of the potential has been carried out in AM-KPFM imaging mode. In this mode the AFM first measures the height profile. The tip than soars to a defined lift height over the surface and starts scanning the previous measured topography. During this scan the cantilever is oscillated in

eigenfrequency (see the eq. 10). To nullify electric forces acting on the tip a V_{DC} -Voltage is applied by a feedback loop opposing these forces (V_{CPD}). By keeping the amplitude of the eigenfrequency constant a potential map can be measured.⁷⁹

The lift height has been chosen to be 200 nm because of the high roughness of the cuprous oxide surface. The measured potential denotes to the applied DC-Voltage V_{DC} .

The experiments were performed in ambient environment at an ISO 14644 certified clean room. Since it is no vacuum chamber it is important to keep in mind external circumstances when analyzing the results. Even though the clean room has been controlled by an air ventilation system the temperature as well as the humidity has been varying. A thin water film on top of the substrate surface is expected.

To limit the influence these external circumstances, the substrates have been prepared and processed on the day of the measurement. To calculate the exact work function, the tip work function should have been calibrated prior and after the measurements. In literature a highly ordered pyrolytic graphite reference (HOPG) with a well-defined work function has mostly been used for this purpose.^{76,80} In this work no reference has been used which is why no absolute value of sample work function could be calculated.

Due to the high surface roughness of electrodeposited cuprous oxide coupled with the external effects discussed above an offset KPFM – image for each cuprous oxide sample has been performed. The exact area of this image has been defined by a coordinate system of the AFM. After further processing (deposition of SAMs) the same area has been measured again to compare it with the previous image.

As mentioned above the KPFM also maps the height profile of the surface. The surface roughness R_{RMS} has been calculated before and after the deposition of the SAMs with the tool gwyddion⁸¹. Since the aim of this procedure is the deposition a monolayer it is not expected to see any changes in the roughness. The results have been added in Table 19. All substrates have been prepared by electrochemical deposition (see previous chapter 4.3) on an Au bottom electrode. The thickness of all samples have been chosen to be 2,5 μm with the same deposition potential for all prepared substrates.

As a result of the high roughness and due to the fact that SAMs should form a monolayer it is not possible to detect SAM directly from a height profile. There is a trend to a smoother surface after the deposition which could be related to the smoothing effect upon the deposition of PCBM (see 5.1.1) but since the statistical error is mostly higher than the height differences no real conclusion can be drawn.

Table 19 average surface roughness of Cu₂O before and after the deposition of a SAM- monolayer

Layout	Average surface roughness R_{RMS}	Layout	Average surface roughness R_{RMS}
Cu₂O	$(86 \pm 4) \text{ nm}$	Cu₂O/cba	$(82 \pm 5) \text{ nm}$
Cu₂O	$(80 \pm 5) \text{ nm}$	Cu₂O/tfba	$(80 \pm 5) \text{ nm}$
Cu₂O	$(138 \pm 8) \text{ nm}$	Cu₂O/meba	$(130 \pm 8) \text{ nm}$
Cu₂O	$(85 \pm 4) \text{ nm}$	Cu₂O/tba	$(86 \pm 4) \text{ nm}$
Cu₂O	$(78 \pm 4) \text{ nm}$	Cu₂O/mba	$(76 \pm 5) \text{ nm}$

After measuring the topography, the potential has been imaged. The surface has been measured before and after the deposition of the organic layer on the exact same position. Due to short period of time in between the measurements and the same tip used, the environmental conditions were assumed to be constant. The KPFM potential map before and after the deposition of the SAM-layer has been added in Figure 43.

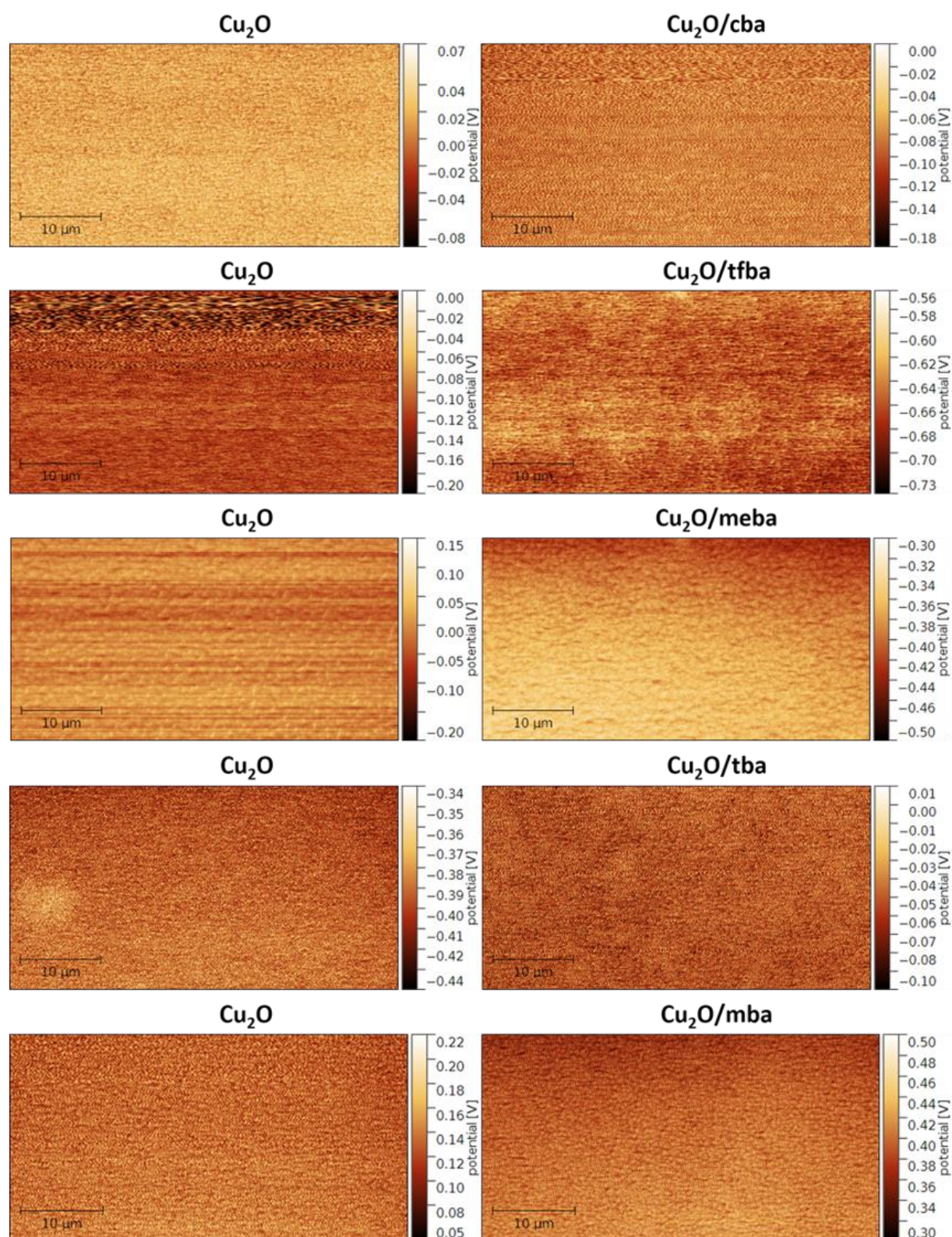


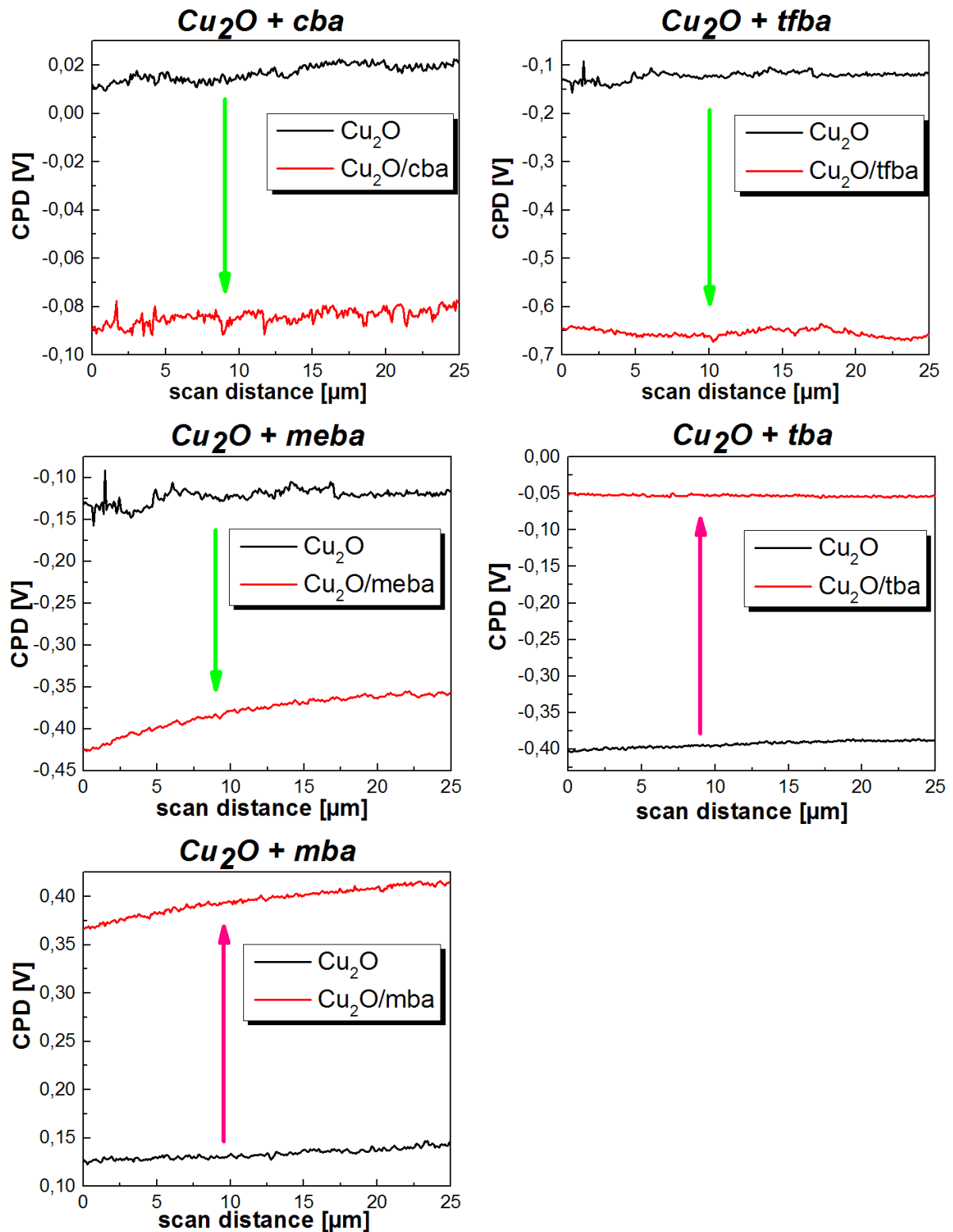
Figure 43 comparison of the potential-map – Cu_2O on the left and the same Cu_2O with deposited SAM on the right

From the potential-map statistical quantities have been calculated with the “Row/Column Statistics Tool” in gwyddion. This tool calculates the average potential of each row and plots them as a function of its position. This row-average as a function of the position has been plotted in Figure 44. The potential difference (shift) between the two measurements because of the SAM deposition has been marked by an arrow for each picture. With the statistics-tool the average CPD-value for each picture respectively has been calculated which has been added in Table 20.

The direct result of the previous discussed conditions can be seen when studying the images and picture average of the pure Cu₂O surface. Depending on the circumstances (humidity, temperature, change of tip) the surface potential of the Cu₂O-surface w shifted to different CPD-values. This is why it was not possible to use one cuprous oxide surface as a reference.

Table 20 average CPD of Cu₂O before and after the deposition of a SAM- monolayer

Layout	CPD (picture -average)	Layout	CPD (picture -average)	ΔCPD
Cu₂O	(16,8 ± 3,3) mV	Cu₂O/cba	(−84,2 ± 3,1) mV	− 101,0 mV
Cu₂O	(−122,2 ± 8,8) mV	Cu₂O/tfba	(−654,4 ± 7,7) mV	− 532,2 mV
Cu₂O	(−7,6 ± 15,3) mV	Cu₂O/meba	(−379,7 ± 20,0) mV	− 379,7 mV
Cu₂O	(−393,3 ± 4,6) mV	Cu₂O/tba	(− 52,9 ± 1,3) mV	+ 340,4 mV
Cu₂O	(133,6 ± 5,1) mV	Cu₂O/mba	(395,9 ± 13,4) mV	+ 262,3 mV

Figure 44 row-average CPD diagram of Cu_2O and $\text{Cu}_2\text{O}/\text{SAM}$ surface

It is important to consider the measured quantity of the potential during the KPFM-experiment. The measured value is the DC-bias necessary to cancel out the electric force acting on the tip. This bias is then recoded as the V_{CPD} . According to eq. 10, the V_{DC} must equal the V_{CPD} since the voltage is applied to the tip.

$$\Delta V = (V_{DC} - V_{CPD}) + V_{AC}\sin(\omega t) \quad \text{eq. 16}$$

To further interpret the results from above it is important to keep in mind the formation of the SAMs. The acid group of the benzoic acid derivate connects with the surface. The parasubstituted head group plays the decisive factor in the change of the surface dipole moment. From the selected five benzoic acid derivates, three have an intrinsic positive dipole moment and two an intrinsic negative one. (see chapter 2.5.2) Only the dipole moment perpendicular to the surface has an influence on the workfunction (eq. 7) which is changing upon contact to the surface.

For a better understanding of the interfacial dipole formed when SAM and surface are brought in contact a schematic illustration has been added in Figure 45. The resulting dipole points out of the surface (Cu_2O) for SAMs with a positive dipole moment (X_{pos}). For SAMs with a negative dipole moment (X_{neg}) the resulting dipole is directed towards the Cu_2O surface. The abbreviation of each derivate is given in the brackets. As template for this figure the publication from Yip et al. (2008) has been used.⁴⁰

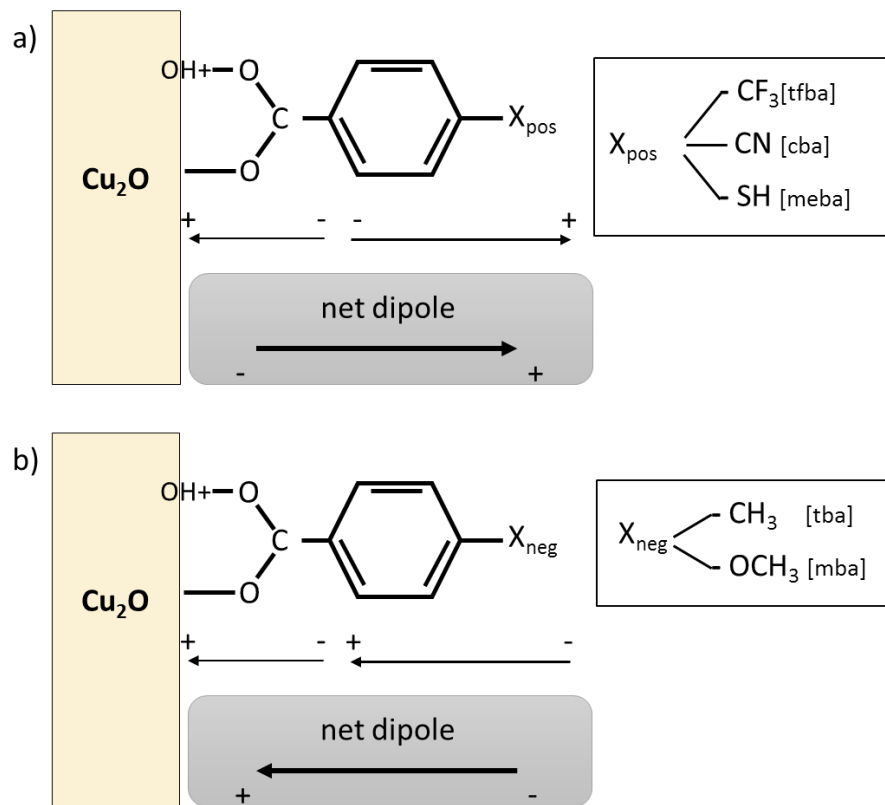
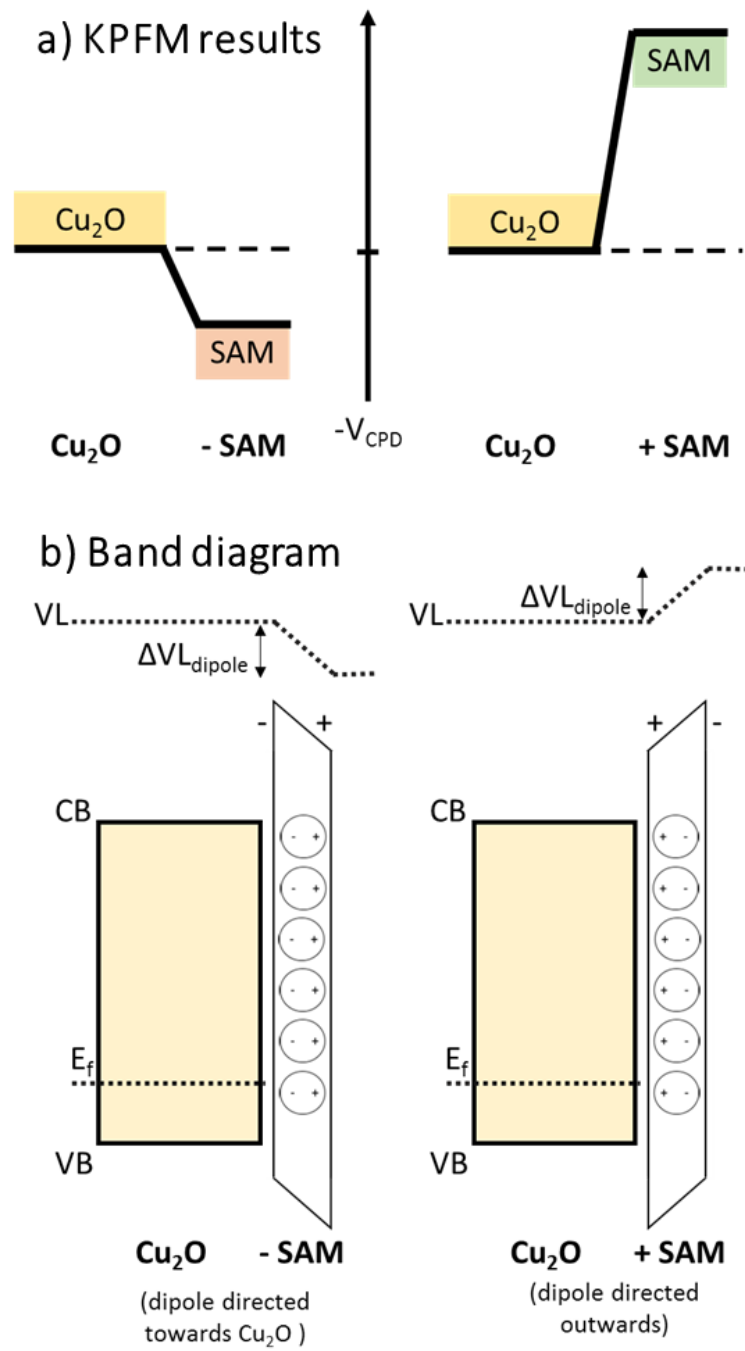


Figure 45 illustration of the net dipole moment formed by depositing a SAM layer – a) SAM with positive intrinsic dipole moment and b) SAM with negative intrinsic dipole moment

Comparing these results with the results obtained from the KPFM-measurements it is obvious to see that the SAMs with the positive dipole moment shift the surface potential in a negative direction with respect to the offset measurement of the respective Cu_2O surface. For SAMs with a negative dipole moment the surface potential shift in a positive direction. Even though the measurements have been carried out in a short period of time, it is not possible to take the potential differences as absolute values since there are too many influencing factors.

Nevertheless, a lot of information can be taken from the direction of the potential shift. The change in the work function is in agreement with the theoretical assessment and also in good accordance to literature.^{36,40,45}

A comparison of the KPFM potential drift (schematic result) and a band diagram of $\text{Cu}_2\text{O}/\text{SAM}$ interface has been drawn in Figure 46. To calculate the energy of the workfunction shift (ΔV_L) one must multiply the potential difference ΔV_{CPD} by the electronic charge $-e$ (see eq. 8). To match the band diagram the KPFM results have been drawn in the negative V_{CPD} direction ($-V_{\text{CPD}}$).

Figure 46 KPFM results and band diagram for $\text{Cu}_2\text{O}/\text{SAM}$ interface

6.3 Cu₂O/PCBM interface characterization with the KPFM

Before modifying the interface with SAMs, the Cu₂O/PCBM interface has been characterized with the KPFM, as mentioned in chapter 5.1.1. The PC₇₁BM-layer has been spin coated following the recipe in chapter 4.4. The sample used to characterize the interface has been prepared with electrochemical deposition on an Au bottom-electrode. The deposition potential has been -0,28 V and the thickness has been approximated to 2,5 μm.

The AFM – height profile of the sample and the change upon deposition of PCBM has been discussed in chapter 5.1.1 The image size has been 40×50 μm.

In the same experiment the potential profile has been mapped with the KPFM. The CPD-map before and after the deposition has been added in Figure 47. In picture c) of the figure the row- average plot has been added after calculating and compiling the data from gwyddion.

The variation of the CPD (picture b) after the deposition of PCBM is also an indication of the inhomogeneous deposition of the organic layer due to the high surface roughness of the cuprous oxide. Another influencing factor could be the contamination of the KPFM – tip with lightly bond organic molecules. To exclude such contamination, the tip should have been calibrated as mentioned above.

As before the average CPD over the whole picture has been calculated by gwyddion and added in Table 21.

A good conformity can be seen by comparing the result with the expected shift ΔV_L of the vacuum level in the band diagram (Figure 42). Since the fermi level of the pure PCBM is higher compared to the pure Cu₂O a shift downwards is expected after the band alignment due to the contact of both materials. This shift corresponds with a CPD shift upwards as has been explained in chapter 6.2.2 since the bias to nullify the electric force is applied to the tip.

Additionally, the electronic properties of p-n junctions have been studied before with the KPFM. Robin et al.(2000) performed a measurement with the KPFM in air in which he showed the CPD- difference between an n and p-type InP-laser diode.⁸² The bias to compensate the electric force has been applied to the tip. The resulting direction of the shift of the CPD-level due to the p-n junction can be compared with the shift measured in this experiment.

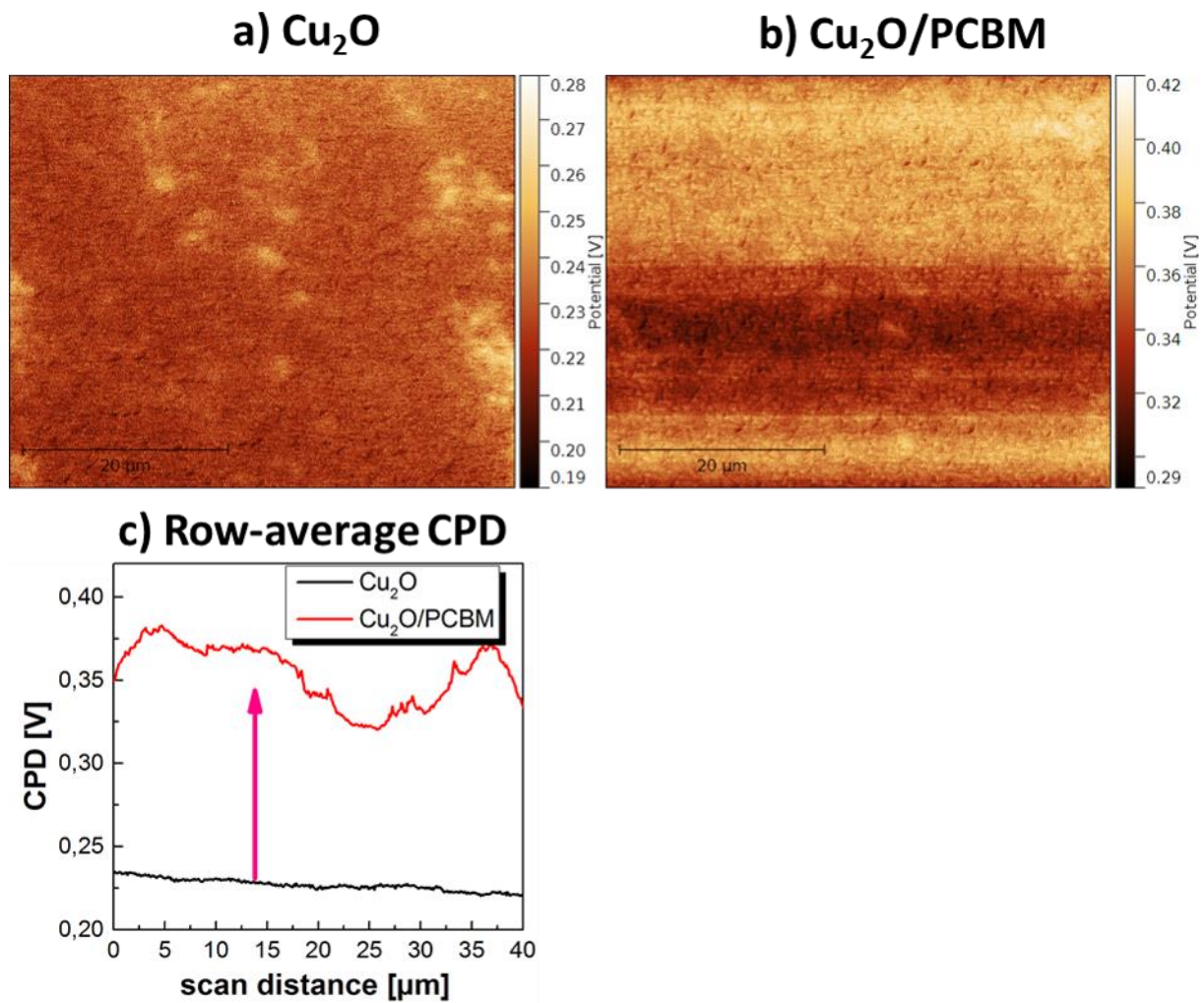


Figure 47 KPFM-images of Cu₂O/PCBM interface: a) Cu₂O image b) image after PCBM deposition c) row-average CPD plot

Table 21 average CPD of Cu₂O before and after the deposition of a PCBM layer

Layout	CPD (picture -average)	Layout	CPD (picture -average)	ΔCPD
Cu ₂ O	$(227,1 \pm 3,7) mV$	Cu ₂ O/PCBM	$(353,9 \pm 18,2) mV$	+ 126,8 mV

The AFM and KPFM image size has been a scan area of 40×50 μm. For a better insight, a more detailed picture of 2,5×2,5 μm has been taken too. The same area has been focused before and after the deposition of PCBM. The images have been added in Figure 48.

The height profile of this figure has been discussed in chapter 5.1.1. The potential profile has been added next to the height profile on the right side. The CPD- difference in this detailed case have been lower compared to the larger scan area.

Both potential profiles have been processed with the “align rows using the median” function in gwyddion to reduce the background.

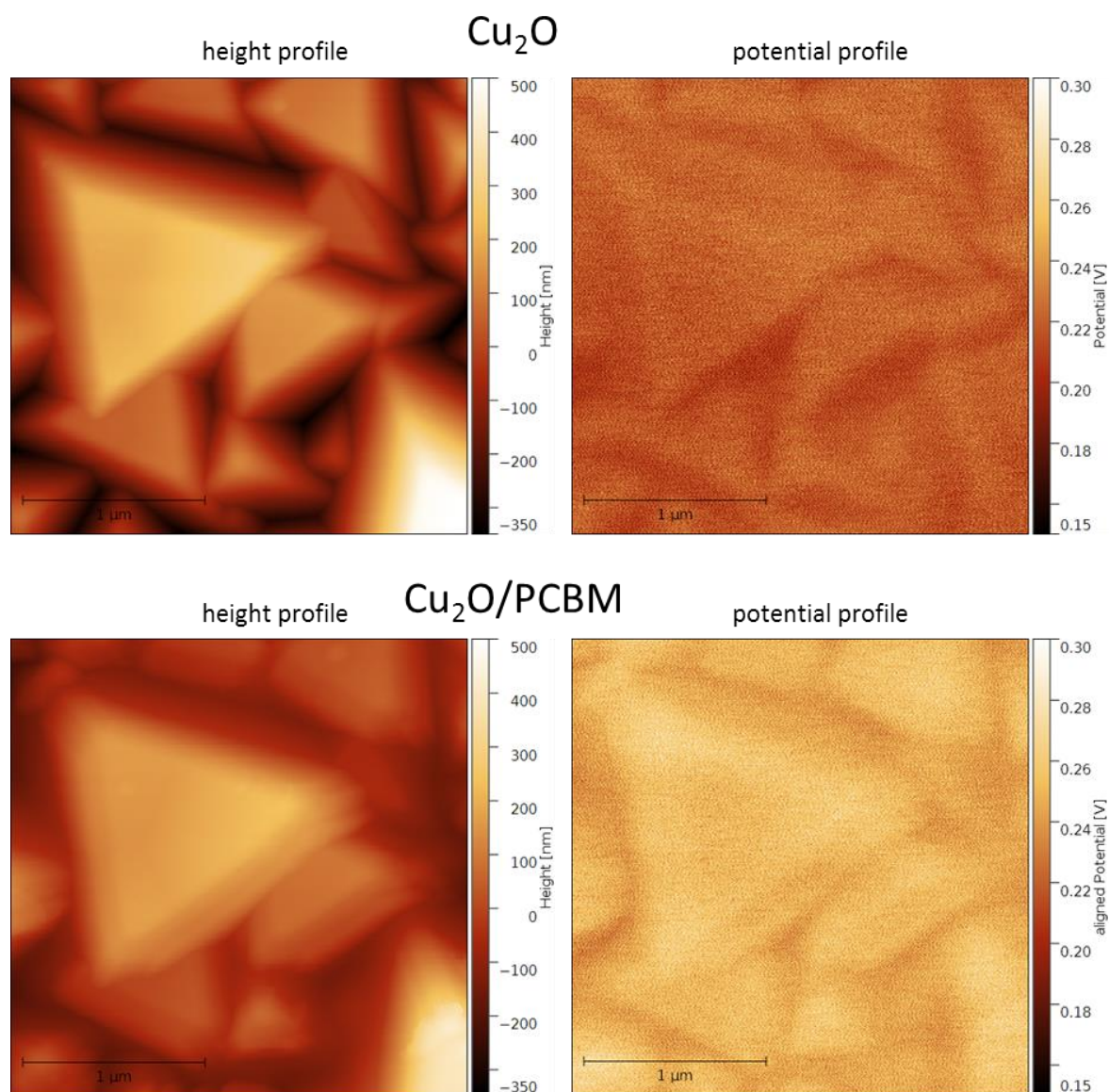


Figure 48 Zoomed-in AFM and KPFM picture of Cu_2O before and after the deposition of PCBM

6.4 Modification of Cu₂O/PCBM interface with selected SAMs

The target of this chapter has been to modify the Cu₂O/PCBM interface, which has been characterized before. The modification has been carried out with the selected self-assembled monolayers.

For this purpose, the two SAMs with the highest change in contact potential difference but opposite directions have been selected.

The SAM used with the positive dipole has been the tfba and the SAM selected with the negative dipole has been the tba. A short review of the properties from previous measurements and literature of these SAMs have been added in Table 22.

Table 22 review of SAMs used for interface modification

Name	Abbreviation	Gas-phase dipole moment	Measured ΔCPD	$\Delta(VL)$
4-(trifluoromethyl) benzoic acid	tfba	+2.1 - +2.7 D	- 532,2 mV	↑
p-Toluic acid	tba	-2.9 - -4.0 D	+ 340,4 mV	↓

The KPFM has been used to measure the change of the surface energy as a result of the deposition of the different thin layers upon the Cu₂O. The change caused by the SAMs and the PCBM individually has been discussed in previous chapters.

For this experiment the same procedure for the SAM deposition as well as the PCBM deposition has been used. The cuprous oxide layer has been prepared 2,5 μm thick on a Au substrate by electrochemical deposition. The deposition potential for all samples in this experiment has been - 0,29 V.

The measured KPFM images have been added in Figure 49. In the first three pictures (1-3), the cuprous oxide surface has been modified with the SAM tfba before depositing the PCBM layer. In picture 4-6 tba has been used as SAM.

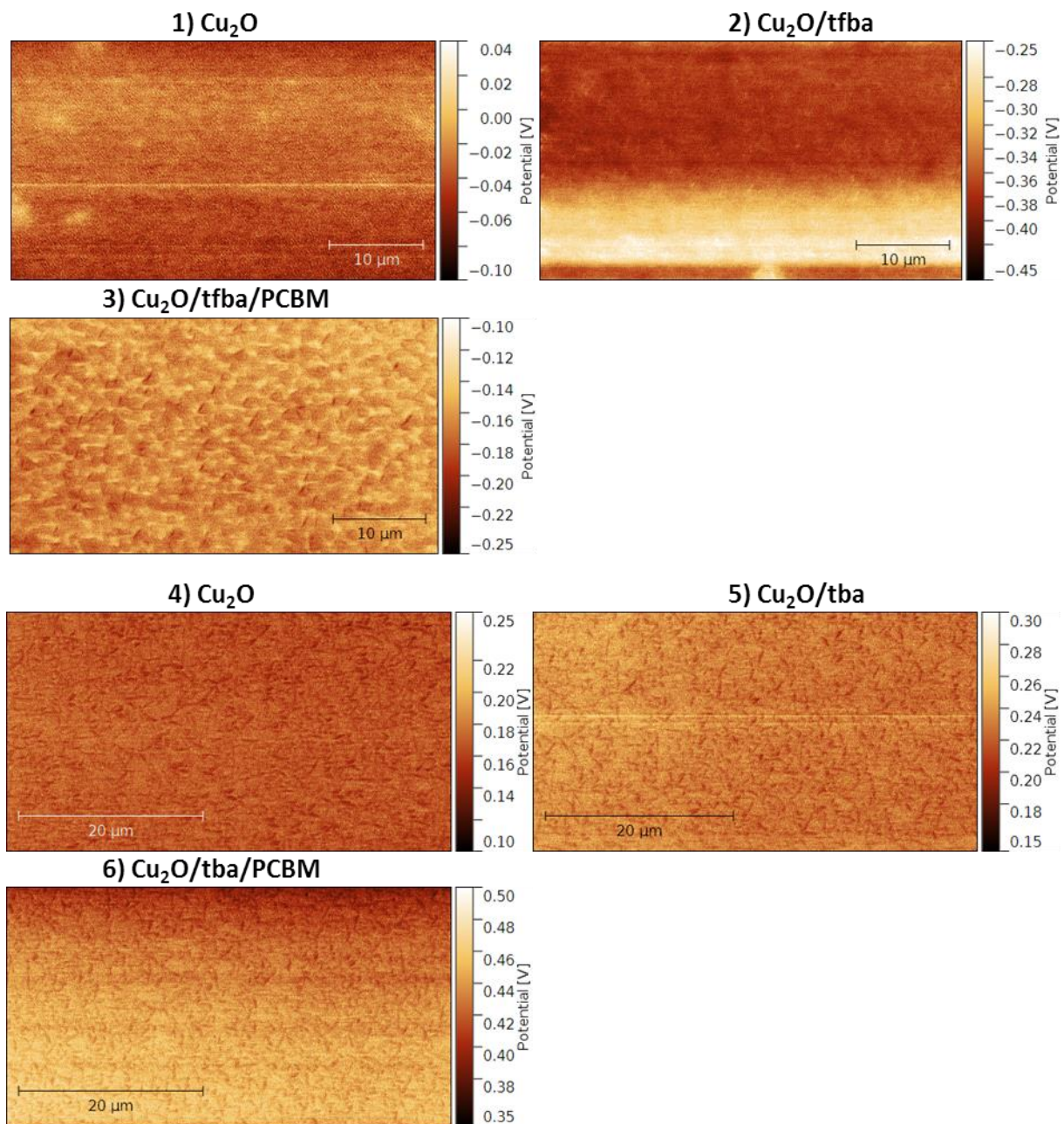


Figure 49 KPFM-images of $\text{Cu}_2\text{O}/\text{SAM}/\text{PCBM}$ interface: 1-3) modification with positive dipole SAM (tfba) 4-6) modification with negative dipole SAM (tba)

The peak in picture 2 could result from some partial charges or problems with the tip since the value jumps back again to the plateau CPD-value. Since the surface is very rough and the measurement is sensitive, distributions of the CPD as well as outliers are expected.

From these KPFM-images the row-average and the picture average CPD value has been calculated using the tool gwyddion. The row-average value has been plotted and added in Figure 50 and the picture-average CPD values have been added in Table 23.

Table 23 average picture CPD of tfba and tba modified structure

Layout	Average CPD [mV]	Layout	Average CPD [mV]
Cu ₂ O	165,9 ± 1,8	Cu ₂ O	-35,5 ± 8,6
Cu ₂ O/tba	229,4 ± 2,8	Cu ₂ O/tfba	-347,1 ± 37,1
Cu ₂ O/tba/PCBM	434,7 ± 16,3	Cu ₂ O/tfba/PCBM	-163,8 ± 3,9

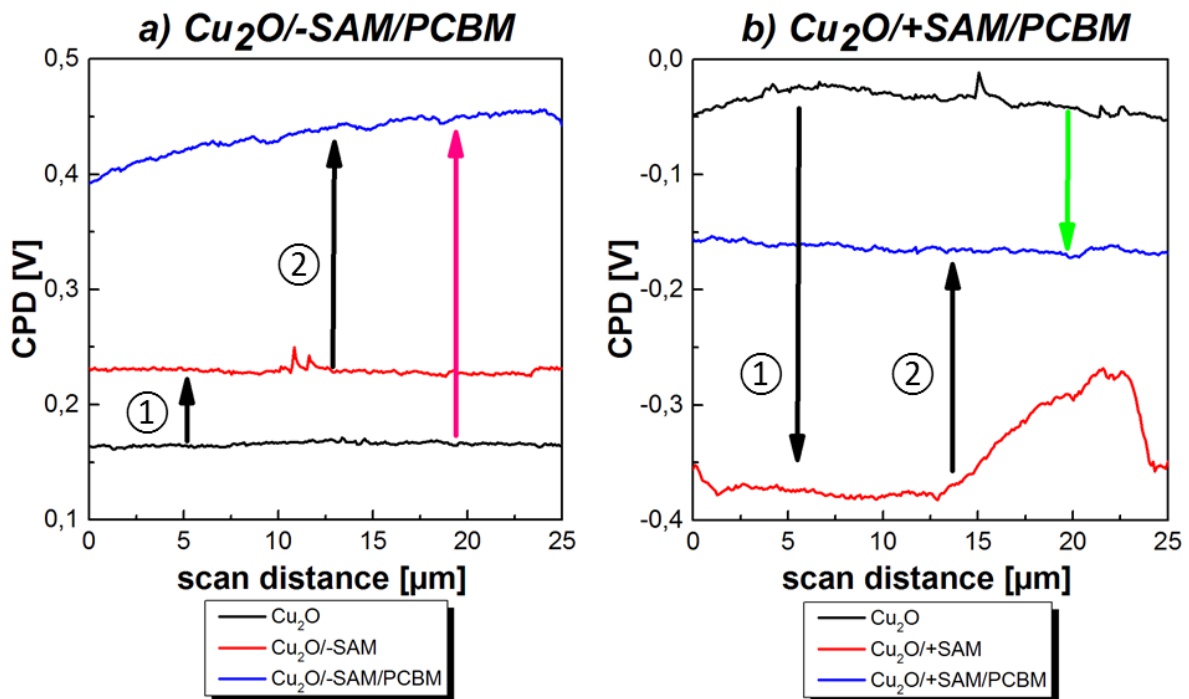


Figure 50 row-average CPD diagram of Cu₂O/SAM/PCBM interface - a) modification with negative dipole SAM (tba) b) modification with positive dipole SAM (tfba)

Referring to the figure it is clear to see the influence of the SAMs on the surface energy.

As measured before the CPD increases after the first deposition of the SAM with the negative dipole moment. This shift has been highlighted with a black arrow and the number 1 (picture a). After deposition of PCBM on top of Cu₂O/SAM the potential increases again (2) resulting in a net increase of the CPD. The overall increase has been marked with a purple arrow and calculated from Table 23 the net increase $\Delta\text{CPD} = 268,8 \text{ mV}$. (potential difference between Cu₂O and the resulting layer).

For the SAM with the positive dipole moment (image b) a behaviour similar to the measurements in the previous chapter can be seen. After the decrease of the potential due to the deposition of the SAM (1) the CPD increases again due to the deposition of PCBM. The result has been an overall decrease of the CPD which has been marked by the green arrow. The calculated net decrease has been $\Delta\text{CPD} = -128,3 \text{ mV}$.

The calculated results as well as the calculated potential difference ΔCPD for the Cu₂O/PCBM case (chapter 6.3) have been added in Table 24.

Table 24 overall change in the Cu₂O/PCBM surface energy due to the introduction of SAMs

Layout	ΔCPD
Cu ₂ O /PCBM	+ 126,8 mV
Cu ₂ O/tba/PCBM	+ 268,8 mV
Cu ₂ O/tfba/PCBM	-128,3 mV

These results show a general possibility to influence the surface potential of the Cu₂O and PCBM interface. With the introduction of a negative SAM the overall CPD increases compared to Cu₂O/PCBM structure whereas the overall CPD decreases when introducing a positive SAM.

This result has been drawn in the inverse direction ($-V_{\text{CPD}}$) in Figure 51 a). A band diagram has been drawn for the structure using the result from the KPFM-experiment and added to the figure (b).

The band diagram has been drawn in the specific case where the band banding has been eliminated by applying an external bias, the so called flat-band voltage. By introducing a negative and positive SAM layer the vacuum-level shifts downwards or upwards respectively. This has been verified in chapter 6.2.

From the theoretical point of view the V_{OC} should increase when adding a layer of SAM with a positive dipole moment and decrease when adding a SAM with a negative dipole moment. Since these results

show good agreement with literature reports^{35,36,40}, an increase or decrease of the open-circuit voltage of the solar cell in the IV-measurement is expected.

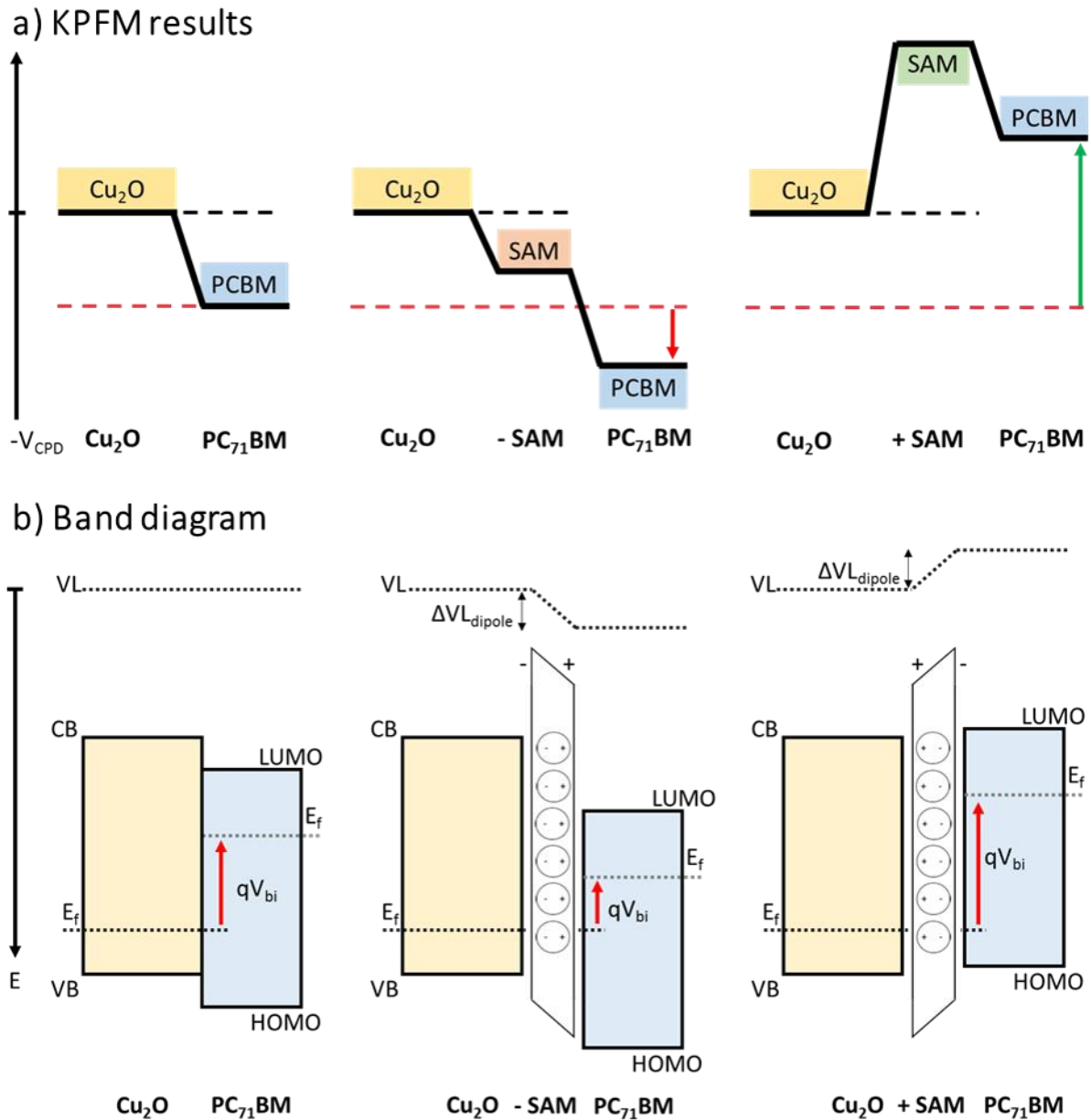


Figure 51 KPFM results and band diagram of $\text{Cu}_2\text{O}/\text{SAM}/\text{PCBM}$ interface

For the IV-characterization a new set of samples have been prepared. As before the Cu_2O have been prepared $2,5\mu\text{m}$ with a deposition potential of $-0,29\text{ V}$ on a Au substrate.

The deposition of the respective SAM-layer and the PCBM layer has been carried out in a nitrogen glovebox with the same preparation procedure as used before.

After processing the organic layers, the substrates have been transported immediately into the sputtering system where they have been left overnight in high vacuum to minimize oxygen inclusions. The sputtered top electrode has been an 800 nm layer of AZO with the same sputtering parameters noted in chapter 4.5.

By just looking at the active interface three different devices have been prepared: a) one with a SAM with positive dipole, b) one with a SAM with the negative dipole and c) one without any SAM as a reference measurement.

The IV- curves of the three devices have been added in Figure 52 with the detailed characteristics written in Table 25.

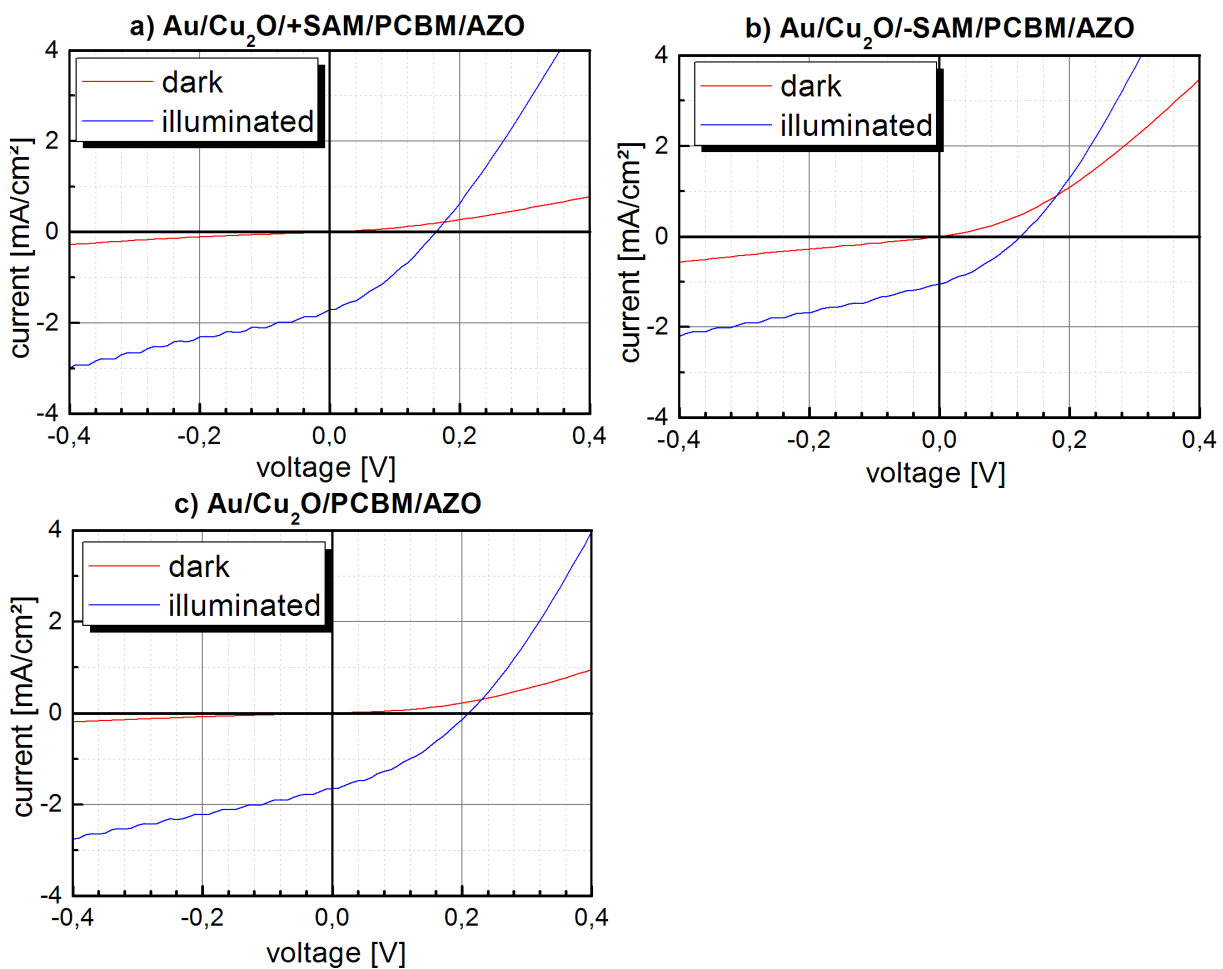


Figure 52 IV – measurement of the SAM modified Au/Cu₂O/PCBM/AZO heterojunction – a) modified with positive dipole SAM b) modified with negative dipole SAM c) reference Cu₂O/PCBM interface

Table 25 characteristics from IV measurement of Cu₂O/PCBM interface modification using SAMs

structure	FF [%]	η [%]	V _{oc} [mV]	J _{sc} [mA/cm ²]
Au/ Cu ₂ O/+SAM/ PC ₇₁ BM /AZO	33,5%	0,094	163,4	-1,71
Au/ Cu ₂ O/-SAM/ PC ₇₁ BM /AZO	31,9%	0,042	124,3	-1,05
Au/ Cu ₂ O /PC ₇₁ BM /AZO	34,9%	0,120	209,3	-1,65

As one can see in the figure and the table, working devices have been constructed. Comparing these results to the previous measured cells (chapter 5.2), the standout parameter is the lower current for this set of samples.

The V_{OC} has been in the same range as measured before for the Cu₂O/PCBM heterojunction. (see chapter 5.2)

Looking at the difference when introducing self-assembled monolayers, a difference between the positive and the negative dipole SAM can be seen.

It is not entirely clear, if this change of the characteristics is entirely induced by the lowering of the workfunction by the SAMs. The detailed interaction between the PCBM and the SAMs and the cuprous oxide and the SAMs would need further studies. Also, effects like recombination of charge carriers by additional induced defect states after deposition the SAM-layer should be considered. Another decisive point in these interfacial studies is the homogeneity of the deposited layers since the electrodeposited cuprous oxide has a relative rough surface structure.

The expected enhancing effect due to the introduction of the SAMs cannot be concluded. A partial control of the electronic properties by SAMs with an opposite dipole moment could be achieved.

To verify these results further measurements with all SAMs should be carried out. Additionally, other self-assembled monolayer groups like thiols or phosphonic acids could be used as has been utilized in various papers.^{36,83–85}

7 Conclusion

Cuprous oxide has been attracted a lot of attention in recent studies as an inorganic absorber. This abundant material offers an affordable large scale production which accomplishes the requirement of cost-per-watt and material supply. N-type doping is difficult for the intrinsic p-type semiconductor Cu_2O which is why the research focuses mainly on a heterojunction structure with Cu_2O as the absorber.

In this thesis the organic n-type semiconductor PCBM has been used to build a heterojunction with Cu_2O . The cuprous oxide has been electrochemically deposited on an Au- and an ITO/Au/ITO-electrode. After spin coating the PCBM a transparent AZO-top electrode has been sputtered. Each layer has been characterized using various techniques such as SEM, AFM and IV-measurements

Since there are no publications on this solar cell structure, each layer has been optimized. The Cu_2O as well as the $\text{Cu}_2\text{O}/\text{PCBM}$ layer has been characterized by using the SEM and the AFM as well as the XRD and FTIR. Since the surface roughness of the Au/ Cu_2O structure has been significantly lower than the ITO/Au/ITO/ Cu_2O -structure the main focus has been directed towards the Au/ Cu_2O structure.

The resulting average PV-characteristics for an Au/ $\text{Cu}_2\text{O}/\text{PCBM}/\text{AZO}$ -solar cell structure has been added in Table 26.

Table 26 IV-characteristics of $\text{Cu}_2\text{O}/\text{PCBM}$ interface

structure	FF [%]	η [%]	V_{oc} [mV]	J_{sc} [mA/cm ²]
Au/ $\text{Cu}_2\text{O}/\text{PC}_{71}\text{BM} / \text{AZO}$	27,3%	0,229	182,7	-4,60

There have been various performance impairing properties identified which decrease the overall performance of the solar cell.

The high surface roughness of the electrodeposited cuprous oxide is problematic for the homogenous deposition of the spin coated the PCBM-film. This results in a very high shunt resistance due to the inhomogeneous junction. Additionally, the high photoconductivity of cuprous oxide, the not ideal carrier transport at the contacts and recombination are also restricting the performance.

To enhance and control the PV-characteristics self- assembled monolayers have been used to engineer the interface of the Au/ $\text{Cu}_2\text{O}/\text{PCBM}$ heterojunction with selected benzoic acid derivates of opposite dipole moment. The work function modulation by SAMs have been reported in several studies and publications.

At first the Au/Cu₂O surface has been treated with SAMs in order to verify a formation of a layer on the surface as well as the influence of the molecule dipole moment on the surface energy. This has been done using the KPFM and the contact angle measurement.

After these experiments the Au/Cu₂O/PCBM interface have been selectively modified by the two SAMs with the highest change in surface potential but opposite directions. The Au/Cu₂O/SAM/PCBM heterojunction has then been studied with the KPFM in order to gain an insight to the change in surface potential by the deposition of the SAMs. From these experiments a shift of the overall potential could be detected which is related to the self-assembled monolayers. This shift in the work function is comparable to the theoretical evaluation as well as literature results.

The measured IV-characteristics of the solar cell structure has been added in Table 27.

Table 27 IV-characteristics of Au/Cu₂O/PCBM interface modification using SAMs

structure	FF [%]	η [%]	V_{oc} [mV]	J_{sc} [mA/cm²]
Au/ Cu ₂ O/+SAM/ PC ₇₁ BM /AZO	33,5%	0,094	163,4	-1,71
Au/ Cu ₂ O/-SAM/ PC ₇₁ BM /AZO	31,9%	0,042	124,3	-1,05
Au/ Cu ₂ O /PC ₇₁ BM /AZO	34,9%	0,120	209,3	-1,65

From the PV-characteristics of the modified structure no performance enhancing effects could be seen but a partial control of the PV-properties could be studied. This behaviour is related to the resulting direction of the SAM dipole moment which also corresponds with the measured KPFM results.

Bibliography

1. Würfel, P. & Würfel, U. *Physics of solar cells: from basic principles to advanced concepts*. (Wiley-VCH, 2009).
2. Solar cell efficiency. *Wikipedia, the free encyclopedia* (2016).
3. Sze, S. M. & Ng, K. K. *Physics of semiconductor devices*. (Wiley-Interscience, 2007).
4. Van Zeghbroeck, B. V. *Principles of semiconductor devices and heterojunctions*. (Prentice Hall ; Pearson Education [distributor], 2010).
5. Shockley, W. The Theory of p-n Junctions in Semiconductors and p-n Junction Transistors. *Bell Syst. Tech. J.* **28**, 435–489 (1949).
6. Solar Spectral Irradiance: Air Mass 1.5. Available at: <http://rredc.nrel.gov/solar/spectra/am1.5/>. (Accessed: 9th June 2016)
7. *Thin-Film Solar Cells*. **13**, (Springer Berlin Heidelberg, 2004).
8. *Thin film solar cells: fabrication, characterization and applications*. (Wiley, 2007).
9. Green, M. A. *Solar cells: operating principles, technology, and system applications*. (Prentice-Hall, 1982).
10. PVEducation. Available at: <http://pveducation.org/>. (Accessed: 22nd July 2016)
11. Köhler, A. & Bässler, H. *Electronic processes in organic semiconductors: an introduction*. (Wiley-VCH, 2015).
12. Stafström, S. Electron localization and the transition from adiabatic to nonadiabatic charge transport in organic conductors. *Chem. Soc. Rev.* **39**, 2484–2499 (2010).
13. *Nanoelectronics and information technology: advanced electronic materials and novel devices*. (Wiley-VCH, 2012).
14. Austria. *Sigma-Aldrich* Available at: <http://www.sigmaaldrich.com/austria.html>. (Accessed: 23rd July 2016)
15. Chatterjee, S., Saha, S. K. & Pal, A. J. Formation of all-oxide solar cells in atmospheric condition based on Cu₂O thin-films grown through SILAR technique. *Sol. Energy Mater. Sol. Cells* **147**, 17–26 (2016).
16. Rühle, S. *et al.* All-Oxide Photovoltaics. *J. Phys. Chem. Lett.* **3**, 3755–3764 (2012).

17. Brattain, W. H. The Copper Oxide Rectifier. *Rev. Mod. Phys.* **23**, 203–212 (1951).
18. Wong, T. K. S., Zhuk, S., Masudy-Panah, S. & Dalapati, G. K. Current Status and Future Prospects of Copper Oxide Heterojunction Solar Cells. *Materials* **9**, 271 (2016).
19. Dimopoulos, T. *et al.* Effect of thermal annealing in vacuum on the photovoltaic properties of electrodeposited Cu₂O-absorber solar cell. *EPJ Photovolt.* **5**, 50301 (2014).
20. Wadia, C., Alivisatos, A. P. & Kammen, D. M. Materials availability expands the opportunity for large-scale photovoltaics deployment. *Environ. Sci. Technol.* **43**, 2072–2077 (2009).
21. Mittiga, A., Salza, E., Sarto, F., Tucci, M. & Vasanthi, R. Heterojunction solar cell with 2% efficiency based on a Cu₂O substrate. *Appl. Phys. Lett.* **88**, 163502 (2006).
22. Malerba, C. *et al.* Absorption coefficient of bulk and thin film Cu₂O. *Sol. Energy Mater. Sol. Cells* **95**, 2848–2854 (2011).
23. Meyer, B. K. *et al.* Binary copper oxide semiconductors: From materials towards devices. *Phys. Status Solidi B* **249**, 1487–1509 (2012).
24. Musa, A. O., Akomolafe, T. & Carter, M. J. Production of cuprous oxide, a solar cell material, by thermal oxidation and a study of its physical and electrical properties. *Sol. Energy Mater. Sol. Cells* **51**, 305–316 (1998).
25. Tsur, Y. & Riess, I. Self-compensation in semiconductors. *Phys. Rev. B* **60**, 8138–8146 (1999).
26. Yu, L., Xiong, L. & Yu, Y. Cu₂O Homojunction Solar Cells: F-Doped N-type Thin Film and Highly Improved Efficiency. *J. Phys. Chem. C* **119**, 22803–22811 (2015).
27. Liao, L. C.-K., Lin, Y.-C. & Peng, Y.-J. Fabrication Pathways of p-n Cu₂O Homojunction Films by Electrochemical Deposition Processing. *J. Phys. Chem. C* **117**, 26426–26431 (2013).
28. Minami, T., Nishi, Y. & Miyata, T. High-Efficiency Cu₂O-Based Heterojunction Solar Cells Fabricated Using a Ga₂O₃ Thin Film as N-Type Layer. *Appl. Phys. Express* **6**, 44101 (2013).
29. Izaki, M. *et al.* Electrochemically constructed p-Cu₂O/n-ZnO heterojunction diode for photovoltaic device. *J. Phys. Appl. Phys.* **40**, 3326–3329 (2007).
30. Lee, S. W. *et al.* Improved Cu₂O-Based Solar Cells Using Atomic Layer Deposition to Control the Cu Oxidation State at the p-n Junction. *Adv. Energy Mater.* **4**, n/a-n/a (2014).

31. Nishi, Y., Miyata, T. & Minami, T. The impact of heterojunction formation temperature on obtainable conversion efficiency in n-ZnO/p-Cu₂O solar cells. *Thin Solid Films* **528**, 72–76 (2013).
32. Love, J. C., Estroff, L. A., Kriebel, J. K., Nuzzo, R. G. & Whitesides, G. M. Self-Assembled Monolayers of Thiolates on Metals as a Form of Nanotechnology. *Chem. Rev.* **105**, 1103–1170 (2005).
33. Schreiber, F. Structure and growth of self-assembling monolayers. *Prog. Surf. Sci.* **65**, 151–257 (2000).
34. Cornil, D., Van Regemorter, T., Beljonne, D. & Cornil, J. Work function shifts of a zinc oxide surface upon deposition of self-assembled monolayers: a theoretical insight. *Phys Chem Chem Phys* **16**, 20887–20899 (2014).
35. Goh, C., Scully, S. R. & McGehee, M. D. Effects of molecular interface modification in hybrid organic-inorganic photovoltaic cells. *J. Appl. Phys.* **101**, 114503 (2007).
36. Lange, I. *et al.* Tuning the Work Function of Polar Zinc Oxide Surfaces using Modified Phosphonic Acid Self-Assembled Monolayers. *Adv. Funct. Mater.* **24**, 7014–7024 (2014).
37. Czeslik, C., Seemann, H. & Winter, R. *Basiswissen Physikalische Chemie*. (Vieweg + Teubner, 2010).
38. Salinas, M. *Interface Engineering with Self-assembled Monolayers for Organic Electronics*. (FAU University Press, 2014).
39. Koch, N. Organic Electronic Devices and Their Functional Interfaces. *ChemPhysChem* **8**, 1438–1455 (2007).
40. Yip, H.-L., Hau, S. K., Baek, N. S., Ma, H. & Jen, A. K.-Y. Polymer Solar Cells That Use Self-Assembled-Monolayer- Modified ZnO/Metals as Cathodes. *Adv. Mater.* **20**, 2376–2382 (2008).
41. Rühle, S. *et al.* Molecular Adjustment of the Electronic Properties of Nanoporous Electrodes in Dye-Sensitized Solar Cells. *J. Phys. Chem. B* **109**, 18907–18913 (2005).
42. Haick, H., Ambrico, M., Ligonzo, T. & Cahen, D. Discontinuous Molecular Films Can Control Metal/Semiconductor Junctions. *Adv. Mater.* **16**, 2145–2151 (2004).
43. Binnig, G., Quate, C. F. & Gerber, C. Atomic force microscope. *Phys. Rev. Lett.* **56**, 930 (1986).

44. *Atomic Force Microscopy in Liquid: Biological Applications*. (Wiley-VCH Verlag GmbH & Co. KGaA, 2012).
45. Melitz, W., Shen, J., Kummel, A. C. & Lee, S. Kelvin probe force microscopy and its application. *Surf. Sci. Rep.* **66**, 1–27 (2011).
46. Maragliano, C. *et al.* Quantifying charge carrier concentration in ZnO thin films by Scanning Kelvin Probe Microscopy. *Sci. Rep.* **4**, (2014).
47. Bauch, M. & Dimopoulos, T. Design of ultrathin metal-based transparent electrodes including the impact of interface roughness. *Mater. Des.* **104**, 37–42 (2016).
48. Dimopoulos, T., Radnoczi, G. Z., Horváth, Z. E. & Brückl, H. Increased thermal stability of Al-doped ZnO-based transparent conducting electrodes employing ultra-thin Au and Cu layers. *Thin Solid Films* **520**, 5222–5226 (2012).
49. Goldstein, J. *et al.* *Scanning Electron Microscopy and X-Ray Microanalysis: A Text for Biologists, Materials Scientists, and Geologists*. (Springer Science & Business Media, 2012).
50. Paunovic, M. & Schlesinger, M. *Fundamentals of electrochemical deposition*. (Wiley-Interscience, 2006).
51. Dharmadasa, I. M. & Haigh, J. Strengths and Advantages of Electrodeposition as a Semiconductor Growth Technique for Applications in Macroelectronic Devices. *J. Electrochem. Soc.* **153**, G47–G52 (2006).
52. Golden, T. D. *et al.* Electrochemical Deposition of Copper(I) Oxide Films. *Chem. Mater.* **8**, 2499–2504 (1996).
53. Angus, J. C. & Angus, C. T. Computation of Pourbaix Diagrams Using Virtual Species: Implementation on Personal Computers. *J. Electrochem. Soc.* **132**, 1014–1019 (1985).
54. Zhou, Y. & Switzer, J. A. Electrochemical Deposition and Microstructure of Copper (I) Oxide Films. *Scr. Mater.* **38**, 1731–1738 (1998).
55. Septina, W. *et al.* Potentiostatic electrodeposition of cuprous oxide thin films for photovoltaic applications. *Electrochimica Acta* **56**, 4882–4888 (2011).
56. Musselman, K. P. *et al.* Strong Efficiency Improvements in Ultra-low-Cost Inorganic Nanowire Solar Cells. *Adv. Mater.* **22**, E254–E258 (2010).

57. Rakhshani, A. E. & Varghese, J. Potentiostatic electrodeposition of cuprous oxide. *Thin Solid Films* **157**, 87–96 (1988).
58. Lee, Y. S. *et al.* Ultrathin amorphous zinc-tin-oxide buffer layer for enhancing heterojunction interface quality in metal-oxide solar cells. *Energy Environ. Sci.* **6**, 2112 (2013).
59. Serway, R. A., Moses, C. J. & Moyer, C. A. *Modern physics.* (Thomson Brooks/Cole, 2005).
60. Gu, S., Wang, X., Wei, Y. & Fang, B. Mechanism for nucleation and growth of electrochemical deposition of palladium(II) on a platinum electrode in hydrochloric acid solution. *Sci. China Chem.* **57**, 755–762 (2014).
61. Wu, S. *et al.* Nucleation Mechanism of Electrochemical Deposition of Cu on Reduced Graphene Oxide Electrodes. *J. Phys. Chem. C* **115**, 15973–15979 (2011).
62. Barin, C. S., Correia, A. N., Machado, S. A. S. & Avaca, L. A. The effect of concentration on the electrocrystallization mechanism for copper on platinum ultramicroelectrodes. *J. Braz. Chem. Soc.* **11**, 175–181 (2000).
63. Kramm, B. *et al.* The band alignment of Cu₂O/ZnO and Cu₂O/GaN heterostructures. *Appl. Phys. Lett.* **100**, 94102 (2012).
64. Gershon, T., Musselman, K. P., Marin, A., Friend, R. H. & MacManus-Driscoll, J. L. Thin-film ZnO/Cu₂O solar cells incorporating an organic buffer layer. *Sol. Energy Mater. Sol. Cells* **96**, 148–154 (2012).
65. Bai, Y. *et al.* High performance inverted structure perovskite solar cells based on a PCBM:polystyrene blend electron transport layer. *J Mater Chem A* **3**, 9098–9102 (2015).
66. Chen, L.-C., Chen, J.-C., Chen, C.-C. & Wu, C.-G. Fabrication and Properties of High-Efficiency Perovskite/PCBM Organic Solar Cells. *Nanoscale Res. Lett.* **10**, (2015).
67. Oku, T. *et al.* Structures and photovoltaic properties of copper oxides/fullerene solar cells. *J. Phys. Chem. Solids* **72**, 1206–1211 (2011).
68. Ishii, H., Sugiyama, K., Ito, E. & Seki, K. Energy Level Alignment and Interfacial Electronic Structures at Organic/Metal and Organic/Organic Interfaces. *Adv. Mater.* **11**, 605–625 (1999).
69. Braun, S., Salaneck, W. R. & Fahlman, M. Energy-Level Alignment at Organic/Metal and Organic/Organic Interfaces. *Adv. Mater.* **21**, 1450–1472 (2009).

70. Wilke, A. *et al.* Correlation between interface energetics and open circuit voltage in organic photovoltaic cells. *Appl. Phys. Lett.* **101**, 233301 (2012).
71. Cahen, D., Hodes, G., Grätzel, M., Guillemoles, J. F. & Riess, I. Nature of Photovoltaic Action in Dye-Sensitized Solar Cells. *J. Phys. Chem. B* **104**, 2053–2059 (2000).
72. Rangan, S. *et al.* Tuning Energy Level Alignment At Organic/Semiconductor Interfaces Using a Built-In Dipole in Chromophore–Bridge–Anchor Compounds. *J. Phys. Chem. C* **118**, 12923–12928 (2014).
73. Yang, B. *et al.* Solution-Processed Fullerene-Based Organic Schottky Junction Devices for Large-Open-Circuit-Voltage Organic Solar Cells. *Adv. Mater.* **25**, 572–577 (2013).
74. Liu, Y. *et al.* Solution-processed small-molecule solar cells: breaking the 10% power conversion efficiency. *Sci. Rep.* **3**, (2013).
75. He, Y. & Li, Y. Fullerene derivative acceptors for high performance polymer solar cells. *Phys Chem Chem Phys* **13**, 1970–1983 (2011).
76. Zhang, L., Roy, S. S., Hamers, R. J., Arnold, M. S. & Andrew, T. L. Molecular Orientation-Dependent Interfacial Energetics and Built-in Voltage Tuned by a Template Graphene Monolayer. *J. Phys. Chem. C* **119**, 45–54 (2015).
77. Rusu, P. C. & Brocks, G. Surface Dipoles and Work Functions of Alkylthiolates and Fluorinated Alkylthiolates on Au(111). *J. Phys. Chem. B* **110**, 22628–22634 (2006).
78. Förch, R., Schönherr, H. & Jenkins, A. T. A. *Surface Design: Applications in Bioscience and Nanotechnology*. (John Wiley & Sons, 2009).
79. Dimension Icon Bruker Training - Surface Potential Interleave and lift modes. Available at: <http://mmrc.caltech.edu/AFM%20Dimension%20Icon/Bruker%20Training/Bruker%20Training.html>. (Accessed: 6th September 2016)
80. Pan, Y. *et al.* Highly ordered, millimeter-scale, continuous, single-crystalline graphene monolayer formed on Ru (0001). *Adv. Mater.* **21**, 2777–2780 (2009).
81. Gwyddion – Free SPM (AFM, SNOM/NSOM, STM, MFM, ...) data analysis software. Available at: <http://gwyddion.net/>. (Accessed: 6th September 2016)

82. Robin, F., Jacobs, H., Homan, O., Stemmer, A. & Bächtold, W. Investigation of the cleaved surface of a p-i-n laser using Kelvin probe force microscopy and two-dimensional physical simulations. *Appl. Phys. Lett.* **76**, 2907 (2000).
83. Zhang, B. *et al.* Surface Functionalization of Zinc Oxide by Carboxyalkylphosphonic Acid Self-Assembled Monolayers. *Langmuir* **26**, 4514–4522 (2010).
84. Rhodes, C. L. *et al.* Characterization of monolayer formation on aluminum-doped zinc oxide thin films. *Langmuir ACS J. Surf. Colloids* **24**, 433–440 (2008).
85. Nogues, C. & Lang, P. Self-Assembled Alkanethiol Monolayers on a Zn Substrate: Structure and Organization. *Langmuir* **23**, 8385–8391 (2007).

List of Figures

Figure 1 Overview of the highest confirmed conversion efficiencies for research solar cells by the National Renewable Energy Laboratory (NREL) ²	1
Figure 2 Schematic diagrams of a p-n junction: (a) p-type (b) n-type (c) junction in contact and equilibrium (d) carrier concentration diagram	4
Figure 3 Energy band diagram of a p-n junction with external applied bias: (a) forward bias (b) reverse bias	5
Figure 4 reference sun solar spectrum.....	6
Figure 5 light absorption scheme	7
Figure 6 I-V curve of solar cell	8
Figure 7 equivalent circuit of solar cell.....	9
Figure 8 hybridization of ethene (a) orbital scheme (b) energy level diagram	11
Figure 9 hopping mechanism (left) spatial and (right) energy landscape of hopping transport under influence of an external electric field [figure taken from ¹²].....	12
Figure 10 [70] PCBM chemical structure [figure taken from Sigma-Aldrich website ¹⁴].....	12
Figure 11 schematic structure of SAMs	14
Figure 12 Electronic energy levels of the tip-sample system for three different cases: a) equilibrium & no contact b) contact & no external bias c) contact & external applied bias.....	18
Figure 13 design layout of the hybrid solar cell	20
Figure 14 light absorption of Cu ₂ O on a IMI electrode and ITO-layer	22
Figure 15 potentiostatic electrodeposition setup	23
Figure 16 cyclic voltammogram of Cu ₂ O for ITO and Au.....	25
Figure 17 Current- time transients of Cu ₂ O deposited on Au bottom electrode at different deposition potentials	26
Figure 18 SEM picture of electrodeposited Cu ₂ O with a deposition potential of - 0,28 V on a Au bottom-electrode a) 2k magnification b) 30k magnification.....	27
Figure 19 SEM picture of electrodeposited Cu ₂ O with a deposition potential of - 0,29 V on a Au bottom-electrode a) 2k magnification b) 30k magnification.....	27
Figure 20 SEM cross-section of Cu ₂ O on an Au bottom-electrode.....	28
Figure 21 AFM picture of electrodeposited Cu ₂ O on a Au bottom-electrode.....	29

Figure 22 height profile of Cu ₂ O on Au electrode - taken from Figure 21 (white line).....	29
Figure 23 reflectivity measurement of Cu ₂ O - sample	30
Figure 24 reflectance measurement - Cu ₂ O - band gap	31
Figure 25 XRD-pattern of Au/Cu ₂ O structure.....	32
Figure 26 Current- time transients of Cu ₂ O deposited on IMI bottom electrode at different deposition potentials	33
Figure 27 SEM picture of Cu ₂ O on a IMI bottom-electrode a) 2k magnification b) 15k magnification	34
Figure 28 AFM picture of electrodeposited Cu ₂ O on a IMI bottom-electrode	34
Figure 29 height profile of Cu ₂ O on IMI electrode - taken from AFM Figure 28 (white line).....	35
Figure 30 SEM comparison of the grain size dependency of the bottom electron in electrochemical deposition	36
Figure 31 AFM height picture before (left image) and after (right image) the deposition of PCBM ...	39
Figure 32 height profile before (top) and after (bottom) depositing PCBM - taken from AFM Figure 31(white line respectively)	39
Figure 33 SEM surface picture before and after the spin coating of PCBM.....	40
Figure 34 IV- characteristics of reference materials - AZO and ZnO/AZO.....	42
Figure 35 SEM cross-section of IMI/Cu ₂ O/AZO structure.....	43
Figure 36 IV- characteristics of Au/Cu ₂ O/PCBM/AZO heterojunction solar cell - influence of annealing before depositing PCBM	44
Figure 37 IV- characteristics of Au/Cu ₂ O/PCBM heterojunction solar cell – illumination time influence on the performance of the solar cell - 10 min illumination between measurements	45
Figure 38 IV- characteristics of Au/Cu ₂ O/PCBM/AZO heterojunction solar cell - Performance of several pixels of an exemplary device.....	46
Figure 39 effect of parasitic resistance - shunt resistance and series resistance of Au/Cu ₂ O/PCBM structure, Au/Cu ₂ O/ZnO structure and IMI/Cu ₂ O/ZnO structure.....	48
Figure 40 IV - characteristics Cu ₂ O/PCBM interface – photocurrent	49
Figure 41 IV- characteristics of ITO/Cu ₂ O/PCBM heterojunction solar cell - Performance of several pixels of an exemplary device	51
Figure 42 Band diagram Cu ₂ O/PCBM.....	54

Figure 43 comparison of the potential-map – Cu ₂ O on the left and the same Cu ₂ O with deposited SAM on the right	60
Figure 44 row-average CPD diagram of Cu ₂ O and Cu ₂ O/SAM surface.....	62
Figure 45 illustration of the net dipole moment formed by depositing a SAM layer – a) SAM with positive intrinsic dipole moment and b) SAM with negative intrinsic dipole moment.....	64
Figure 46 KPFM results and band diagram for Cu ₂ O/SAM interface.....	65
Figure 47 KPFM-images of Cu ₂ O/PCBM interface: a) Cu ₂ O image b) image after PCBM deposition c) row-average CPD plot.....	67
Figure 48 Zoomed-in AFM and KPFM picture of Cu ₂ O before and after the deposition of PCBM	68
Figure 49 KPFM-images of Cu ₂ O/SAM/PCBM interface: 1-3) modification with positive dipole SAM (tfba) 4-6) modification with negative dipole SAM (tba)	70
Figure 50 row-average CPD diagram of Cu ₂ O/SAM/PCBM interface - a) modification with negative dipole SAM (tba) b) modification with positive dipole SAM (tfba).....	71
Figure 51 KPFM results and band diagram of Cu ₂ O/SAM/PCBM interface.....	73
Figure 52 IV – measurement of the SAM modified Au/Cu ₂ O/PCBM/AZO heterojunction – a) modified with positive dipole SAM b) modified with negative dipole SAM c) reference Cu ₂ O/PCBM interface	74

List of tables

Table 1 summary of benzoic acid derivatives	16
Table 2 sputtering parameter bottom electrode	21
Table 3 surface roughness comparison - Au electrode.....	30
Table 4 Element data used to analyze the XRD	31
Table 5 Identification of the resulting XRD peaks.....	32
Table 6 surface roughness comparison - IMI electrode	35
Table 7 calculated average surface roughness.....	36
Table 8 top electrode sputtering parameter	37
Table 9 surface roughness - comparison before and after depositing PCBM	40
Table 10 zinc oxide sputtering parameter	41
Table 11 IV-characteristics for reference solar cell - AZO and ZnO/AZO.....	42
Table 12 IV-characteristics Au/Cu ₂ O/PCBM/AZO - annealing	44
Table 13 IV-characteristics of Au/Cu ₂ O/PCBM/AZO - device	46
Table 14 calculated values for the parasitic resistance of the Cu ₂ O/PCBM and the Cu ₂ O/ZnO interface structure.....	48
Table 15 IV-characteristics of IMI/Cu ₂ O/PCBM - device	50
Table 16 average output characteristics of Au/Cu ₂ O/PCBM/AZO-hybrid solar cell.....	52
Table 17 band diagram - literature data of cuprous oxide and PCBM	54
Table 18 Contact angle of Cu ₂ O and Cu ₂ O with self-assembled molecules.....	57
Table 19 average surface roughness of Cu ₂ O before and after the deposition of a SAM- monolayer .	59
Table 20 average CPD of Cu ₂ O before and after the deposition of a SAM- monolayer	61
Table 21 average CPD of Cu ₂ O before and after the deposition of a PCBM layer	67
Table 22 review of SAMs used for interface modification	69
Table 23 average picture CPD of tfba and tba modified structure	71
Table 24 overall change in the Cu ₂ O/PCBM surface energy due to the introduction of SAMs	72
Table 25 characteristics from IV measurement of Cu ₂ O/PCBM interface modification using SAMs .	75
Table 26 IV-characteristics of Cu ₂ O/PCBM interface	76

Table 27 IV-characteristics of Cu ₂ O/PCBM interface modification using SAMs	77
---	----